

HETEROEPITAXIAL DIMER STRUCTURES ON THE SILICON(100) SURFACE

By

MARK WAYNE GRANT

A DISSERTATION PRESENTED TO THE GRADUATE SCHOOL
OF THE UNIVERSITY OF FLORIDA IN PARTIAL FULFILLMENT
OF THE REQUIREMENTS FOR THE DEGREE OF
DOCTOR OF PHILOSOPHY

UNIVERSITY OF FLORIDA

1994

TABLE OF CONTENTS

	<u>page</u>
ACKNOWLEDGMENTS	v
ABSTRACT	vi
 CHAPTERS	
1 INTRODUCTION	1
Surface Structures	2
Transmission Ion Channeling	6
2 EQUIPMENT	8
UHV Chambers	8
Introduction Chamber	9
Preparation Chamber	9
Ion Scattering Chamber	11
Accelerator	12
3 MeV ION SCATTERING	17
Rutherford Backscattering Spectroscopy	17
Channeling	20
4 SUBSTRATE PREPARATION AND CHARACTERIZATION	29
Thin Si Windows	30
Chemical Preparation	30
Surface Cleanliness	30
Crystallinity	33
Thin Ge Windows	35
Fabrication	35
Characterization of Crystallinity	39
Surface Cleaning	44
5 CHANNELING CALCULATIONS	47
Calculated Yields	48

Assumptions	48
Execution	56
Crystallographic Projections	60
6 DATA REDUCTION	66
Experimental Angular Scan Extraction	66
Comparison of Experimental and Calculated Angular Scans	74
7 THE Si(100) SURFACE	83
8 Sb ON THE Si(100) SURFACE	88
Motivation.	88
Experiment	90
Results and Discussion	93
Annealed Surfaces.	93
Unannealed Surfaces	95
9 Ge ADSORBED ON THE Si(100) SURFACE	101
Motivation.	101
Experiment	103
Results and Discussion	103
Adatom Adsorption Sites (0.6 ML)	103
Coverage Dependence.	109
10 Sb DEPOSITED ON PSEUDOMORPHIC Ge ON Si(100)	114
Motivation.	114
Experiment	117
Results and Discussion	119
11 CONCLUSIONS	127
Sb on Si(100)	127
Ge on Si(100)	129
Sb on Ge on Si(100)	130

APPENDICES

A Si <i>EX SITU</i> TREATMENT	132
B Ge THIN WINDOWS: DEFECT ANALYSIS	134

REFERENCES	137
BIOGRAPHICAL SKETCH	146

ACKNOWLEDGMENTS

There are many to whom I owe a debt at this point in my life. Paramount among these are my parents and sisters; no person could expect a more loving and supportive family. They have been a constant and reliable source of encouragement.

I also wish to acknowledge the support of my advisor, Liz Seiberling. She has shown a wealth of patience, always providing a challenging yet comfortable environment in which to work. It is largely do to her guidance that I was able to finish this thing. I am also indebted to Paul Lyman for getting me started in the lab, and for doing all of the hard work before I began. He has been a good friend.

In the way of colleagues, I have been lucky. My life has been greatly enriched by the opportunity to interact with two Dutch students, Jan Hoogenraad and Danny Dieleman, and a Pole, Andrez Dygo. All have expanded my view of the world (not to mention, Danny and I have the same taste in bars). It has also been a pleasure to share a lab and office with Mark Boshart. He and I have had quite a few laughs. I have, as well, enjoyed and benefited from my friendships with Allison Bailes and Rick Picullio. I wish to thank Dave Wilmess for keeping me sane. Also, I thank the many others, too numerous to name, who have made my stay here as pleasant as could be expected.

Finally, I wish to acknowledge the love and understanding of Wendy this last year.

Abstract of Dissertation Presented to the Graduate School
of the University of Florida in Partial Fulfillment of the
Requirements for the Degree of Doctor of Philosophy

HETEROEPITAXIAL DIMER STRUCTURES ON THE SILICON(100) SURFACE

By
Mark W. Grant

August 1994

Chairman: Lucy Elizabeth Seiberling
Major Department: Physics

I have used transmission ion channeling to characterize thin heteroepitaxial films on the Si(100) surface. The studies have been structural in nature, designed to determine the adatom bonding sites for three separate but related systems: Sb deposited on the Si(100) surface at coverages ≤ 1 monolayer (ML), Ge below 1 ML on Si(100), and Sb deposited on 1 ML pseudomorphic Ge on Si(100). These studies illustrate the power and utility of transmission channeling for adatom site determination.

For the Sb/Si(100), I have determined the overlayer geometry for samples annealed at 550°C after Sb deposition. I find this surface to be terminated by symmetric Sb-Sb dimers having a bond length of 2.8 ± 0.1 Å. The site compares well with previous studies for the annealed surfaces. Surprisingly, I find that the surface

formed upon deposition at room temperature also is terminated by symmetric dimers, in spite of the presence of significantly less long-range order on the surface.

I have characterized the Ge-adsorbed Si(100) surface for a range of coverages. The data suggest the presence of some coverage dependence on the surface. The bonding geometry of the Ge has been determined for a Ge coverage of 0.6 ML, yielding asymmetric dimers, having a bond length of 2.6 ± 0.1 Å and a dimer tilt of $12 \pm 4^\circ$.

Having characterized these systems, I next studied the system of 1 ML of Sb adsorbed on 1 ML Ge-terminated Si(100). Two structural issues were addressed. First, the effect of the Sb overlayer on the Ge has been determined. Upon deposition of Sb, the reconstruction in the Ge layer is lifted, rendering the Ge near bulk-like. Second, the geometry of the Sb overlayer on strained Ge has been determined. By characterizing both the Ge and Sb layers, I conclude that the Sb dimers are asymmetric, having a bond length of 2.76 ± 0.07 Å and a dimer tilt of $7 \pm 3^\circ$.

CHAPTER 1 INTRODUCTION

The main focus of this dissertation concerns the deposition, and subsequent formation of monolayer (1 monolayer, ML, is defined as 6.78×10^{14} atoms/cm²) films, of foreign chemical species on the clean Si(100)-2x1 surface (heteroepitaxy). Specifically, three systems are addressed: germanium adsorbed at coverages below 1 ML on the clean Si(100) surface {Ge/Si(100)}, near 1 ML of antimony adsorbed on the clean Si(100) surface {Sb/Si(100)}, and 1 ML of antimony adsorbed on 1 atomic layer of Germanium on the Si(100) surface {Sb/Ge/Si(100)}. These studies, though conducted on technologically important systems, were motivated by an interest in the basic physical mechanisms governing the interactions of the adsorbates (adatoms) with the surface and with each other. They were designed to determine the *structures* of these surfaces on an atomic scale, and thereby to elucidate the processes leading to epitaxy and interface formation. While it is often the case that the application of any single experimental technique does not lead to a complete understanding of a given physical system, it is true that through the combined efforts of many techniques and with the contemplation of many scientists, often, collectively, such an understanding may be achieved. Studies of semiconductor surfaces are, more often than not, characterized by this collective approach. In this spirit, the following structural investigations were undertaken.

In the interest of clarity, the discussions of the three systems studied (Sb/Si, Ge/Si, Sb/Ge/Si) are presented separately and the relevant connections are made in the conclusions. These three topics constitute chapters 8, 9, and 10. For each, remarks on the motivation for the research are presented along with a review of the important results from other researchers. In no way are these intended to be a complete reviews

of the topics. In general, only work directly impacting the interpretation or understanding of the present results is included. Preceding those specific chapters are ones describing the experimental procedures and data reduction, including a discussion of the main technique and computer calculations involved in the analysis. Those topics covered in detail were chosen to facilitate the continued effort by the research group on such studies. For instance, a moderate amount of space has been devoted to the production and characterization of alternate substrates (Ge, chapter 4), as this information should be useful for future studies of adsorbates on the Ge(100) surface using transmission ion channeling. In contrast, little space is devoted to the experimental setup, since this, while important, has been covered thoroughly elsewhere [Lyma91a].

The results presented here should be of interest to many theorists and experimentalists concerned with reconstructed surface structures in relation to electronic properties, epitaxy on strained layers, surfactant-mediated growth, adatom mobility, and many other topics. In addition, ion-beam enthusiasts should be interested in these studies as an example of the power and utility of MeV ion beams. These two aspects of this study are introduced below.

Surface Structures

When a crystalline surface is created (by cleaving or cleaning) in the absence of contaminants (i.e. in a vacuum), the resultant two crystals are terminated by atoms that are representative of the bulk constituents of the material, but that reside in a physical and chemical environment which has been altered drastically. As a result, the outermost atomic layer, as well as several layers directly adjacent to it, often exhibits structural characteristics not observed in the bulk [Zang88]. In order to compensate for their new environment, the surface atoms move from their nominal, bulk-terminated lattice positions to a configuration of lower energy. For Si surfaces, due

partly to the directional nature of the Si-Si bonds and to the dangling bonds left by the act of cleaving, the effect is remarkable [Need87; Robe90; Chad79; Jaya93]. For this and other semiconductors, such movement ("reconstruction") typically occurs in the plane of the surface and the phenomenon is often accompanied by altered bonding states, orbital rehybridization, and lattice strain [Mead89; Redo82; Appe78a; Appe78b; Ters92]. As a dramatic example, consider the clean Si(111) surface. The ideal bulk-terminated surface has a simple 1x1 symmetry (the "mxn" nomenclature indicates the number of in-plane bulk lattice vectors needed to describe the reconstructed surface). However, the surface in equilibrium at room temperature exhibits a superstructure having a 7x7 symmetry, where more than 100 atoms per unit cell take place in the reconstruction over 4 atomic layers [Zang88, p. 49]. This amazing structure is illustrated in figure 1-1. Note the complexity and substantial size of the surface unit cell.

The surface of interest in this study, Si(100), commonly exhibits a considerably less complicated reconstruction. The surface unit cell contains only 2 top-layer atoms, and the symmetry of the surface (2x1) [Schl59] is related simply to the symmetry of the bulk. The surface, though, still exhibits striking structural features which are not completely transparent, despite years of intense study by experimentalists and theorists. Perhaps because of the relative simplicity and the technological importance of this particular Si surface, it has become a model one to study and somewhat of a gauge with which to measure the current state of the science. Although the reconstructed surface is presumably in an energetically-optimized configuration for clean Si, the surface is still highly reactive, possessing one dangling bond per surface atom [Chad79; Redo82]. Because of this reactivity, most impurities introduced on the surface will interact in such a way as to form chemical bonds with the topmost Si atoms (chemisorb), and hence adhere to the surface in preferred bonding sites

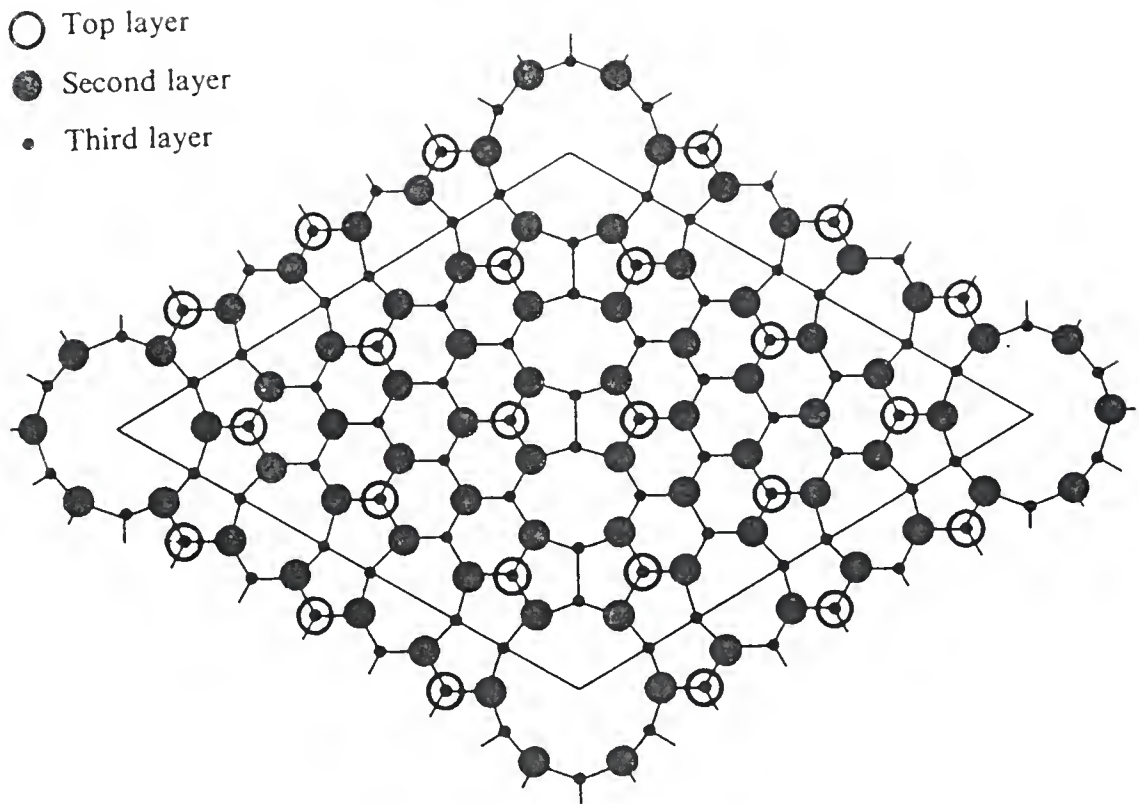


Figure 1-1. Si(111) 7x7 surface reconstruction. Shown is the surface unit cell. This figure is from Zangwill [Zang88, p. 49].

[Tang92; Zang88, p. 185]. For this reason, structural studies on such systems are of interest.

Since the primary thrust of these structural studies has been to elucidate the ordering, on an atomic level, of chemisorbed overlayers on the Si(100) surface, the studies concentrate on thin films. This focus entails the deposition of monolayers (a few Å) of the adsorbate, and hence involves the initial stages of interface formation and the chemistry of the initial stages of epitaxial growth. At this level, structural studies address the positions of adsorbed atoms with respect to the underlying Si lattice and/or the positions of the adatoms with respect to each other. Also of interest is the effect of the adsorbed overlayer on the underlying, adjacent Si. Issues affecting the surface region in these systems can involve such variables as the size of the adatom [Cope90], the availability and mobility of the adatoms [Ters94; Mo90; Eagl93], epitaxy-induced surface stress [Trom92a; Ters91; Trom93], the preferred valence electron state of the adatom [Mead89; Uh86], the relative strength of the adsorbate-adsorbate to adsorbate-substrate interaction [Mo92; Barn86], and the interaction of the adatoms with defects (such as steps and surface vacancies) on the surface [Mo89; Stil92].

It has been through intense study that detailed features of such systems typically are clarified. From the beginning, advances in experimental studies have accompanied advances in theoretical treatments, as the experimentally determined bonding geometries and subsurface lattice distortions were compared to those predicted by total energy calculations, molecular dynamics simulations, or some other treatment. The usual result was a clearer understanding of the mechanisms leading to reconstruction and a more certain interpretation of experimental data [Appel78b; Chad79]. In conjunction with the electronic properties of such surfaces, provided by probes such as photoemission spectroscopy [Rowe74; Land92; Yang92], both

structural studies and theories foster insight into the bonding characteristics of these increasingly difficult systems. It is hoped that the work presented herein will aid in this effort.

Transmission Ion Channeling

The development of the technique of transmission ion channeling has occurred over the last 30 years. The initial discovery of the channeling phenomenon sprang from the observation of anomalous sputtering yields that varied with incident-beam angle [Rol60] and anomalous ranges of ions in crystals when the crystals were aligned in certain directions [Davie60]. There was then a tremendous amount of experimental and theoretical work on the subject (there are several early review articles on the subject including that by Gemmell [Gemm74]). For instance, one important work was published in 1965 by Lindhard [Lind65], detailing the continuum model (chapter 5) and making several other lasting contributions to the field. Also, Barrett, using computer simulations of the channeling process, provided early insights into the interpretation of channeling data [Barr71]. It was realized early on that the channeling effect could be used to locate impurities in crystalline materials. Experiments in this vein were first conducted around 1967 [Bøgh67, Matz67]. Now such lattice location experiments in the bulk are common. Examples include a wide range of impurities in a variety of crystals, from W implanted in Cu at various levels [Bord76] to D implanted [Bech88a] in Si.

The first use of transmission ion channeling for interface studies was that of Feldman *et al.* [Feld78] in studies of the Si-SiO₂ interface. It was first used to determine the adsorption site of an impurity on a surface in 1981 with the study by Cheung and Mayer of Ni on the chemically clean Si surface [Cheu81]. Similar studies were carried out by Jin, Ito and Gibson for Au on Si(100) [Jin85]. In the 1980's, a group at the University of Aarhus, Denmark, began using channeling in the

transmission geometry for studies of D, H, O and Te on metal surfaces [Mort88, Jens90]. Then, in 1985, the first ultrahigh vacuum (UHV) adsorption-site determination was carried out on a UHV-cleaned surface using transmission ion channeling on a metal surface {D on Ni(100)} [Sten85].

Continuing to expand the range of application of this technique, the results presented in this dissertation represent the first use of the technique for the determination of adsorbate bonding sites on the UHV-clean Si(100)-2x1 surface. Also, channeling in the transmission geometry (such that the beam passes through the sample, with scattered particles detected at forward angles), or transmission channeling, is currently practiced at only a few laboratories in the world. At the University of Florida Van de Graaff accelerator, where the present studies were undertaken, many of the clean-surface-preparation and equipment-related problems were solved prior to the present work, and studies had been conducted using transmission ion channeling on the pseudomorphic growth of Ge thin films on Si(100) [Lyma91b]. However, no structural studies on an atomic level had been performed. A secondary focus of the work detailed in this dissertation has therefore been to refine the existing techniques, leading to the ability to use transmission ion channeling for adatom site determinations on clean semiconductor surfaces [Seib93]. Finally, the techniques developed were tested on physical systems. Specifically, agreement was sought with previous studies for the systems of Sb/Si(100) annealed at 500°C, which had been structurally characterized using surface extended x-ray adsorption fine structure (SEXAFS) and scanning tunneling microscopy (STM) [Richt90], and Ge/Si(100), which had been structurally characterized using x-ray standing waves (XSW) [Font93].

CHAPTER 2 EQUIPMENT

The quantity and complexity of the equipment used for the studies presented here has much to do with the intrinsic nature of the experiments. These are surface studies, which require meticulous care for the provision of a clean vacuum environment. This objective is accomplished through the use of modern vacuum chambers, pumping systems, and monitoring systems. In addition, the samples studied often are produced employing molecular beam epitaxy, and characterized with several standard surface analysis techniques. Since these samples are of acceptable quality for a limited time, adequate procedures and equipment for the introduction and transfer of samples into the vacuum chamber are necessary. The main technique used for analysis, MeV ion scattering, also requires special equipment for the attainment of a suitable beam, while maintaining good vacuum, and the ability to detect scattered particles in a variety of geometries. This whole capability is then coupled to an accelerator (which produces the ion beam) and occupies a footprint consistent with the limited laboratory space available. An extensive and complete description of this setup has been given in the Ph.D. thesis of Lyman [Lyman91a]. In the interest of completeness, this chapter contains a brief discussion of the experimental equipment and capabilities.

UHV Chambers

Because of the large number of sample preparation and experimental capabilities required to perform these surface studies, geometrical issues and port space are of concern. This set of constraints has led to the use of three separate, interconnected ultrahigh vacuum (UHV) experimental chambers. One chamber is dedicated to ion scattering and another to sample preparation. A third, smaller

chamber is used as a means of introducing several samples (up to five) into the system at a time. It provides the ability to change samples quickly (unfortunately, a common occurrence) without breaking vacuum. Each of these chambers can be isolated via UHV-compatible valving, making maintenance on any given one possible while the others are pumped. Figure 2-1 shows an overhead view of the setup. Samples are clipped to Ta modules that can be picked up and moved under vacuum from one chamber to the next using rack-and-pinion transfer arms. Vacuum is maintained in the system by careful attention to the cleanliness and composition of materials inserted and by baking the preparation and scattering chambers after each break in vacuum. The baking procedure consists of heating the chambers to $\sim 130^{\circ}\text{C}$ for around 2 days.

Introduction Chamber

The stainless steel sample introduction chamber contains a carousel with receptacles for five sample modules. Thin Si crystals to be used as substrates are prepared chemically and cleaned *ex situ* (see chapter 4), then clipped to modules and loaded into the introduction chamber five at a time. The introduction chamber is then evacuated to roughly 2×10^{-9} Torr, a process which usually takes several hours and requires no bakeout. The chamber is small (8" diameter) and is pumped by a Varian 150 l/s diode ion pump. A gatevalve separates the pump from the chamber. The chamber contains an ion gauge for measuring the pressure. This gauge, however, is seldom used because of a suspicion that it contaminates the samples, which are in close proximity. There are several viewports to facilitate sample transfer. A module then can be picked up, translated into the preparation chamber, and attached to the sample manipulator therein.

Preparation Chamber

The commercial, stainless steel sample preparation chamber (12" diameter) is pumped by a 300 l/s ion pump, and has a base pressure of 5×10^{-11} Torr. The sample

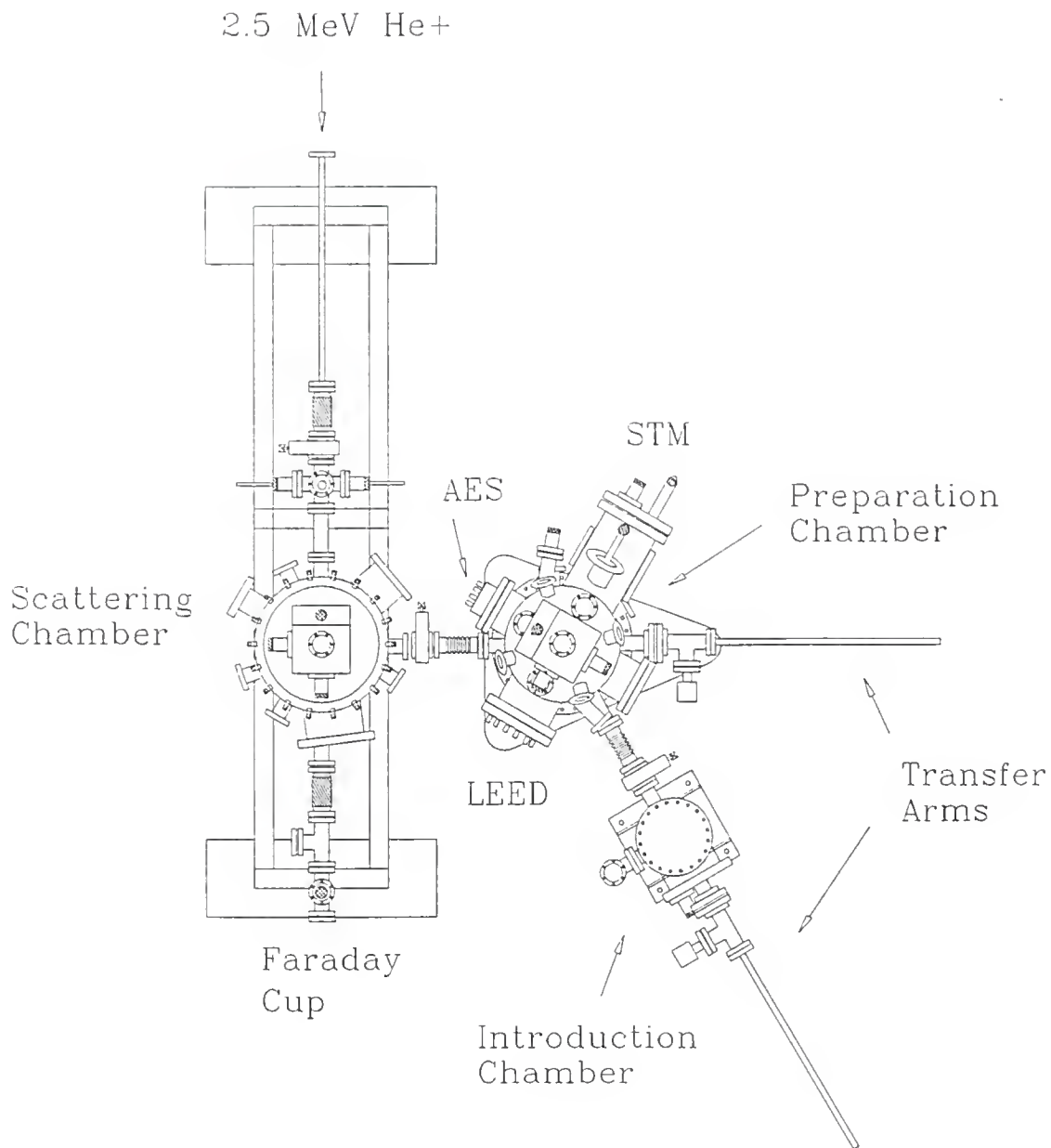


Figure 2-1. Experimental setup. The three UHV chambers are illustrated schematically from an overhead view (from the Ph.D. thesis of P. Lyman, p.19) [Lyman91a]. Sample preparation and surface characterization equipment are contained in the preparation chamber. The scattering chamber is equipped with 4 solid-state charged particle detectors. Samples are moved from chamber to chamber with the transfer arms.

manipulator has two angular and three translational degrees of freedom. A sample can be heated radiatively to $>1000^{\circ}\text{C}$ using a Ta strip heater on the sample stage or by a retractable heat lamp, and can be cooled by contact with a copper braid attached to an *in situ* liquid nitrogen reservoir. We have succeeded in cooling a sample to -40°C by suspending a pressurized (~ 8 psi) 40 l liquid nitrogen dewer near, and connected with a short rubber hose to, the nitrogen inlet port and flowing nitrogen through the reservoir. The heat lamp consists of an *in vacuo* tungsten-halogen bulb whose filament is at one focus of an elliptical nickel reflector; the lamp can be translated so that the other focus of the reflector is near the sample. The lamp has a maximum power of 250 W and can melt Si. The strip heater is composed of a 1.0 cm x 1.5 cm x 0.0127 mm strip of Ta and is shielded from the rear of the sample by a thin sheet of sapphire. The temperature of a sample is estimated from the current passing through the Ta strip, using a calibration curve [Lyman91a]. The calibration was performed with a thermocouple in contact with a thin window. The chamber is outfitted with rear view low energy electron diffraction (LEED) optics and a cylindrical mirror analyzer for Auger electron spectroscopy (AES) for surface characterization. The sample modules are designed so that a given sample can be analyzed with LEED, AES and transmission channeling without breaking vacuum. Sample preparation instruments include an ion sputter gun and two effusion cells. A residual gas analyzer (RGA) is available for the characterization of gas species in the chamber.

Ion Scattering Chamber

The ion scattering chamber has a base pressure of 5×10^{-11} Torr, and is maintained at pressures below 1×10^{-10} Torr with beam on sample by differential pumping along the beam line. The chamber is composed of stainless steel, has a 12" diameter, and is pumped by a 500 l/s Varion diode ion pump. The samples are mounted on a precision goniometer with two angular and three translational degrees of

freedom (see figure 2-2), typically allowing five well-separated beam spots (1 mm²) per thin window (7 mm diameter). In this geometry, with the exception of one point on the sample, a rotation about either axis may result in a translation of the beam spot. Near the <100> axial direction, for which this effect is greatest, and for a beam spot maximally displaced from the axis of rotation, a rotation of the sample about its normal by 2° (typical for an angular scan) leads to a displacement of approximately 0.05 mm. This displacement causes only 5% of the beam to irradiate a new part of the surface. A change in the beam spot on this level is not expected to significantly influence our results. A Faraday cup is located downstream of the sample, and is fitted with a viewport in the rear. The beam can be stopped either by a piece of tantalum or by a quartz disc. The quartz fluoresces when struck by the beam, and the beam profile thereby can be observed. Four bakeable, passivated, ion-implanted silicon detectors are mounted at angles of 18, 50, 78, and 150° to the beam direction. The geometrical placement of the detectors is illustrated in figure 2-3. The 78° detector is mounted below the sample, attached to the goniometer (facing up). The detector at 18° is covered by a thin foil (10 micron Al), and is used to measure elastic recoils [Behr87].

Accelerator

As indicated in figure 2-1, the system of UHV chambers is connected via a beamline to an ion accelerator. The accelerator is a HVEC 4 MV single-ended Van de Graaff, that, in practice, is capable of producing a high current (μA) beam of H⁺ or He⁺ ions in an energy range of 0.5 to 3.5 MeV. For a typical experiment, we use 2.5 MeV He⁺, with a current on sample of 5-20 nA (singly charged, *i.e.*, before passing through sample). The current is reduced from the nominal ≈300 nA produced by the Van de Graaff by the insertion of a small (1.6mm) aperture in the beamline after focusing the beam at the end of the beamline to a size of 2x2 mm. This aperture also serves, along with collimating slits, to limit the beam divergence, which we estimate as

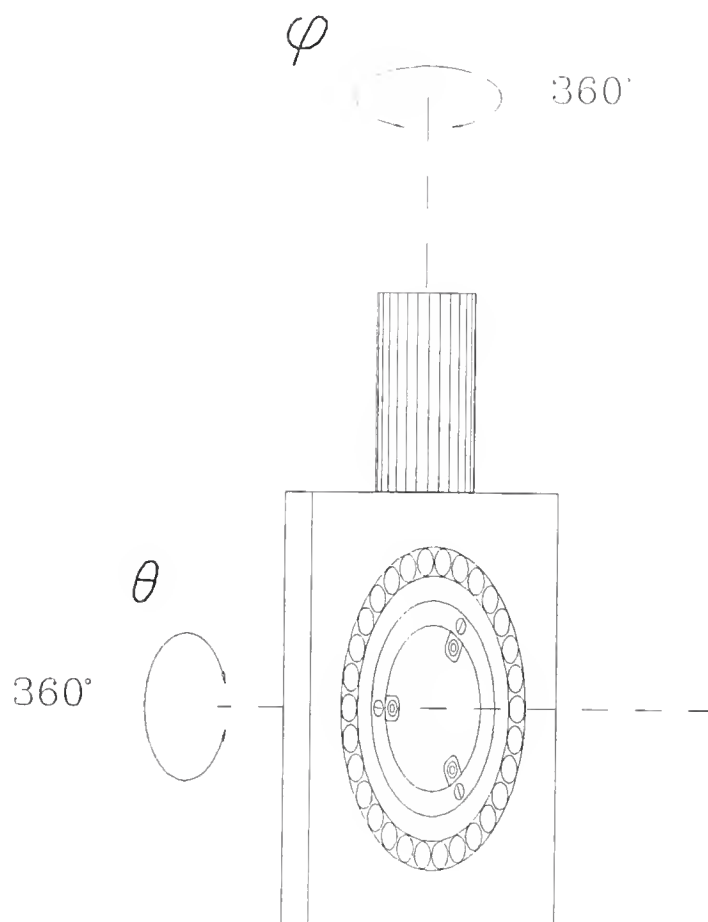


Figure 2-2. Scattering chamber goniometer. Indicated are the θ and ϕ angular degrees of freedom. The manipulator to which this is attached also provides 3 translational degrees of freedom.

Detector placement (Top view)

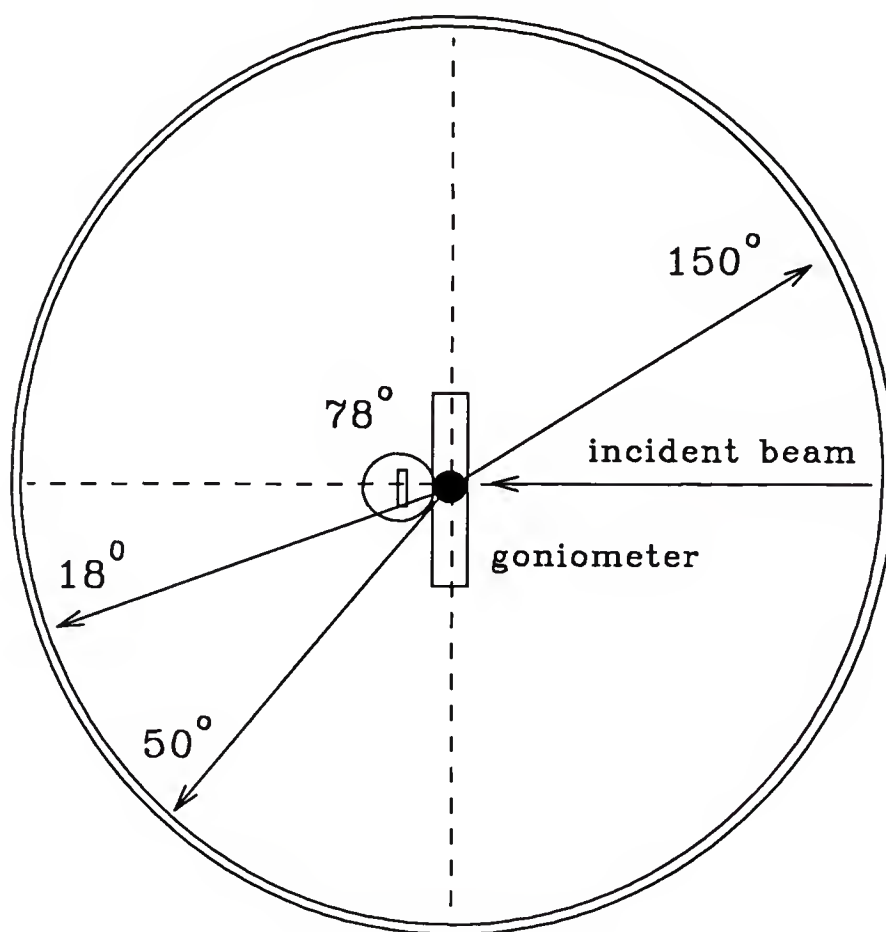


Figure 2-3. Top view of the detector arrangement in the scattering chamber. After passing through the sample (center), the beam enters a Faraday cup (not shown) for current integration.

$<0.8^\circ$. The incident beam energy is determined by measuring the field strength of the analyzing magnet with a nuclear magnetic resonance gaussmeter.

The strength of the magnetic field has been calibrated against the beam energy using the $^{27}\text{Al}(p,\gamma)\text{Si}^{28}$ resonance reaction at 991.9 keV [Feld77]. Two points were obtained for the calibration by counting γ 's as the energy was varied for both H^+ and H_2^+ beams. Figure 2-4 shows the data used for the calibration. The vertical axis displays the number of gammas detected. The horizontal axis displays the frequency of the NMR probe and is related linearly to the strength of the magnetic field analyzing the beam. The signal has the form of a step function because the H particles were incident on a thick Al target and therefore produced gammas at some point in the target whenever the energy of the beam was above that for the resonance. In each case (H^+ and H_2^+) the voltage on the Van de Graaff terminal was adjusted to give 992 keV per H particle at the sample when on resonance, yielding the two data points needed for the calibration.

It should be noted that this procedure was performed after the data presented in this manuscript were taken. Upon calibration it was discovered that the energy of the beam was slightly in error using the earlier tabulated frequency settings. This shift would have caused a slight, systematic underestimation of the absolute coverage determined for each sample. However, since there was no way to know precisely when the discrepancy arose, and since any error introduced was within our experimental uncertainty in the coverage, the data were not corrected.

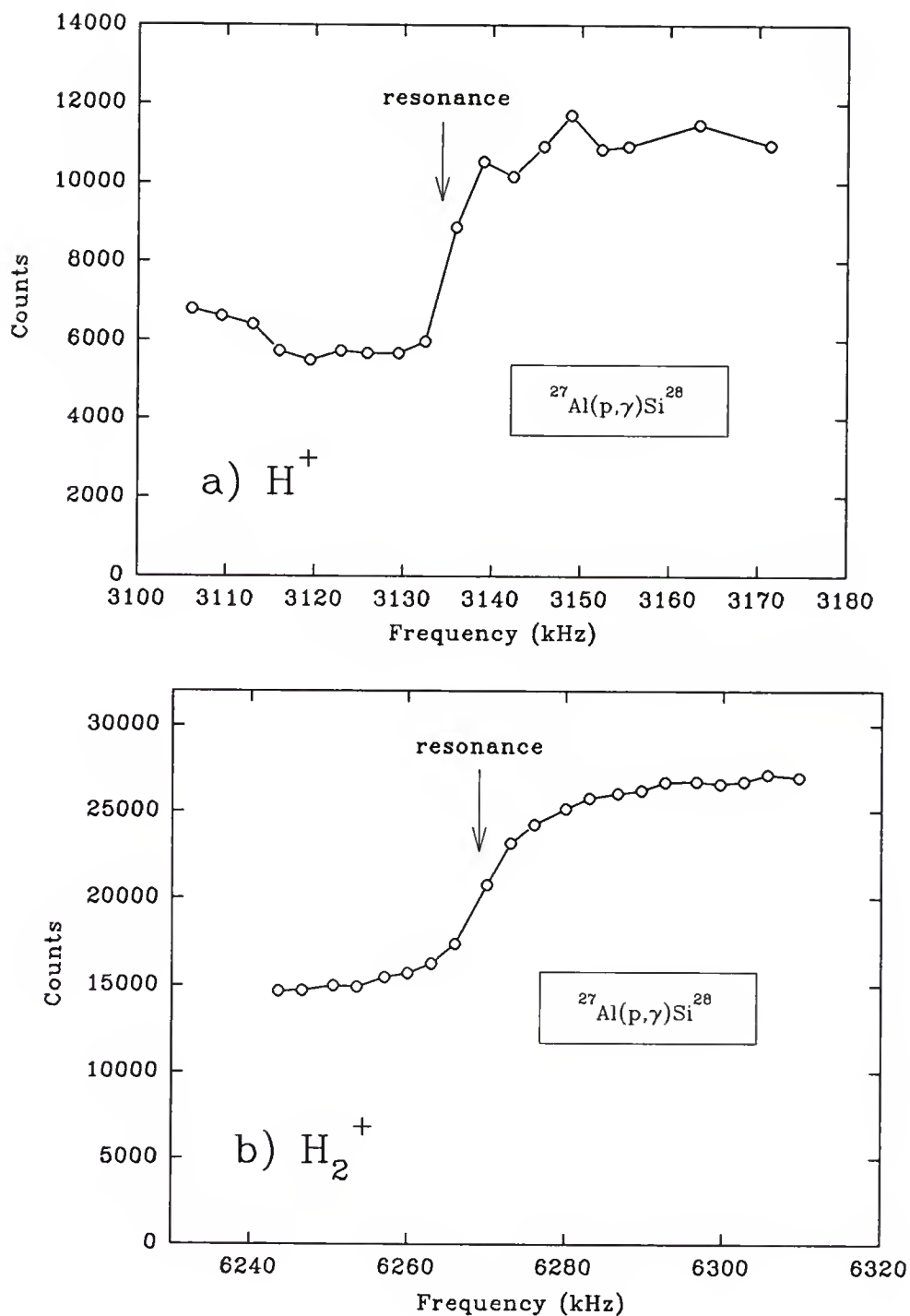


Figure 2-4. Data used for Van de Graaff calibration. The resonance is located at the half-height of the step. a) Data for H^+ beam; b) Data for H_2^+ beam.

CHAPTER 3

MeV ION SCATTERING

MeV ion beams have enjoyed widespread application for materials analysis for many years [Feld82; Feld77; Chu78; Van85; Sten92]. For the results presented in this manuscript, the principle tool was a 2.5 MeV beam of He^+ ions. In this chapter, some of the characteristics of ion beam analysis that make the technique attractive for the application to surface analysis are outlined. Also included is a discussion of the ways in which the ions were used in a typical experiment to probe the physical characteristics of our samples. The discussion begins with a description of a typical backscattering spectrum (in the absence of channeling) used to study the gross physical properties such as sample thickness, uniformity, composition and degree of contamination of the samples. This use represents the most basic and common one for MeV ion beams in materials analysis. The discussion then progresses to cover the ideas behind the use of channeling in the transmission geometry to elucidate the atomic structure of the surfaces of samples. Augmenting this treatment is a brief overview of the mechanisms governing the channeling process (channeling will be described further in chapter 5).

Rutherford Backscattering Spectroscopy

One of the most useful and well-established techniques utilizing ion beams is Rutherford backscattering spectroscopy (RBS) [Feld82]. There are three important properties of RBS which make it useful for materials analysis, in general, and for this study in particular. First, the technique is mass dispersive, which allows separation in energy of the signal from among impurities and from that of the substrate itself [Van85]. In practice this quality is extremely useful for the identification of unwanted sample contamination and the confirmation of the chemical makeup of the samples as

prepared. Second, by avoiding beam energies leading to non-Rutherford scattering, the process is classical, with well-defined and well-described cross sections (Rutherford), making the technique quantitative [Sten92]. This feature allows the experimental determination of impurity levels (for coverage above ~ 0.001 ML for heavy nuclei and ~ 1 ML for light). For surface studies this quantitative nature insures that the absolute coverage of surface adlayers can be determined. In fact, RBS represents one of the most accurate and trusted methods (in cases where the impurity has a larger Z than the substrate) for determining the amount of a given foreign chemical species on a surface or implanted in a near-surface region. Finally, since the rate of energy loss for protons and alpha particles in most materials has been studied extensively and is well tabulated [Zieg77], the technique affords some depth resolution. This makes RBS one of the most accepted techniques for the study of thin films (see our analysis of the Ge thin windows, chapter 4).

These considerations are summarized graphically in figure 3-1, where is shown a typical RBS spectrum (scattering angle = 150°) from a Si sample with ~ 0.95 ML of Sb on the front (beam exit) surface. In the inset the scattering geometry is sketched. This spectrum also indicates that some Sb (< 1 ML) has been deposited (inadvertently) on the back of the sample. Further illustrated is the widening of the Si signal and the separation of the Sb peaks on the two sides due to energy loss of the ions through the sample. The mass dispersive quality of the technique is clear from the separation of the Si substrate and surface Sb peaks. From such a spectrum (with a calibrated detector) one can determine accurately the thickness of the Si substrate ($\pm 5\%$), the identity of the surface "contaminant" ($\pm Z = 1$), and the amount of the contaminant ($\pm 10\%$).

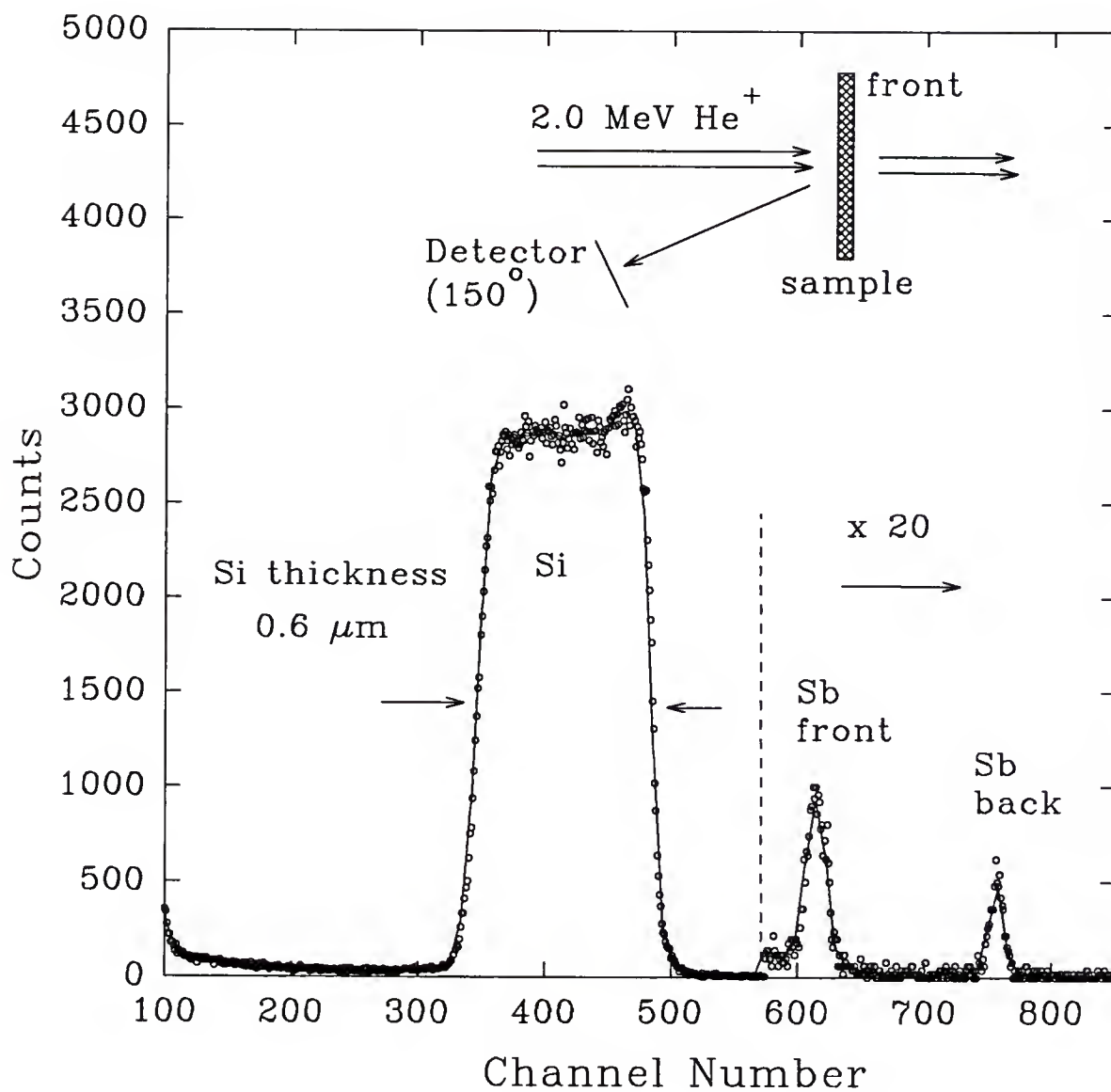


Figure 3-1. Sample RBS spectrum. The open circles are the data. The scattering geometry is shown in the inset (the front is the surface studied).

For our experiments, RBS has been used mainly to determine the thicknesses of the thin Si crystals and the amounts of given impurities adsorbed on the surfaces. For the surface coverage determinations, typically, an accuracy of 3-5% (or even 1-2%) [Van85] is attainable from RBS in a system optimized for precise quantitative impurity detection. However, in our experimental setup, designed for thin samples, implanted standards (common for achieving high accuracy [Cohe83; Wätj90]) cannot be used because we integrate current after the beam passes through the sample. Thus, our measurement of sample coverage is limited by experimental uncertainties involving current integration, detector solid angle, and counting statistics. Fortunately, knowledge of the coverage to within 10% is adequate for the studies presented in this manuscript (our setup is optimized to measure relative yields). For the thickness measurement, inaccuracies associated with the empirical, tabulated energy loss parameters provide the dominant errors. The parameters are known to within approximately 5% [Zieg77], which translates to an uncertainty of $\sim 5\%$ in a determination of the sample thickness. This level of accuracy is acceptable since the sample thickness is important in the data analysis only in that it is used in the calculation of the angular scans (chapter 5). The angular scans are relatively insensitive to differences in thickness on the present level (hundreds of Å).

Channeling

In addition to providing information on the composition of materials and the thickness of films, MeV ion beams also can be used to study the crystallinity of materials. Advantage is taken of the fact that, under the proper conditions, the spatial distribution of the ion beam can be affected drastically as it penetrates a crystalline material [Feld82]. This effect occurs because only a small fraction of the total number of ions suffer a low-impact-parameter collision at a given atomic plane ($\ll 1\%$). The vast majority penetrate farther into the crystal, where they are influenced mainly

through large-impact-parameter interactions with the host nuclei (and slightly through multiple collisions with electrons).

Indeed, if a beam of MeV ions penetrates a crystal while aligned with a major crystallographic direction, its Coulomb interaction with the atom rows causes the ions to be gently steered (the interaction is gentle in that the change in the trajectory of a channeled ion caused by any one crystal atom is small). These interactions lead to highly a non-uniform flux distribution, which is peaked at the center of the channels (flux peaking). Eventually (after $\sim 1000 \text{ \AA}$ for 2.0 MeV alpha's), the ion beam assumes the in-plane periodicity of the crystal. As a consequence of this effect (referred to as "channeling"), the probability that an impurity in (or on) the crystal will suffer a low-impact-parameter collision (i.e. will scatter an ion significantly) will depend strongly upon its position with respect to the underlying matrix (substrate). This process is illustrated schematically in figure 3-2.a. Here one channel is depicted as viewed from a direction perpendicular to the beam. The channel is defined by the rows of atoms (open circles). Several ion trajectories are sketched (not to scale), and the pileup of flux at the center of the channel is shown as the dashed curve. The motion of any given ion is controlled by the electrostatic potential in the crystal and the direction and point of entry of the ion into the channel. Interactions with the ion rows are largely characterized by repeated, correlated collisions which occur over the distance of hundreds of atoms [Lind65].

The experimental manifestation of the channeling process is a greatly reduced scattering yield from the substrate for channeled beams. This effect is shown in figure 3-3. Here, spectra are shown for a 2.0 MeV beam of He^+ ions incident on Si, aligned (solid curve) with the $\langle 100 \rangle$ axial channeling direction ($\langle 100 \rangle$ crystallographic direction), and in a random direction (dashed curve) near the $\langle 100 \rangle$ axis (7° tilt of the beam with respect to the crystallographic axis). Although taken on the same sample,

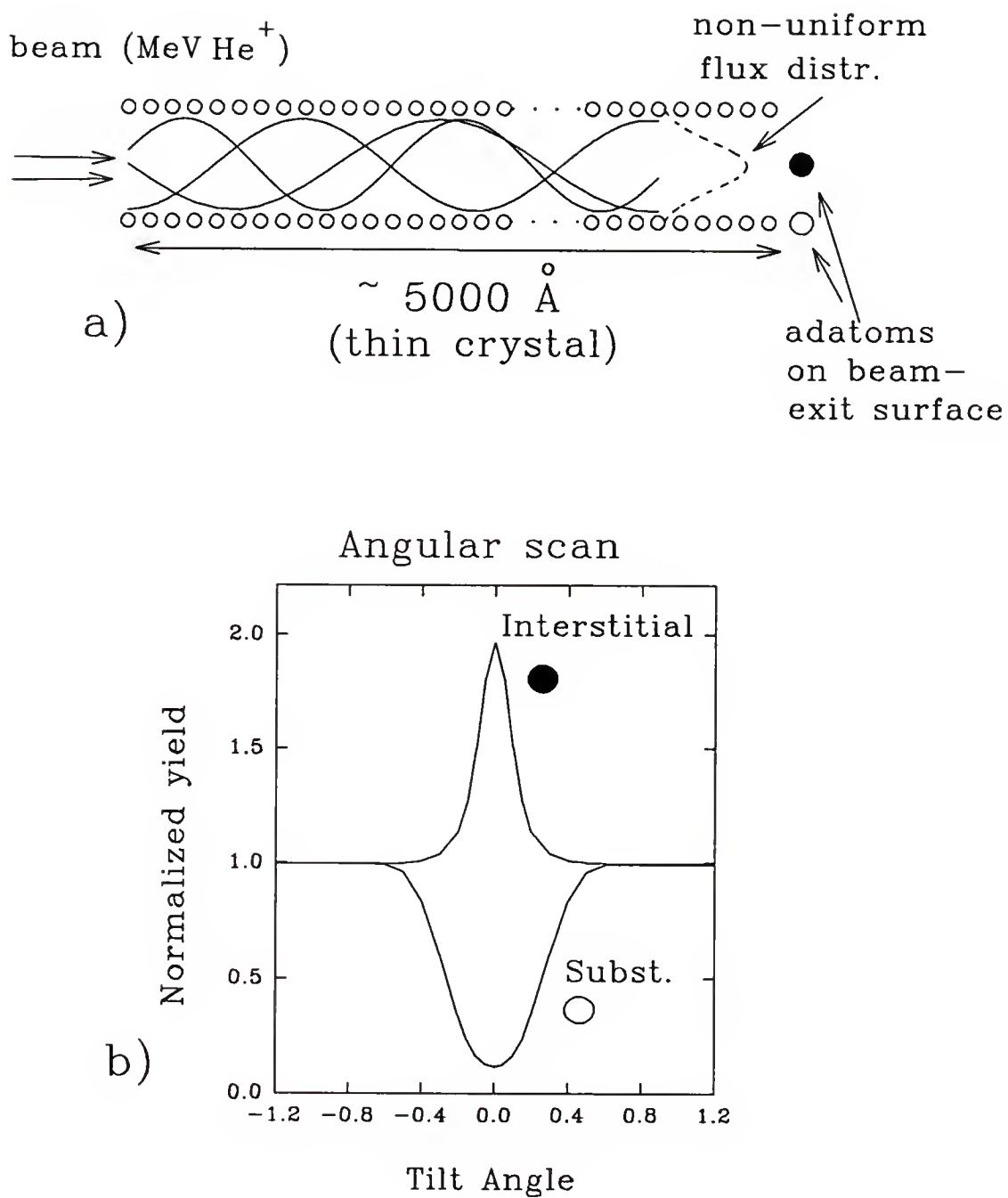


Figure 3-2. Schematic illustration of channeling. a) Channeled particles (represented by solid lines) leading to flux peaking (dashed line); b) Angular scans for those adatom positions indicated in a.

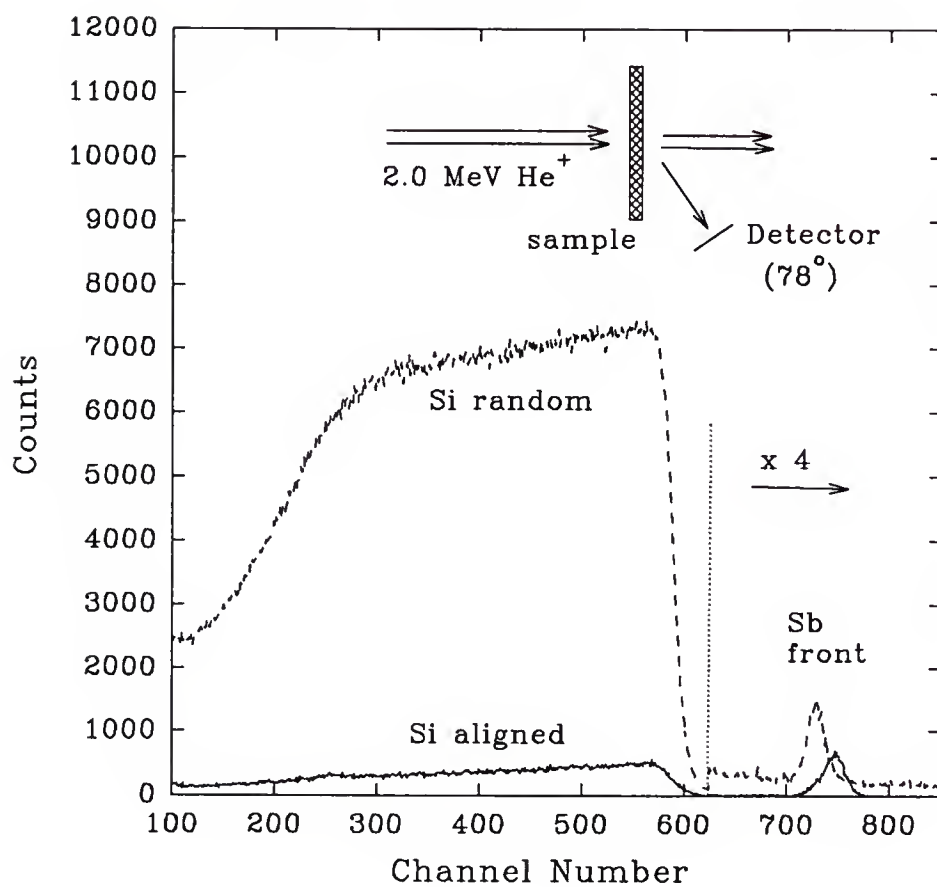


Figure 3-3. Sample spectrum from 78° spectrum. Spectra for both random (dashed curve) and aligned (solid curve) incidence are shown. The scattering geometry is given in the inset (the surface of interest is toward the detector).

the random spectrum shown here differs in appearance from that in figure 3-1 (RBS spectrum) because the scattering angle is 78° (as compared to 150°). The scattering angle affects the data in several ways. First, the path length of a scattered ion through the Si is increased, due to the glancing view the detector has of the sample. This increased path length causes a corresponding larger energy loss for scattered particles. For this reason the Si signal appears much thicker (occupies more of the horizontal axis), and obscures the Sb peak from the back of the sample. Also, the mass resolution is reduced due to kinematics [Gold80], which moves the Sb and Si signals closer together. Another effect is an increased cross section, which leads to a greater scattering yield for a given solid angle. In figure 3-3, however, the reduction in the yield for the aligned spectrum, as compared to the random, is completely a channeling effect.

In channeling, the flux distribution is also a function of the tilt angle, ψ , of the beam with respect to the axial channeling direction. It is the combined dependence of the scattering yield on position, and this dependence of the flux on ψ , that is used in transmission ion channeling for adatom site determination. In practice, this determination is accomplished by a comparison of the experimentally determined scattering yield as a function of ψ , an *angular scan*, with computer-calculated angular scans. Also shown in figure 3-2.a, are potential bonding sites for adatoms on the beam-exit side of the thin crystal (large circles). Figure 3-2.b then shows angular scans for such positions. Note that, due to the flux peaking, an interstitial site will exhibit an enhanced yield in the channeling direction ($\psi=0$), while a substitutional site will show a reduced yield (Si occupies, by definition, a substitutional site). At larger tilts, the yield for each of these sites approaches that for random incidence (defined as 1). Of course, a whole range of adatom sites, and, hence angular scans, is possible. Qualitatively, much can be inferred about the adatom bonding sites from a

consideration of the shapes and depths of such angular scans. For a quantitative determination of the bonding site, however, experimental and computer-calculated scans are compared.

An important consideration concerning the experimental angular scans is the angle of tilt of the beam with respect to the given crystallographic direction, ψ . In principle, it is necessary to know precisely the exact angular position at which each spectrum is acquired with respect to the crystal (this defines the so-called "crystal coordinates"). In practice, however, systematic uncertainties introduced by the physical makeup of the goniometer and sample mounting conspire to make this knowledge difficult to obtain with precision. These effects can be accounted for and the crystal coordinates calculated after a lengthy calibration of the experimental setup [Dygo93]. However, such precision is difficult to maintain reliably for our setup, and is unnecessary for characterizing small tilts about a known direction. Since we used angular scans over only $\sim 2^\circ$, and since we can determine accurately the coordinates of the axial direction, our main concern then becomes the execution of angular scans across the axial channel in an appropriate direction. For these studies, care was taken to conduct the scans in a so-called "random plane". Such scans are meant not to coincide with nor intersect (except at tilt = 0) any major crystallographic planes of the crystal.

In order to avoid problems associated with planar channeling, one has to be able to determine the positions of the planar directions. Since we use thin crystals, which allow the beam to pass through the sample, the requisite determination is possible. After passing through the sample, the beam enters a faraday cup and can be made to strike a piece of quartz (in front of a 2.75" viewport). Beam alignment is then accomplished by viewing the distinct patterns on the quartz, which fluoresces when struck by MeV ions, as a channeling direction is approached [Arms71]. This

phenomenon expedites the aligning of the sample along an axial channeling direction, because the ion beam forms a doughnut pattern as the axial direction is approached [Gemm74; Rosn78]. Aligning the sample in this way with any axial or planar channeling direction can be accomplished with great accuracy in less than 1 min. and with a beam current of less than 10 particle nA. Angular scans are then planned in order to avoid the planes. For the $\langle 100 \rangle$ axial channeling direction, the ϕ degree of freedom has a relatively minor affect on the actual tilt angle because the ϕ axis is nearly parallel to the beam (see figure 2-2 for the definition of the angular degrees of freedom θ and ϕ). Therefore, scans are conducted by tilting in θ . Since the angular positions of the planes will depend upon the orientation in which the sample is mounted, the planes are avoided by choosing the proper orientation of the sample module on the goniometer [Lyma91a]. Several orientations often are tried before a $\langle 100 \rangle$ scan is completed. For the $\langle 111 \rangle$ direction, the angle between the sample normal (approximately the ϕ axis) and the beam is $\sim 55^\circ$. Therefore, in this channeling direction the crystal is oriented reproducibly with respect to the beam from run to run. Also, no major plane is encountered for tilts in ϕ , so the scans are conducted with ϕ movement. For the $\langle 110 \rangle$ direction, again, the sample is oriented reproducibly. However, tilts in only θ or only ϕ both coincide with planes in the crystal. Therefore, scans are conducted using tilts with both angles. This procedure is illustrated in figure 3-4, which displays a contour plot of the Si yield obtained at tilts about the $\langle 110 \rangle$ axial direction. In this figure, the effect of planes crossing the axial channeling direction is seen clearly. This contour plot was constructed from a data set composed of 763 spectra, taken on a grid in θ and ϕ , in the RBS chamber (this chamber has a goniometer which is identical to the one in the UHV scattering chamber). Also shown as the symbols (*) is a superposition of the cut typically used to acquire data across

this axial direction. This cut is seen to avoid adequately the major planes, satisfying the conditions defining a random plane.

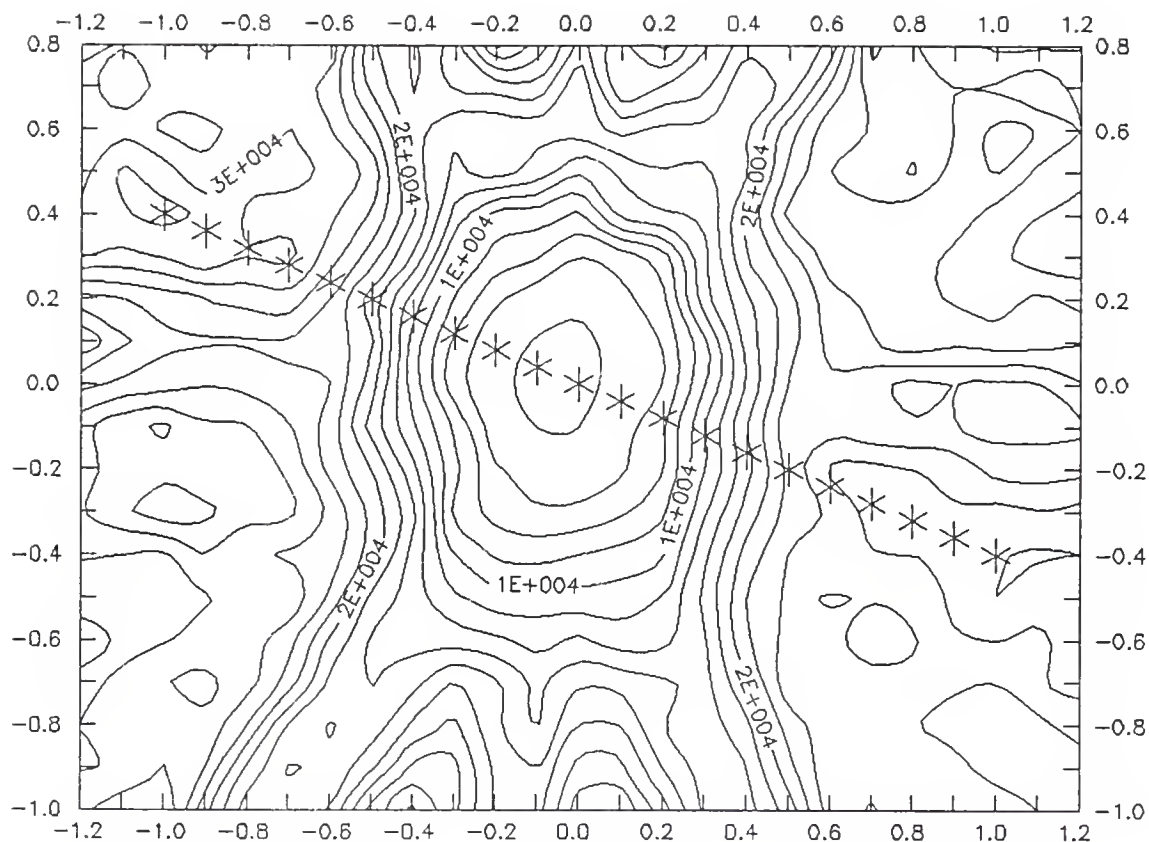


Figure 3-4. Plane of scan for $\langle 110 \rangle$ axial channel. The horizontal axis represents the θ degree of freedom, and the vertical axis ϕ (units are degrees). The plane of the angular scan is shown as the symbols (*). Each contour represents 2000 counts.

CHAPTER 4

SUBSTRATE PREPARATION AND CHARACTERIZATION

Transmission ion channeling necessitates the use of thin (from $0.2\mu\text{m}$ to $2.0\mu\text{m}$), single crystals that are able to withstand manipulation (for sample loading, etc.) and thermal cycling (for cleaning, sample preparation, etc.). There exist recipes for making such windows of a variety of materials. For example, thin Ni windows in the (100) orientation have been produced by epitaxial growth of metal onto single-crystal NaCl, followed by flotation of the film from the salt and onto a frame in water [Jens90]. Similar procedures have been utilized to produce thin crystals of Al, Cu, Pd, Pt, W, Ag [Jens90], and Ge [Outl84]. The experiments presented in this discussion were conducted on the Si(100) surface. A suitable technique for the production of thin Si windows was described in the literature by Cheung [Cheu80]. The procedure, as carried out in our laboratory, has also been described in detail [Lyman91a], so only a brief overview will be given here. The basic idea is to employ a selective etchant which ceases to etch Si when its dopant level is sufficiently high.

At a certain point in time, it became desirable also to have thin Ge windows available for transmission ion channeling studies. Although the use of self-supporting Ge crystals several microns thick had been reported in connection with nuclear physics experiments [Gibs72], no published literature described their fabrication, uniformity or crystalline quality. Free-standing single-crystal Ge films fabricated by epitaxial growth onto NaCl and separation from the substrate by differential shear stress had been reported [Outl84], but were substantially thicker ($10\mu\text{m}$) than desirable and were therefore unsuitable for use in transmission ion channeling. After considerable effort, an appropriate procedure was developed for the in-house fabrication of suitable windows [Gran93d] in collaboration with Dr. F. Namavar at Spire Corporation.

Although the Ge windows have not, as yet, been used for surface studies in this laboratory, their fabrication and characterization are described below, since a substantial effort was expended towards their development. Utilization would constitute a logical extension of the experiments contained herein.

Thin Si Windows

Chemical Preparation.

As received, a Si wafer is 2" in diameter, $\sim 200\ \mu\text{m}$ thick, and typically is doped lightly with Sb. After a brief cleaning step, Boron is deposited on the polished surface (suspended in an organic solvent) and diffused into the surface region of the wafer in a tube furnace (at 1050°C , under flowing, dry N_2). After the diffusion is accomplished, the wafer is cleaved into $1.3 \times 1.3\ \text{cm}$ samples and each is etched into a thin window in two steps. The first step removes Si from a circular region on the back (unpolished) side of the sample to a thickness of $\sim 5\ \mu\text{m}$. The second step selectively etches the remaining n-type Si until reaching the n^+ region of high ($5 \times 10^{19}\ \text{B}/\text{cm}^3$) Boron concentration, at which point etching essentially stops [Bohg71]. These steps are outlined schematically in figure 4-1. After the thin windows are produced, a lengthy *ex situ* cleaning process is employed to remove any metallic and carbonaceous surface contaminants. That process is very similar to that described by Ishizaka and Shiraki [Ishi86] (referred to as the "Shiraki oxide" technique), which leaves the Si protected by a thin oxide ($\sim 5\text{-}10\ \text{\AA}$). Our *ex situ* cleaning procedure does differ in a few details, and therefore is outlined in appendix A. The oxide which results is free from impurities within the sensitivity of AES (see below), and is desorbed *in vacuo* by radiative heating.

Surface Cleanliness

Before surface experiments are performed on a sample, and after the oxide desorption, it has to be insured that the clean surface is of high crystalline quality and

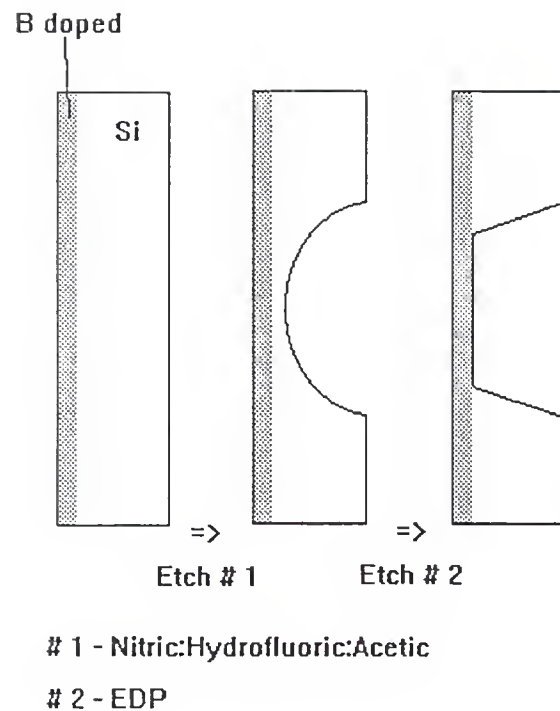


Figure 4-1. Sketch of samples at various stages of preparation (cross sectional view, not to scale). Etch #1 constitutes the gross removal of Si. Etch #2 is selective, removing only the lightly doped Si. The thick, unetched region surrounding the window is used as a supporting frame.

is atomically clean. To this end, the surfaces are characterized by AES and LEED. Both of these techniques are established and extremely useful for the surface scientist. Both utilize the short escape depth of the exiting electrons to achieve a high surface sensitivity [Wood86, chapter 3]. To produce the escaping electrons, AES relies on the excitation of core-levels and their subsequent decay, which can kick out Auger electrons [Davis78]. This excitation is accomplished in most cases, including ours, by a focused keV electron beam [Davis78]. While keV electrons are efficient at knocking out core-level electrons, they also effectively heat the substrate. For thick semiconductors, the heat is carried away readily. For the samples we use, however, the heating by the electron beam is drastic enough to burn holes in the thin windows. Therefore, none of the AES spectra discussed in this work was taken on thin windows. Instead, spectra typically were acquired on the thick frame next to the window, or during separate runs on thick crystals. We have no reason to think that these Auger spectra are not characteristic of the elemental composition of the surface on the thin windows prepared similarly.

LEED allows an evaluation of the degree of order and the symmetry of the atomic arrangements on the surface [Zang88, chapter 3; Wood86, chapter 2] and is accomplished by diffraction of a low-energy electron beam from the surface atoms. Because of the low energies employed in LEED (10-100 eV), no such heating problem has been encountered. LEED has been used to monitor the cleanliness and uniformity of substrates as measured on the thin windows themselves for all samples discussed.

Both LEED and AES indicate that our Si(100) sample surfaces, after the thermal desorption of the oxide, are clean and well ordered. LEED shows the two-domain 2x1 pattern characteristic of this surface [Feld86, p. 167; Schl59; Hame86] for most samples. Although the quality of the patterns varies from sample to sample, typically they are sharp and the background low (high background or diffuse spots are

indicative of disorder [Wood86, p. 38]). Occasionally, a sample is overheated, leading to the appearance of satellite spots in the pattern, possibly because of faceting [Hame86] or B segregation [Lyma91a]. B segregation has been shown to alter the reconstruction on the Si(111) surface [Bens89]. Data from such samples were not used in the analysis. Auger spectra indicate that the oxide, before thermal desorption, is free of impurities. Spectra taken after desorption also typically show little contamination. This trait is illustrated in figure 4-2, which shows Auger spectra before and after oxide desorption on a Si(100) sample. The positions of common contaminants, C and O, are indicated. This spectrum is particularly clean, as it is not uncommon to observe a C peak above background, due mainly to the buildup of C on the surface as a function of electron bombardment.

Crystallinity

Transmission ion channeling studies rely on the crystalline properties of the substrate of interest. The technique, however, is comparatively insensitive to defects in a crystal. This insensitivity is evidenced by our channeling studies for highly doped Si. Although the doping level (5×10^{19} B/cm³) has a tremendous impact on the electronic properties of the Si, this level represents only one part in 1000 atomic impurities, and would not be expected to influence channeling measurements significantly. The indicator of good crystalline quality, as measured by channeling, is the minimum yield. Table 4-1 shows measured values of the minimum yield for a number of samples taken over a period of ~ 2 years, along with the standard deviation, and number of measurements. These values were taken from data for which there was available an angular scan, to help insure that true alignment of the beam with the axial direction was obtained. Also shown are calculated values for the different channels using a formula arrived at from Monte Carlo simulations of the channeling process [Feld82, p. 44].

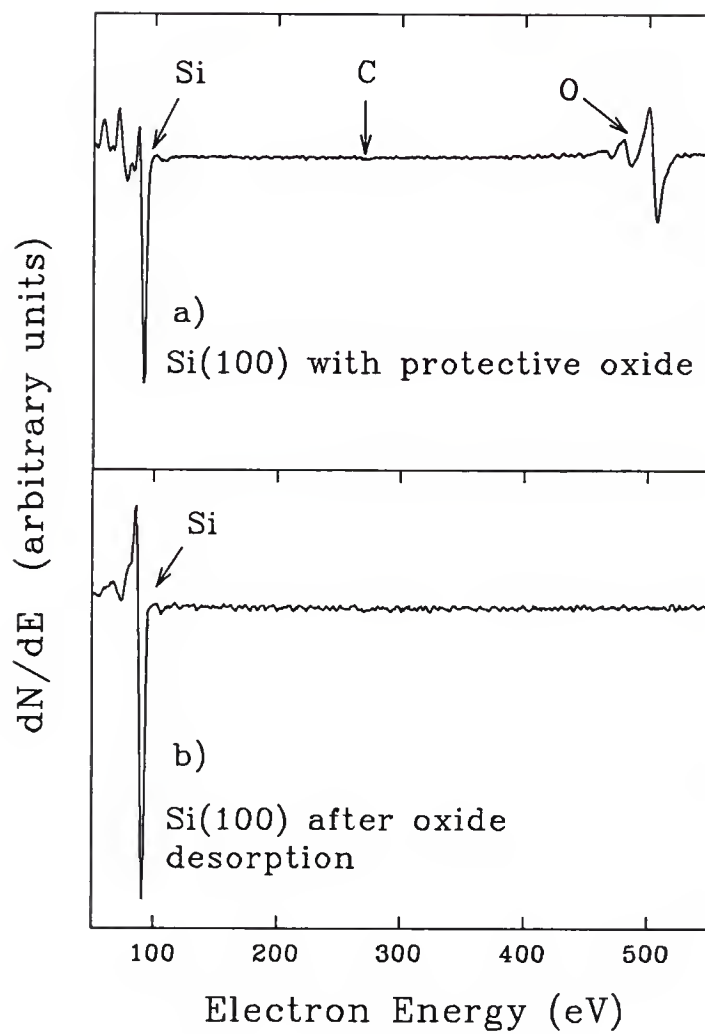


Figure 4-2. Sample Auger spectra from Si(100) surface. a) Before oxide desorption; b) After oxide desorption.

Table 4-1. Si channeling minimum yields

direction	χ_{\min}	σ	#	calc. [†]
<100>	0.048	0.013	22	0.033
<110>	0.038	0.012	15	0.023
<111>	0.050	0.013	23	0.028

[†]The <110> and <111> values were scaled from the <100> value [Feld82, p. 45] with d (linear string density).

Our measured values of the minimum yield are seen to agree reasonably well with the calculated values. For our measurements, the minimum yield is found by integrating the total counts in the Si peak (50° detector) from scattering throughout the ~ 5000 Å thickness. Due to dechanneling of the beam with thickness, our values are expected to be higher than the calculated values, which give the minimum yield just after entering the crystal (see figure 5-7). Also, for our measurements, there exists a finite beam divergence, which serves to increase the minimum yield slightly [Gemm74]. Overall, we conclude that the crystalline quality of a typical thin Si window as produced in the manner described above is adequate for the studies detailed herein.

Thin Ge Windows

Fabrication

Using an Applied Materials 1200 epitaxy reactor at atmospheric pressure, epitaxial Ge layers with thicknesses of 0.5 - 4.0 μm were grown at Spire Corporation on clean Si(100). Prior to Ge growth, to produce clean Si surfaces, the samples were heated to 1200 °C for 1/2 hour and then etched *in situ* by passing HCL over the surface until approximately 1 μm of the Si was removed. Germanium tetrachloride (GeCl_4) was used as a Ge source for growth on these substrates, with the growth rate ranging from 0.5 to 1.0 $\mu\text{m}/\text{min}$ and growth temperatures from 750°C to 850°C. Transmission Electron Microscopy (TEM) and cross-sectional TEM (XTEM) were used by Dr. Namavar at Spire to determine defect densities in the layers. A typical

XTEM micrograph of the as-grown Ge film is shown in figure 4-3. The micrograph shows a defective region of misfit dislocations extending from the Ge/Si interface 2000 - 3000 Å toward the surface. A region of high crystalline quality extends about 5000 Å from the surface. A plane-view TEM survey of a large area near the surface of the sample indicates a defect density in the range of $10^6/\text{cm}^2$ [Nama91]. This defect density, low for epitaxial Ge layers on Si(100), is attributed to a high dislocation glide velocity at the relatively elevated growth temperatures employed in CVD [Kvam91; Nama90]. The defect density is below that detectable by ion channeling.

In order to produce thin windows, several etching steps (outlined below) were applied to the as-grown samples. The state of the sample after the successive steps is schematically illustrated in figure 4-4. After the Si(100) wafers with the Ge grown on them were received from Spire, they were cleaved into 1.3 cm by 1.3 cm squares, and the front (Ge) and back (Si) of the sample were masked completely in Parafilm (Parafilm is made by Dixie/Marathon, Greenwich, Conn.) except for a small (~2mm) hole in the center of the back. Then the first etchant, which consisted of $\text{HF}:\text{HNO}_3:\text{CH}_3\text{CO}_2\text{H}$ (2:4:1 volumetric ratio), was applied. It was used to etch the unprotected region to a thickness ranging from a few to tens of microns. This part of the sample preparation was similar to that applied in the selective etching of doped Si for the production of thin Si windows. The purpose of this step was to create a bowl-shaped cavity in the Si, both to act as a template for the final window, and to expedite the etching in subsequent steps. For the fabrication of Si windows this step is terminated when light from a high intensity lamp is visible through the thinned Si, however Ge is opaque at these thicknesses, preventing the use of this method. The hope during this step was to come as close to the Si-Ge interface as possible, without etching the Ge (or etching entirely through the sample), which was accomplished (roughly 25% of the time) by careful calibration of the etch rate under controlled



Figure 4-3. Plan-view cross-sectional transmission electron micrograph of 1.2 μm Ge film on Si substrate. The defective region is visible as the dark area.

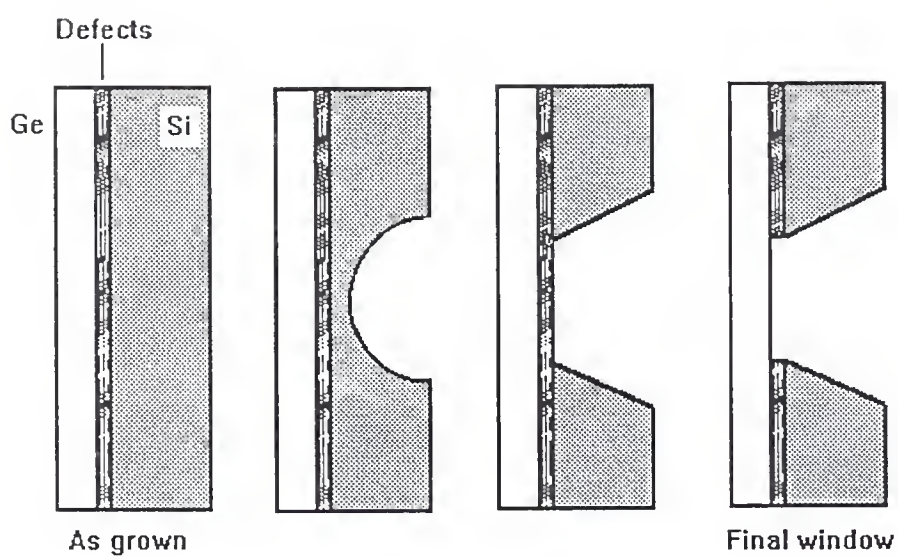


Figure 4-4. Illustration of Ge thin window etching steps. Step one removes large quantities of Si. Step two employs a selective etch which does not remove Ge. Step three is not selective, but is brief and removes the defective region from the back of the window.

experimental conditions. The length of time required in this etch bath to reduce a 400 μm wafer to a few microns was ~ 25 min. Next, the Parafilm was removed, and the sample was submerged in a solution consisting of ethylenediamine: H_2O :pyrocatechol (EDP) in the ratio 50 ml:25 ml:10 g, held at 85°C , which etches Si at a rate of about 50 $\mu\text{m}/\text{hour}$ but etches Ge at a negligible rate. The samples were left in this solution until the Ge/Si interface was reached, which was indicated by the appearance of a flat, blue-tinted region in the center of the etch pit. It was found that KOH increased the window size more quickly and gently than continued etching in the EDP, so the samples were removed from the EDP just after the interface was reached and were placed in a 10 Normal solution of KOH at 85°C until of suitable diameter. In this manner, samples of up to ~ 6 mm in diameter were produced (although the larger samples were not tested for durability under ion irradiation). After these steps, the sample consisted of a uniformly-thin Ge window backed by a defect-ridden region and surrounded by a thick Si frame (third panel in figure 4-4). Finally, the defective region was removed from the back of the window by masking the front of the sample in Parafilm (without contacting the thin part) and dipping it briefly (~ 6 sec) in a mixture of HNO_3 :HF (20:1 volumetric ratio).

Characterization of Crystallinity

RBS with channeling was used to further characterize the structure of the windows. Ion beam analysis of the Ge windows was accomplished in a high vacuum ($\sim 10^{-6}$ Torr) ion scattering chamber connected to the UF Van de Graaff accelerator and equipped with a goniometer having two stepper-motor-controlled angular degrees of freedom. For the data presented here, the beam was 2.0 MeV He^+ and a surface barrier detector was placed at a scattering angle of 170° . Figure 4-5 shows a channeling spectrum (solid circles) for a 1.2 μm Ge epilayer on Si exposed to the etching procedure described above, including the removal of the defective region.

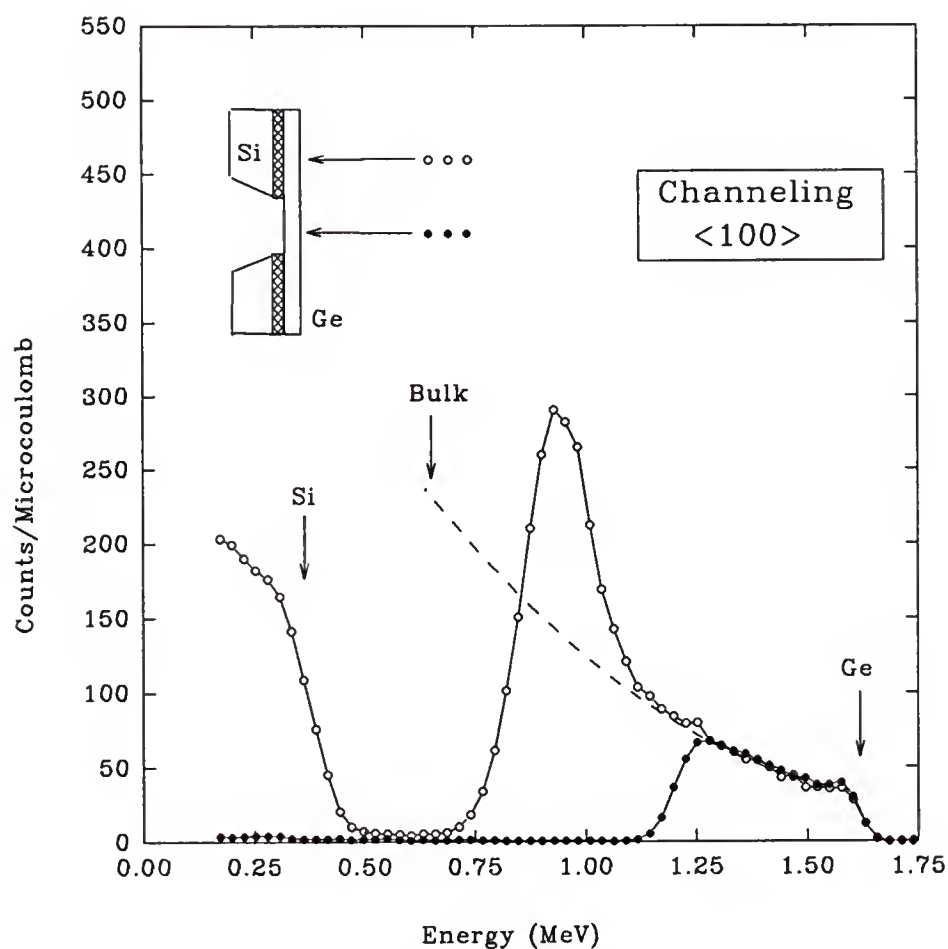


Figure 4-5. Channeling spectra from Ge thin window. The open circles represent scattering from the thick (unetched) portion of the sample. The filled circles represent scattering from the thin window. The dashed curve is from a channeling spectrum obtained from a bulk Ge crystal. The peak in the spectrum from the thick region (open circles) is due to the defect-ridden region, which has been removed from the back of the thin window (filled circles).

Channeling spectra of the unetched sample (open circles) and of bulk Ge (dashed curve) are shown for comparison. The two spectra were taken on the same sample, the former on the thick frame surrounding the thin window and the latter in the center of the window (see inset). The peak in the channeling spectrum from the unetched sample near 0.95 MeV is the result of ion beam dechanneling by defects in the Ge layer near the Si-Ge interface [Feld82, chapter 4], as well as direct scattering of the ion beam by the distorted channels near defects [Wiel86, Quer68]. A detailed analysis of the effects leading to this peak is given in appendix B. A visual inspection of figure 4-5 indicates that the etching process removed the Si substrate and the defective region of the Ge epilayer. The Ge minimum yield on the window is clearly as low as that in the unetched region, and as low as that for bulk Ge, indicating that the crystalline quality of the Ge epilayer is comparable to that of the bulk crystal in the region near the Ge surface. Channeling spectra on the window have also been taken with the beam entering through the back (etched side) of the Ge and are indistinguishable from that shown in figure 4-5. This implies that the crystalline quality of the window at the back is comparable to that at the front, and further indicates that the defective region has been completely removed. If the defects had not been removed, immediate dechanneling as the beam entered the crystal from the back would lead to a dramatic increase in the yield throughout the sample thickness.

In figure 4-5, the bulk spectrum (dashed line) and the spectra from the thin window sample were obtained in separate experiments. For the bulk experiment, the beam was aligned with the Ge $\langle 100 \rangle$ axial channel using the standard procedure [Chu78, p. 228] of determining the polar coordinates of several major planar channeling directions, plotting these points on polar graph paper, and identifying the axial direction as the point of intersection of the planes. This procedure was time consuming (several hours), so, to minimize the influence of beam damage and carbon

buildup, the beam spot was changed before retuning the channeling direction (~10 min.) and taking the spectrum shown. In contrast, the procedure used for aligning the beam on the Ge window was similar to that employed with the Si windows (discussed in chapter 3). However, for the Ge case (due to the thicker windows and increased stopping power of Ge over Si [Zieg77]), the pattern on the quartz viewport was visually less distinct. Although this had the effect of decreasing the precision with which we were able to align the beam, with care the alignment was accomplished satisfactorily, as is indicated by the low minimum yields obtained.

Using RBS, it is easy to estimate the thickness variation of the thin windows. Due to statistical fluctuations in the processes governing the amount of energy lost by energetic ions traversing a crystal, an ion beam having an energy distribution which can be approximated by a delta function upon entering the crystal will have a different energy distribution at a thickness t . This effect is termed energy straggling. It has been shown that this distribution (except at small t) can be well-described by a Gaussian, with variance given by Bohr theory [Bohr15] as,

$$\Omega_B^2 = 4\pi(Z_1 e^2)^2 N Z_2 t. \quad (4-1)$$

Here, Z_1 and Z_2 are the atomic numbers of the incident ion and target, respectively. The falling edge of a random spectrum taken from a thin film is broadened by contributions from a finite detector resolution, energy straggling through the sample, and nonuniform sample thickness. A random spectrum from the Ge window was used to estimate the thickness variation of the window over an area the size of the beam spot (1 mm²). Figure 4-6 shows the numerical derivative of the spectrum (dots) in the regions of the beam entrance and beam exit of the window and Gaussian fits to each peak (solid lines). The fit to the beam entrance peak yields the energy resolution of the system at the beam entrance, Ω_D . The quantity Ω_D includes detector resolution

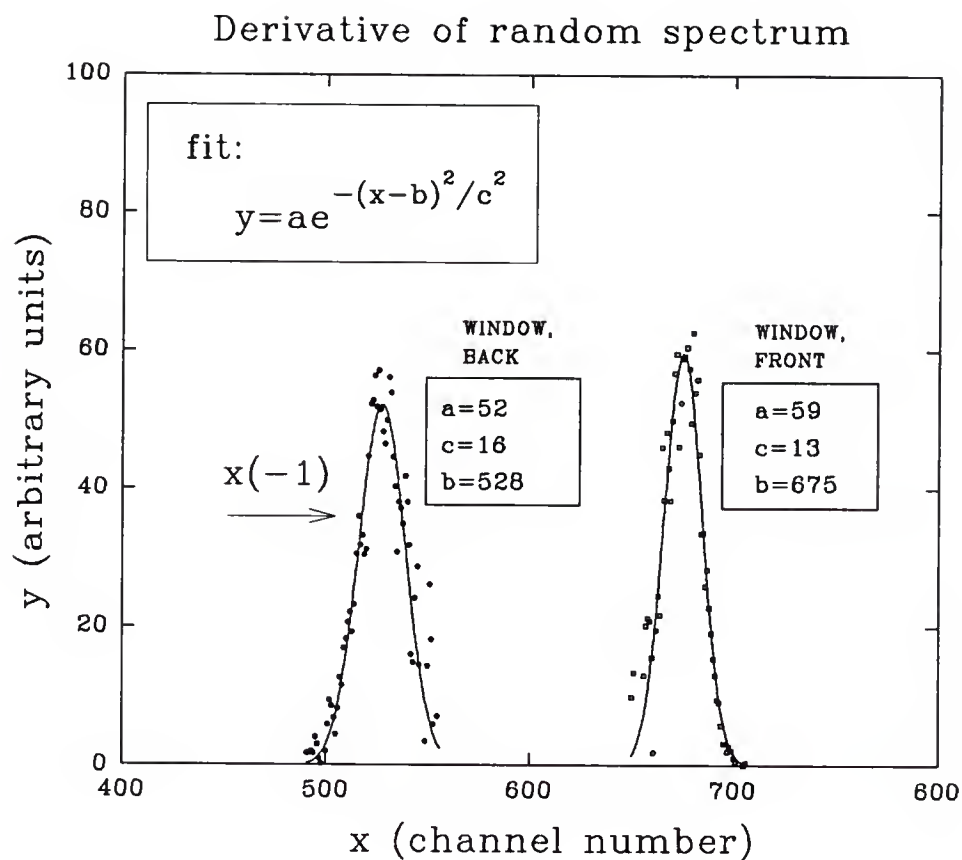


Figure 4-6. Numerical derivative of random spectrum from Ge/Si sample. Portions of the derivative of the spectrum are shown. Since the rising and falling edges of RBS spectra take the form of error functions, the derivatives of these regions are Gaussian [Chu78, p. 50]. The functional form used to fit the peaks is given, along with the value obtained for the fitting parameters.

(dominant), the energy spread of the incident beam, and contributions from the electronics. Equation (4-1) yields the variance due to straggling at the beam exit surface. All of these contributions can be treated as Gaussian, so they add quadratically,

$$\Omega^2 = \Omega_D^2 + 2\Omega_B^2 + \Omega_t^2. \quad (4-2)$$

Here, Ω is the width of the Gaussian at the beam exit side in figure 4-6, and represents the apparent resolution at t . Using this, we place an upper limit on the thickness variation of the window (Ω_t) within the area of the beam spot of 8% for this sample.

Surface Cleaning

Shown in figure 4-7 is a portion of an AES spectrum taken near the edge of (but not on) a Ge thin window before any *in situ* cleaning steps. There are clear peaks from several elements: C, O, Cl, and Ge. These peaks, plus the absence of a LEED pattern, indicate that the surface is covered by a disordered layer of various impurities, probably composed of organic molecules and Ge-C, Ge-O species. We have successfully sputter-cleaned the thin Ge windows using 1.5 keV Ar bombardment (emission = 22 mA at a pressure of $\sim 5 \times 10^{-5}$ Torr and for a beam rastered over ~ 2.5 cm²). A spectrum from the sample of figure 4-7 after 2 cycles of sputtering and annealing is shown in figure 4-8. In contrast to the sample before cleaning, after cleaning, impurities give no signal above background. From this spectrum the O level is estimated to be below 0.4%, with C below 0.3%. Sputtered samples have been annealed to approximately 600°C. These samples typically yielded sharp 2x1 LEED patterns with low background and with 4th order streaks, as observed by other groups (for instance [Culb86]), indicative of the of c4x2 domains and hinting at the transition (from 2x1 to c4x2) which has been observed on this surface just below room temperature [Culb86, Keva85]. Further, we have found that such a Ge window

exposed to a channeled 2 MeV He ion dose of $42 \mu\text{Coulombs}/\text{mm}^2$ shows no degradation in crystalline quality (as measured by ion channeling). Since a typical dose required for an energy spectrum is 6 to $12 \mu\text{Coulombs}$, the windows meet all criteria necessary for use as substrates for transmission ion channeling.

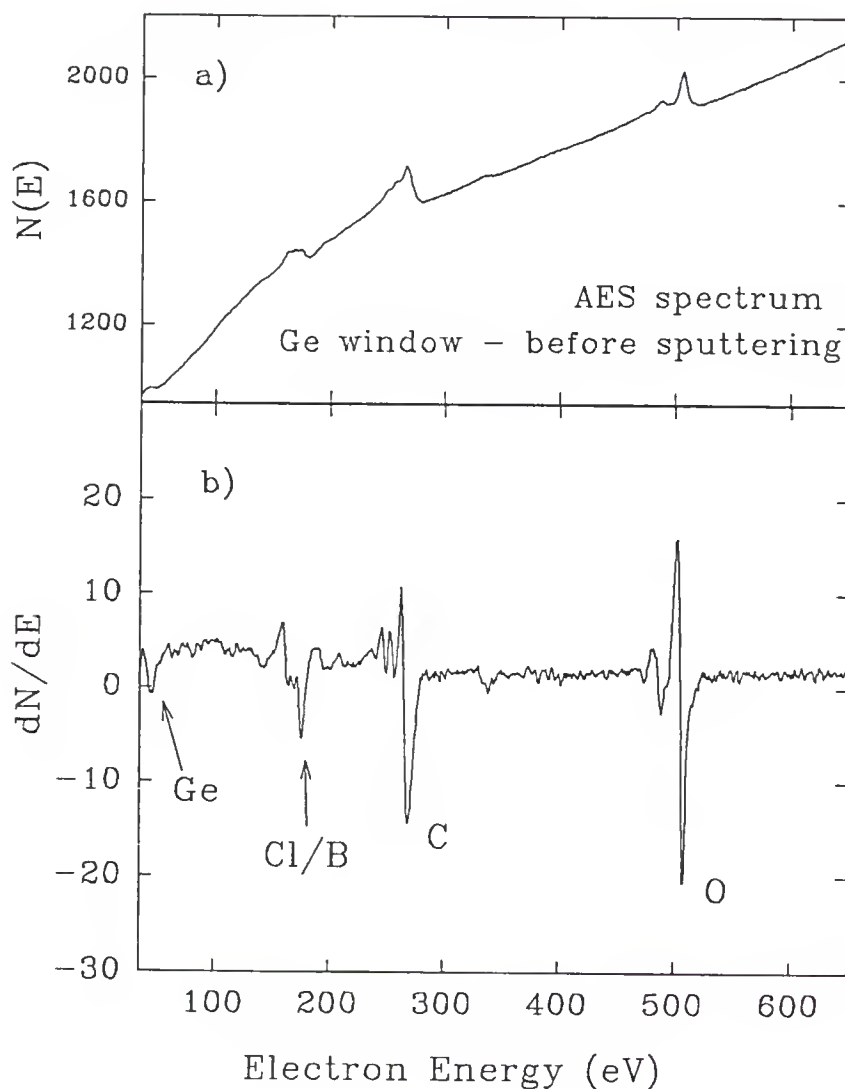


Figure 4-7. Auger electron spectrum from a Ge-window sample before cleaning. a) Raw counts versus energy, $N(E)$; b) Spectrum as typically displayed, dN/dE (surface impurities are indicated).

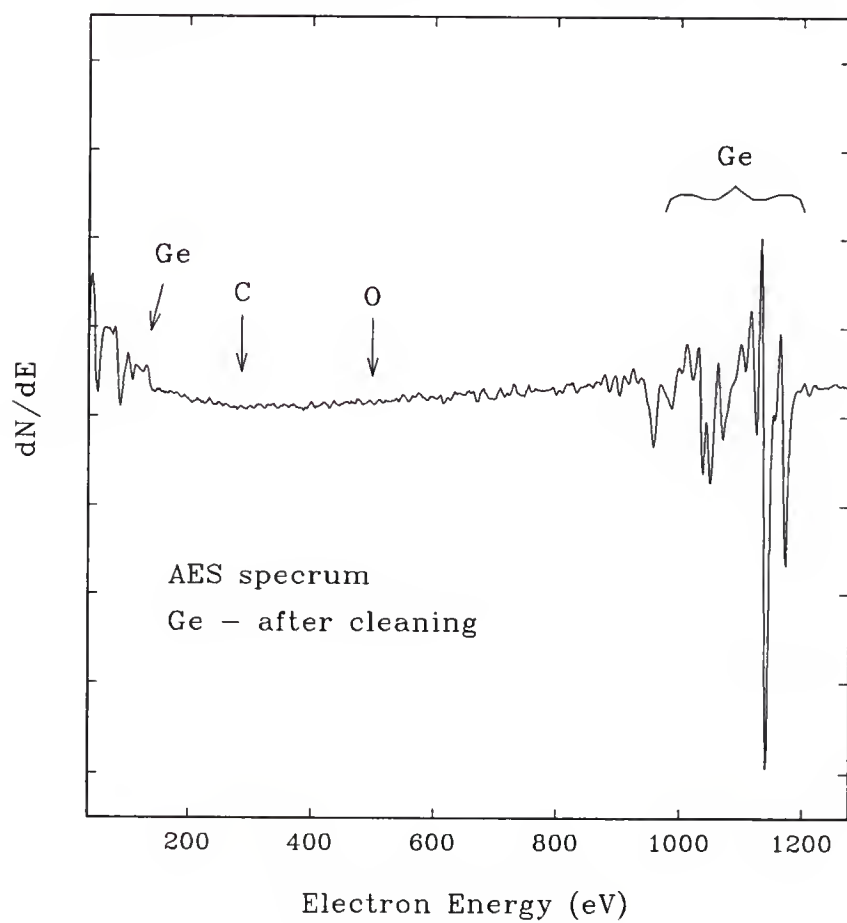


Figure 4-8. Auger electron spectrum from Ge-window sample after sputtering and annealing for two cycles.

CHAPTER 5

CHANNELING CALCULATIONS

The basic motivation behind the use of computer-calculated angular scans for the interpretation of channeling data is clear. On the one hand, experimental angular scans provide a very direct glimpse at the registry of the overlayer with the substrate. This assertion is true because, for channeled beams, the ion flux varies tremendously over any given axial channel (discussed below), and therefore can give large variations in the scattering yield from spatially differing bonding sites. On the other hand, achieving the level of precision demanded by the current state of surface science requires an intimate knowledge of the flux distribution in any such channel, a distribution which is not readily measured in a typical experiment. The solution has been to reproduce the flux using computer calculations of the channeling process.

There are two basic methods employed to find the distribution of channeled ions in crystals. One method is to simulate the channeling process with some sort of Monte Carlo technique. In this process, ions are sent into the crystal at random positions and their trajectories followed. The yield from impurities in (or on) the crystal is then obtained readily by simply keeping track of how many ions get sufficiently close to the proposed position of the impurity to scatter. Another method is to formulate some sort of analytic expression for the flux distribution in the crystal, and calculate the overlap of the proposed impurity site with the distribution. The code used in this thesis work is based on the latter idea. It employs a numerical solution to the analytic equations describing the flux distribution in three axial channeling directions ($\langle 100 \rangle$, $\langle 110 \rangle$ and $\langle 111 \rangle$) of, in this case, Si.

In this chapter the methods employed in the calculation are outlined, and a discussion is given of the assumptions made. Also discussed is the method used to

determine the projected adatom sites in the off normal ($\langle 110 \rangle$ and $\langle 111 \rangle$) channeling directions. This treatment is included since it is a crucial step in the interpretation of the calculated scans in relation to the experimental data, and thus the determination of the bonding site. Several discussions of the reduction of data using simulations of the channeling process exist, including those by Gemmell [Gemm74] and Morgan [Morg73].

Calculated Yields

Methods involving the analytic solution of the flux distribution in a channel usually are based on two simplifying assumptions. First, it is assumed that the rows of atoms can be approximated by lines of charge of the appropriate linear density. Second, it is assumed that statistical equilibrium for the ion beam is approached in the crystal. With the first, the problem becomes two-dimensional. The second allows one to write an expression for the flux distribution in a given channel. The code used for this study is based upon these two assumptions. It was developed by B. Bech Nielsen at Aarhus, Denmark and was acquired from him in April, 1991 [Bech88a, Bech88b]. The code was tested, comments added, and modified [Hoog92] by a visiting student, J. Hoogenraad, before being used for these studies. Modifications concerning the calculation of angular scans made by him and made afterwards were largely superficial. The discussion that follows, unless otherwise stated, concerns this code, which is in four main parts AREA.FOR, DFUNC.FOR, DIFFMA.FOR, and XMINN.FOR.

Assumptions

Continuum approximation. As an MeV ion beam enters a crystalline solid the vast majority of collisions with the atoms making up the solid are gentle, high impact parameter collisions [Lind65]. If the direction of the beam is close to ($\pm \sim 0.5^\circ$) that of a low-index axis of the solid, then, to a given ion, the atoms of the solid appear to be arranged in a periodic array of rows. These effects combine and lead, for most ions

approaching rows, to a series of correlated impacts such that the collision is characterized by the gentle interaction of the ion with many atoms, rather than a high angle scattering event with any single atom. That being the case, the row of atoms can be thought of, to a good approximation, as a line of charge of the same, smeared linear density. This approximation, referred to as the continuum approximation, was introduced by Lindhard [Lind65]. In such treatments, it is convenient (and conventional) to separate the motion into two components, which leads to the definition of the transverse energy,

$$E_{\perp} = E \varphi^2 + U(r), \quad (5-1)$$

for a particle traveling at a position r (string at $|r|=0$), moving at an angle φ with respect to a string, and having potential energy $U(r)$ (see figure 5-1). As the ion is channeled, this quantity is, to first order, conserved.

The continuum approximation is, of course, only valid as long as the graininess of the potential is not felt by the ion beam. This condition was expressed by Lindhard as,

$$U''(r_{\min})d^2 / 8E < 1, \quad (5-2)$$

which leads, using Lindhard's potential for the strings [Lind65], to a restriction on the distance of closest approach (r_{\min}) for which the continuum approximation is valid,

$$r_{\min} > (2dZ_1Z_2e^2 / 8E)^{1/2}. \quad (5-3)$$

Here, d is the atomic separation on the strings (5.43 Å for the $\langle 100 \rangle$ axis of Si). For our channeled beam experiments (2.5 MeV He^+), the right hand side of equation 5-3 equation is equal to 0.02 Å. At first glance, this seems to exclude substitutional sites. However the crystal atoms have a mean displacement [Gemm74] from their equilibrium (string) positions (ρ) due to thermal vibrations of $\rho_{\text{Si}} \approx 0.1$ Å (room

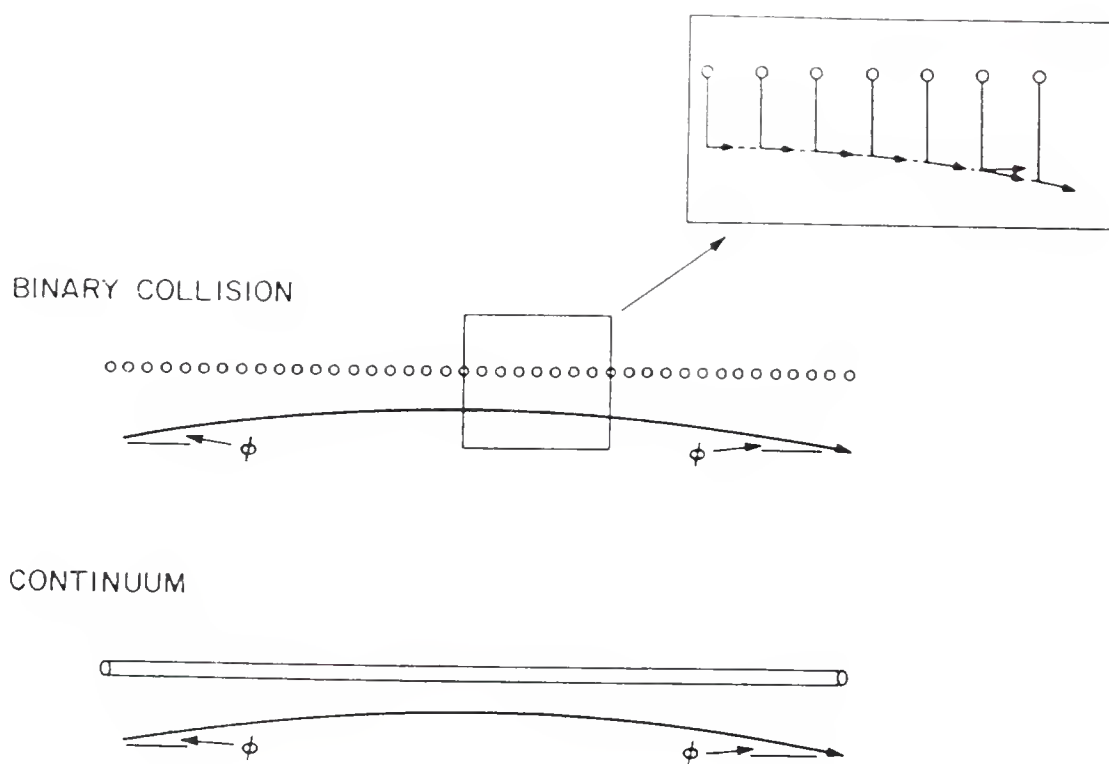


Figure 5-1. Sketch of an ion interacting with a string (row of atoms). The effective charge of ions He ions in Si at these energies ($\sim 2\text{MeV}$) is +1.94. Due to the gentle nature of the interaction (inset), the atom row can be approximated by a line of charge (from Feldman [Fe88, p.39]).

temperature). This insures that, under these conditions, the continuum approximation is valid for use in the calculation of scattering yields for all impurity positions in (or on) the crystal.

Statistical equilibrium. The assumption of statistical equilibrium for channeling processes relies on the two-dimensional nature of the space within which the particles are confined, and was first made by Lindhard. He pointed out in reference to this system, [Lind65] that the spatial distribution function, $F(E_{\perp}, \mathbf{r})$, for a system conserving energy, is proportional to the an integral over the momentum part of the phase space,

$$\int \delta(E - E_{\perp}) d\mathbf{p}, \quad (5-4)$$

in the microcanonical ensemble (E is conserved), with

$$d\mathbf{p} = 2\pi p_{\perp} dp_{\perp} = 2\pi M dE_{\perp}. \quad (5-5)$$

The integral in equation 5-4 is then constant, implying that the probability density for particles of given E_{\perp} is uniform within the area that their E_{\perp} allows them to access. If the accessible area is termed $A(E_{\perp})$, then the distribution function becomes,

$$F(E_{\perp}, \mathbf{r}) = \begin{cases} 1/A(E_{\perp}) & E_{\perp} \geq U(\mathbf{r}) \\ 0 & E_{\perp} \leq U(\mathbf{r}). \end{cases} \quad (5-6)$$

A given channeled particle is confined therefore to move within the area defined by the value of its transverse energy and the electrostatic potential in the channel. This concept is illustrated in figure 5-2, where several trajectories are shown for 2.0 MeV He^+ ions in a $\langle 100 \rangle$ channel. These trajectories were calculated within the 25-string Doyle-Turner continuum potential [Doyl68] (equation 5-7, below). The trajectories shown are for ions entering the channel at various positions (indicated by the arrows) and aligned with the axial direction. The accessible areas, which are defined by the

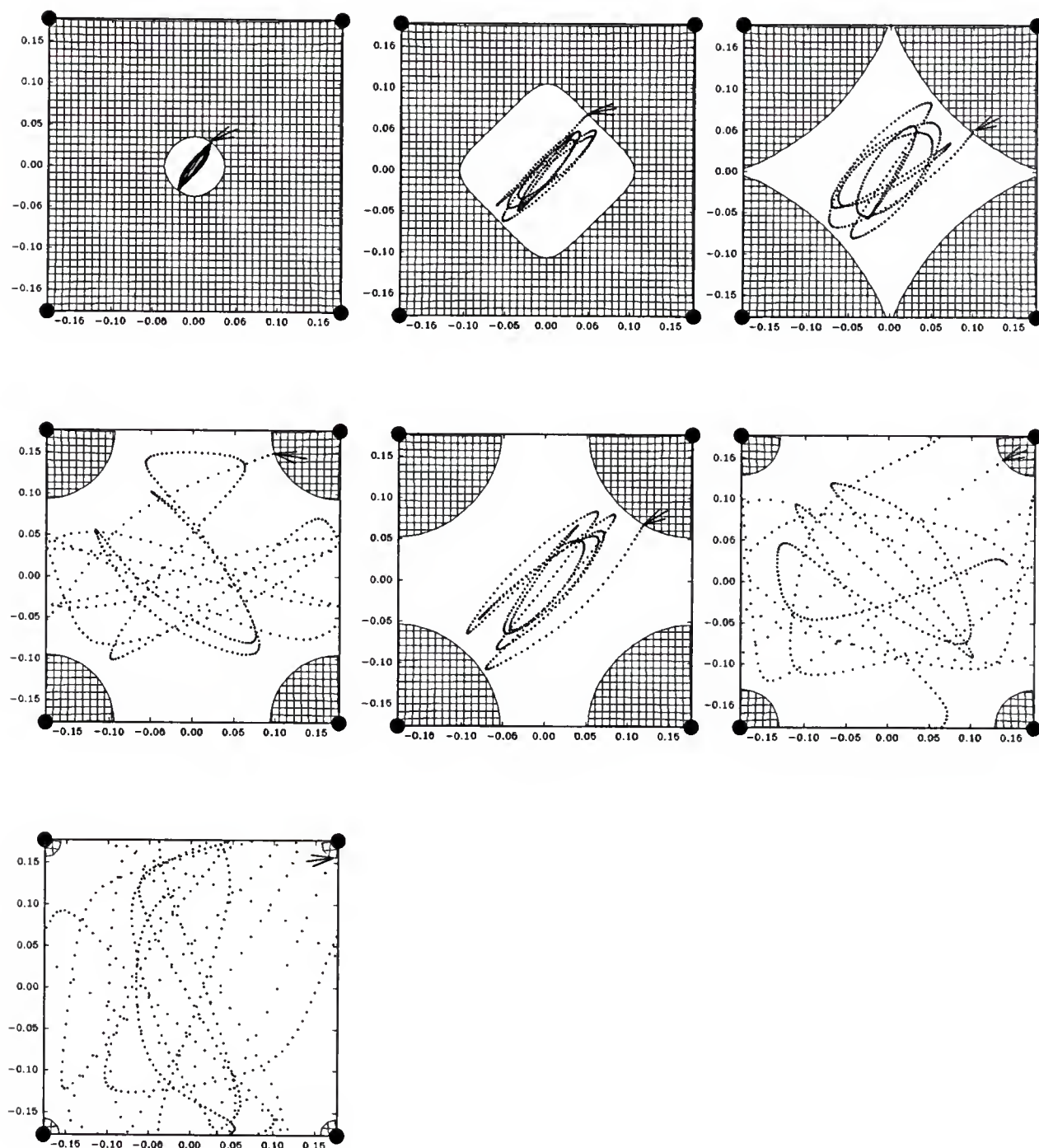


Figure 5-2. Ion trajectories projected on the $\langle 100 \rangle$ plane. The trajectories shown (dots) were calculated for a 2.0 MeV He ion moving in a continuum potential for a pathlength (into the page) of 5000 Å. Every 10 Å the forces on the ion were calculated and its trajectory adjusted. The arrows indicate the position of entry of the ion into the channel. Hatched regions indicate inaccessible areas.

magnitude of E_{\perp} (equation 5-1, $\psi = 0$), are shown for each case as the unhatched regions in which the particles travel.

There are several problems with the statistical equilibrium hypothesis, which need to be addressed. The first concerns the ion distribution at shallow depths in the crystal ($< 1000 \text{ \AA}$). It is clear that just after entering the crystal, the beam does not satisfy the requirements of statistical equilibrium, because particles oscillate between the "walls" of their confining potential barrier. This behavior will be manifested by oscillations in the scattering yield from the substrate atoms as a function of depth which show a characteristic dampening at positions deeper in the sample due to the lack of coherence among the individual ion trajectories. This effect has been well documented [Barr71, Abel75]. The fact that the oscillations die at thicknesses above $\sim 2000 \text{ \AA}$ [Barr71, Abel75], supports the assumption of statistical equilibrium as the beam exits the crystal for our samples, which are much thicker ($\sim 5000 \text{ \AA}$).

Another concern is related to the influence of crystallographic planes on the shapes of angular scans. If an ion is incident at a tilt angle such that its momentum vector p_{\perp} is in a direction which coincides approximately with that of a major plane of the crystal, the motion of the particle will be governed by the plane (planar channeling), and statistical equilibrium will not be realized. The effects of planar channeling can be minimized with careful attention to the direction chosen for the angular scan. For our current experimental setup, this problem has been dealt with, as discussed in chapter 3, by avoiding major planes while tilting about the axial direction. Also, angular scans that are grossly misshapen and/or are without the appropriate shoulder level are not accepted. As an example, figure 5-3 shows several angular scans across the $<100>$ axial channeling direction. The solid circles represent the normalized yield from a scan conducted in a random plane. Note the symmetry of the scan and the correct level at larger tilt angles. Also shown are two unacceptable

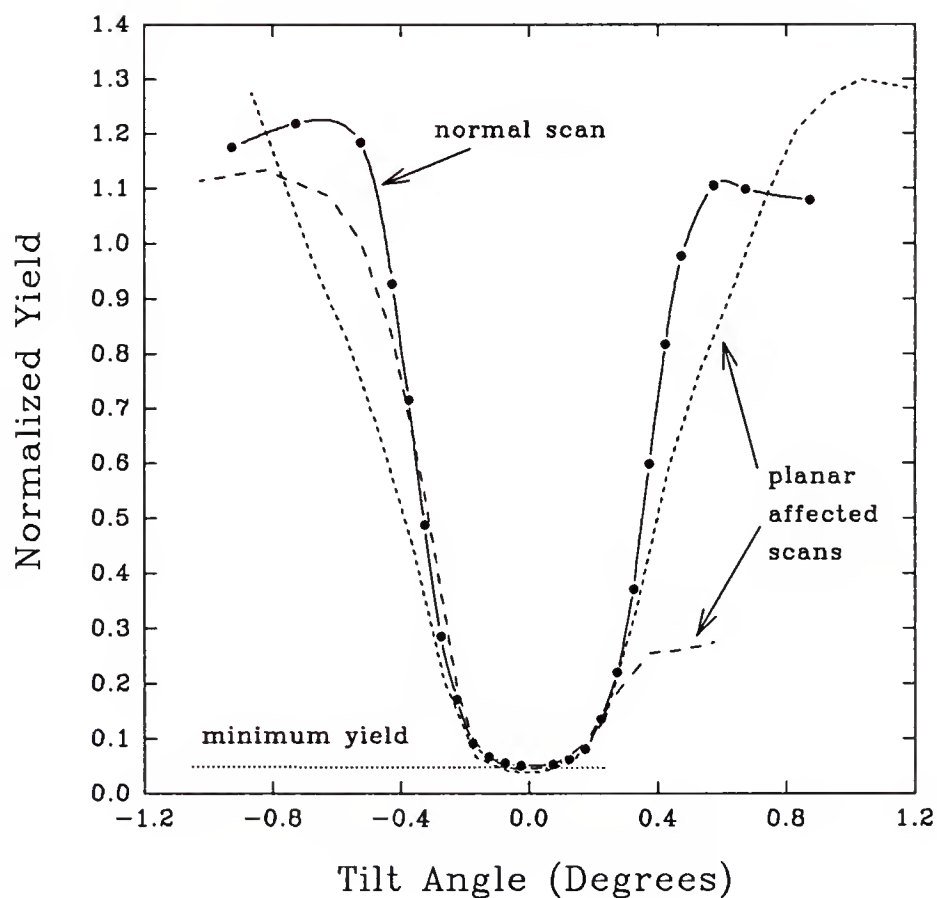


Figure 5-3. Angular scans across the $\langle 100 \rangle$ axis of Si. The angular scan represented by the filled circles has the expected shape and shoulders for a scan in a random plane. The scans represented by the dashed curves are affected by planar channeling and are unacceptable.

angular scans. For these scans, the yield from the overlayer being studied might be effected in a similar manner, and could yield inaccurate results. For this reason, no conclusions were drawn from scans showing large and obvious deviation from normal. This discrimination, in principle, should be sufficient. In practice, the situation is even better. We have observed that, even when the host angular scan has been affected by planar channeling, the surface impurity scans are reproducibly *unaffected* [Lyma91a]. Presumably, this is a benefit of the thickness of our windows. Over the ~ 5000 Å pathlength the ions travel to reach the exit surface, the planar effects are likely washed out. Therefore, as long as scans are used which are not drastically affected by planar channeling, the assumption of statistical equilibrium should be valid in this respect.

A final concern with calculations based on the continuum approximation was studied by Barrett [Barr71, Barr76]. He found that these calculations underestimate the yield in the channeling direction due to crystal focusing effects and, also, due to a low energy tail on the transverse energy distribution function. Both of these effects are not accounted for with the assumption of statistical equilibrium. These omissions, for substitutional impurities when the beam is aligned in the channeling direction, can lead to errors in the calculated yield of a factor of 2 to 3. However, for this worst case, the error with respect to the random yield is only $\sim 2\%$. For the sites displaced from substitutional, the effect is diminished, since the cause, for both, is a small component of the beam with high transverse energy. The contribution to the yield from well-channeled particles increases rapidly as the impurity is displaced from substitutional, so the high- E_{\perp} component has a very small influence on the yield for displaced impurities. Therefore, the assumption of statistical equilibrium is expected to introduce a negligible error for the calculation of yields for sites displaced (even slightly) from substitutional, and a small error for exactly-substitutional sites.

Execution

With the assumptions of the model in place, the calculation of the scattering yield as a function of angle is rather straightforward. The basic idea is to calculate the potential (from lines of charge) in the channel. From this, and with the definition of transverse energy, the flux distribution can be found. The scattering yield is then the overlap of the flux distribution with the impurity location (distributed as a Gaussian in the channel).

Figure 5-4 displays the potential within each channel calculated within the continuum model. The potential used is the thermally-averaged 25 string Doyle-Turner potential, given by,

$$U(r) = \{ (8\pi^2 a_0 e^2 Z_1) / d \} \sum_{i=1,4} \{ a_i / (b_i + (2\pi\rho)^2) \} \exp \{ -(2\pi r)^2 / (b_i + (2\pi\rho)^2) \}. \quad (5-7)$$

Here a_0 is the Bohr radius, and a_i and b_i are the Doyle-Turner coefficients which describe 4 Gaussians used to fit atomic potentials. These potentials were calculated by taking the Fourier transform of electronic scattering factors determined with a relativistic Hartree-Fock method [Doyl68]. Equation 5-7 then represents the continuum potential derived from those atomic potentials. Note the presence of ρ , the two-dimensional RMS thermal vibrational amplitude of the crystal atoms, in the potential, which arises due to thermal averaging.

It is this potential in the channel that dictates the accessible areas for ions with a given E_{\perp} , allowing a calculation of the ion flux distribution. For random incidence, the flux distribution is uniform, and with total area of the channel being denoted A_0 , is equal to $1/A_0$. Then the probability of a close encounter between ion and impurity (Π_{in}), normalized to that for random incidence, is given by,

$$\Pi_{in}(E_{\perp}) = A_0 \int F_a(E_{\perp}, r) P_i(r) dr. \quad (5-8)$$

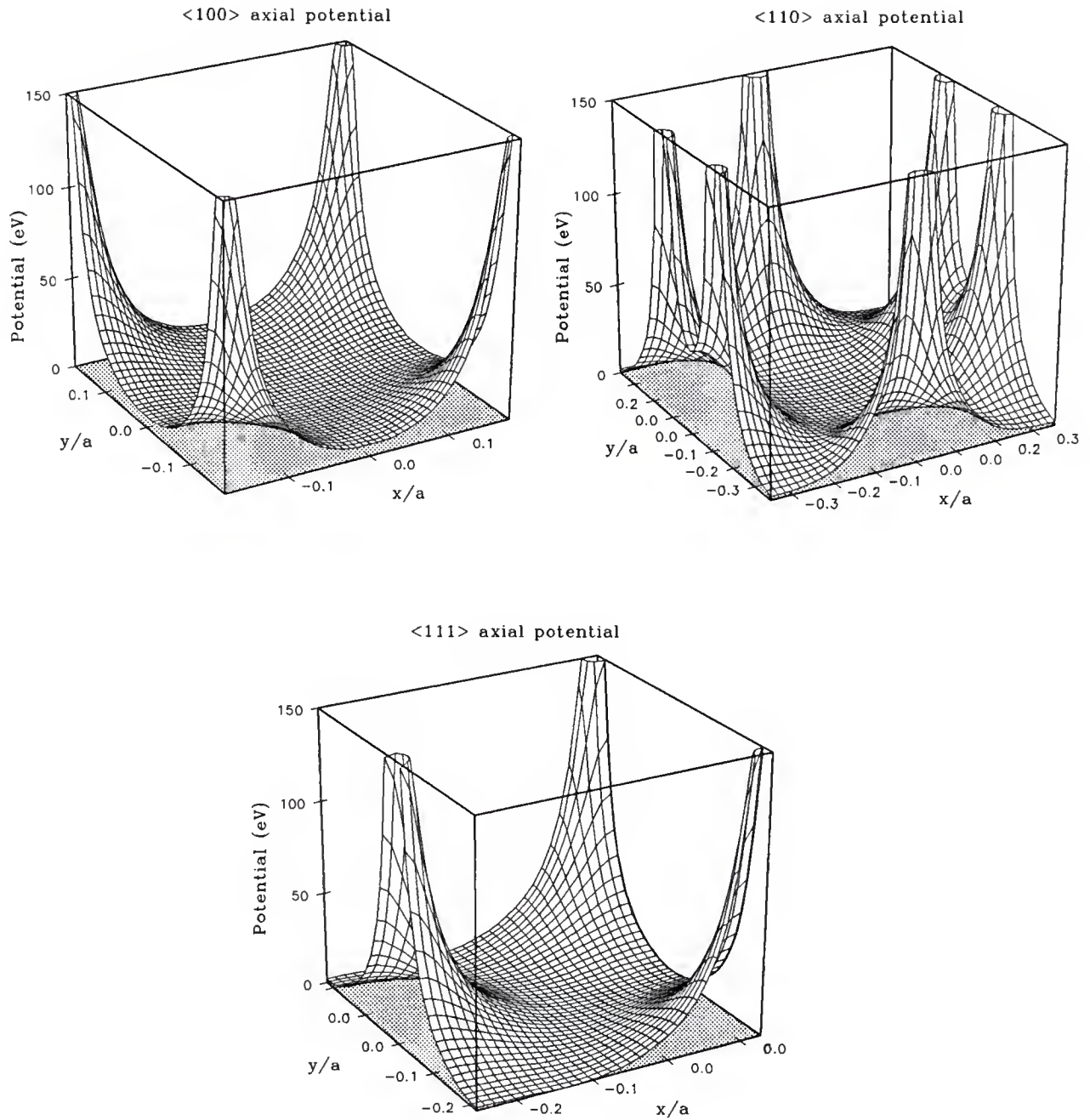


Figure 5-4. Electrostatic potentials calculated in the <100>, <110> and <111> axial directions of Si with a thermally-averaged Doyle-Turner potential. Units are fraction of a lattice constant.

Here F_a is as defined above (equation 5-6), and P_i is the Gaussian distribution of the impurity on the surface,

$$P_i(\mathbf{r}) = 1/(\pi\rho^2) \exp\{-(|\mathbf{r}-\mathbf{r}_i|/\rho)^2\}, \quad (5-9)$$

while, ρ is the two-dimensional RMS thermal vibration amplitude of the impurity. Other distribution functions for the impurity are possible. This matter of choice and considerations involving the magnitude of ρ are discussed in chapter 9. Equation 5-8 gives the basis for the calculation of scattering yields for channeled beams.

Up to now the discussion has assumed that transverse energy is conserved. In practice, however, interactions (multiple scattering) with electrons and interactions with the thermally vibrating strings lead to gradual changes in the transverse energy distribution of the ions as the beam penetrates deeper into the crystal. Those changes have the effect of smearing the flux distribution with depth, and lead to changes in the scattering yield. This problem of dechanneling was studied by Bonderup *et al.* Their theoretical treatment [Bond72], to which the reader is referred for details, serves as the basis for the inclusion of dechanneling in this calculation. The general treatment relies on the solution of the diffusion equation, which is written,

$$\partial g(E_{\perp}, z)/\partial z = \partial/\partial E_{\perp} \{D(E_{\perp})\} \partial/\partial E_{\perp} \{g(E_{\perp}, z)\}. \quad (5-10)$$

The quantity $D(E_{\perp})$, can be thought of as a position dependent diffusion coefficient, and $g(E_{\perp}, z)$ is the transverse energy distribution function (z is thickness). The solution of this equation, and the treatments for the electronic and nuclear contributions to the dechanneling are discussed in the references [Bond72; Bech88a], and at length in the PhD. thesis of B. Bech Nielsen [Bech88b]. Shown in figure 5-5 is a channeling spectrum for 2.0 MeV He^+ incident on Si along the $\langle 100 \rangle$ axis (dots). For this spectrum, the horizontal axis is displayed as depth into the crystal, and the rise in yield due to the increasing cross section with depth (energy) has been extracted, so the

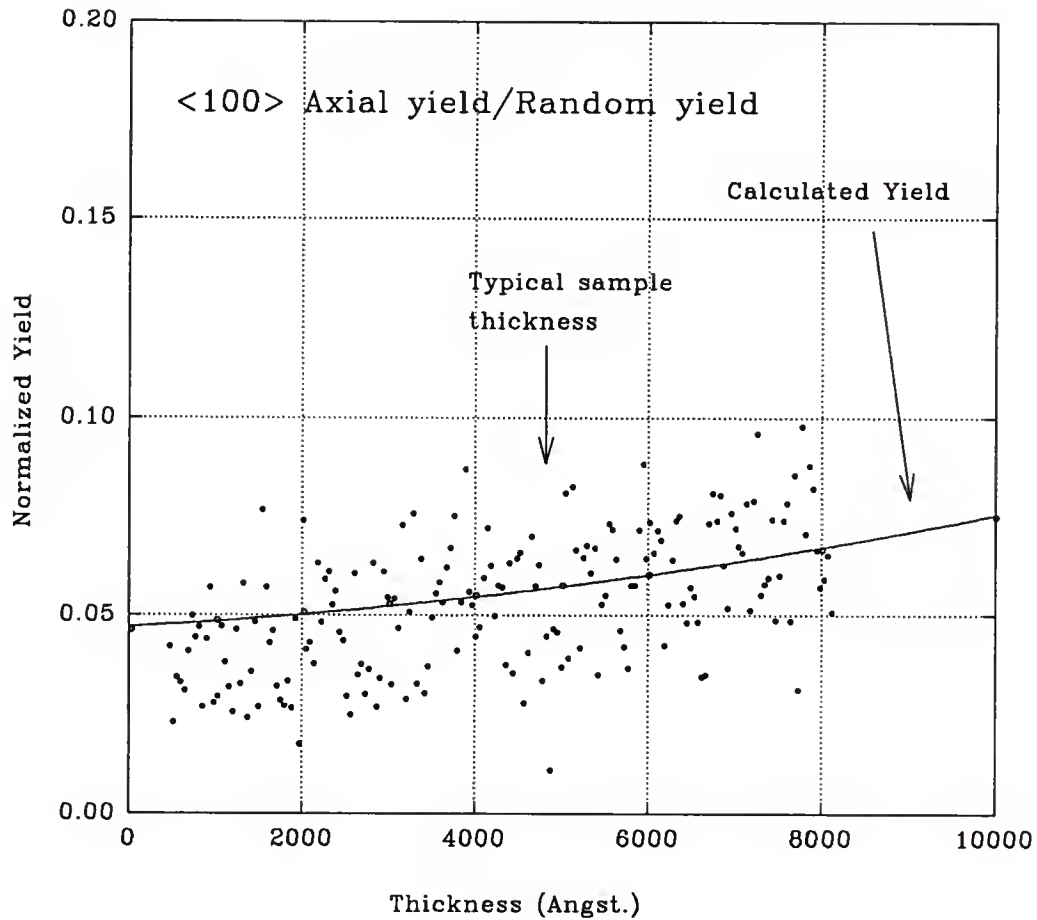


Figure 5-5. Minimum yield with depth into a Si sample aligned with the <100> axis. Shown is a channeling spectrum divided by a random spectrum (dots). This roughly eliminates the increase in yield due to the dependence of the cross section on energy ($1/E^2$). Also shown is the increase in yield with thickness due to dechanneling predicted by the channeling calculation.

increasing yield is solely from an increasing dechanneled component of the ion beam. Also shown is the scattering yield as a function of depth predicted by the calculation (solid curve). Here, the contribution to dechanneling from electrons [Bech88b] has been calculated assuming a uniform electron density equal to that given by distributing the 4 valence electrons per Si atom evenly in the crystal. The nuclear contribution [Bech88b] is from Si atoms vibrating with a vibrational Si amplitude of $\rho_{\text{Si}}=0.14 \text{ \AA}$. It is clear that the agreement at depths which correspond to the thickness of a typical window is much better for the calculation including dechanneling, without which, the predicted yield would show no increase. With the transverse energy distribution function, the equation used to calculate the scattering yield for a given beam-tilt becomes,

$$\chi(E, \psi, z) = \int_0^{\infty} g(E_{\perp}, z) \Pi_{\text{in}}(E_{\perp}) dE_{\perp}. \quad (5-11)$$

Then, by inputting the (experimentally determined) thickness of the crystal, the beam energy, and taking a range of tilts, the calculated angular scans are generated for a given impurity site. Figure 5-6 shows the calculated scattering yield as a function of position across three low-index channels in Si for a channeled beam ($\psi=0$) of 2.5 MeV He^+ ions. The thickness of the crystal was 5000 \AA , and the vibrational amplitude of the impurity was taken as 0.2 \AA . The yield was calculated over this grid by X_MINN.FOR using equation 5-11. This figure illustrates well that the scattering yield is very sensitive to the positions of impurities on the surface.

Crystallographic Projections

Required as input for the calculation of the angular scans are the predicted positions of the impurities of interest in the given axial channel. Our studies were conducted on Si crystals in the $\langle 100 \rangle$ orientation. However, data have been acquired across three axial channeling directions: the $\langle 100 \rangle$, $\langle 110 \rangle$ and $\langle 111 \rangle$. In each of

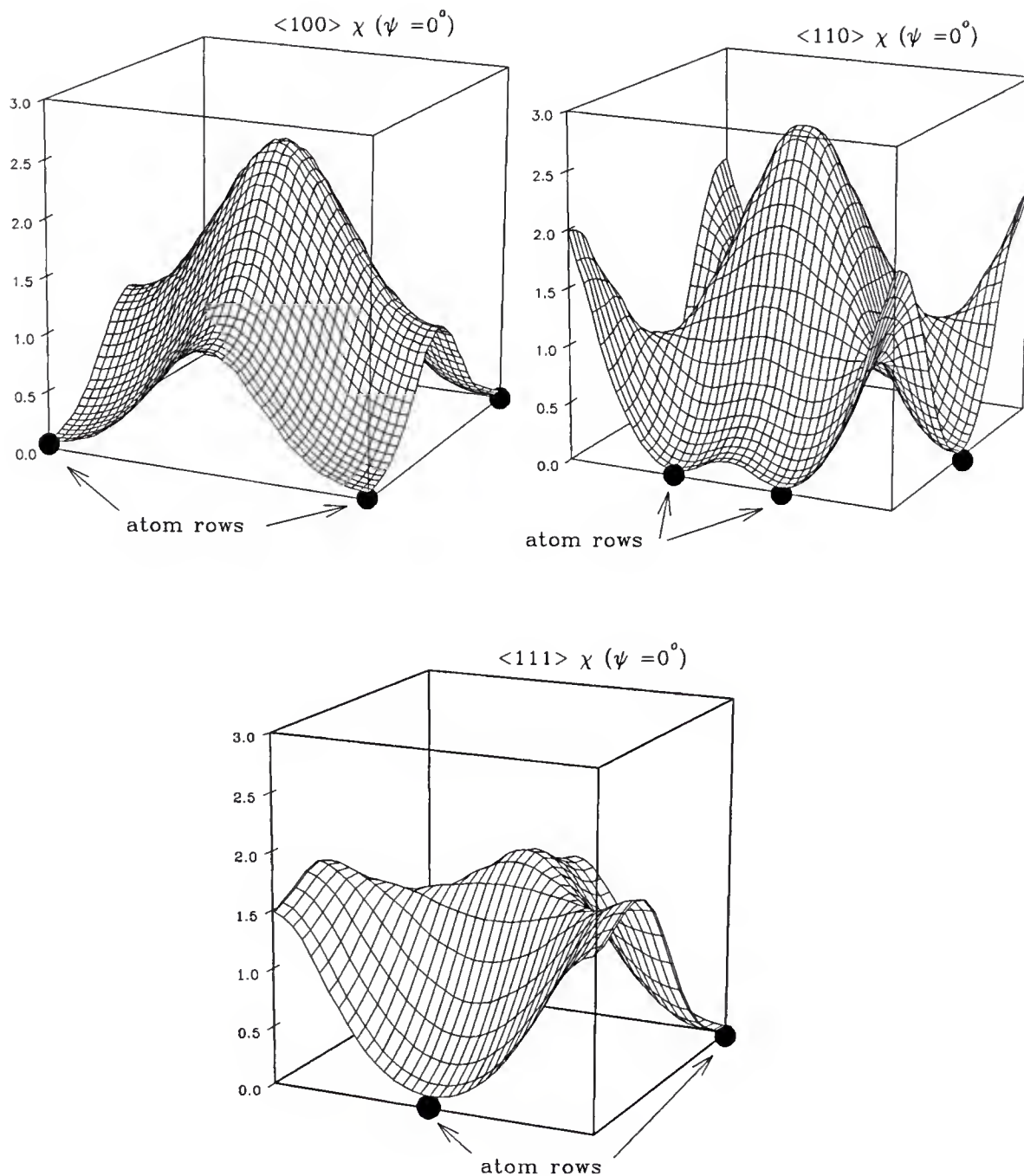


Figure 5-6. Scattering yield across the $\langle 100 \rangle$, $\langle 110 \rangle$, and $\langle 111 \rangle$ axial channels for 2.0 MeV He ions channeled in Si ($z = 5000 \text{ \AA}$). The figures represent the scattering yield for an impurity having $\rho = 0.2 \text{ \AA}$ at all positions across the channels. These reproduce the (slightly smeared) flux distributions. The filled circles represent the atom rows defining the channels.

these cases, the scattering yield from a given adatom site is dictated by the position of the site projected onto the plane perpendicular to the axial direction. For the $\langle 100 \rangle$ direction (perpendicular to the surface), the adatom site coordinates give the position in the channel. For the off-normal directions ($\langle 110 \rangle$ and $\langle 111 \rangle$), however, these positions must be calculated from the adatom coordinates on the surface. Another consideration concerns the steps on the surface (typical step densities are ~ 20 steps/micron [Mo90]). Steps on the Si(100) surface separate local crystallographic domains which appear rotated by 90° [Mo89, Hame86], as is illustrated in figure 5-7. Here, an STM image [Hame86] of the Si(100) surface is shown. The dimer rows are visible as the lines running across each terrace, and the elongated bumps making up the dimer rows are interpreted as representing the individual dimers. Only upon descending four steps is a position in the crystal equivalent to the original obtained. This being the case, projections from the $\langle 100 \rangle$ adatom surface site must be considered from each of the possible steps. Because a typical beam spot encompasses tens of thousands of steps, for nominally flat surfaces, one would expect an equal contribution from each step. Therefore, each site on the surface yields, in the $\langle 110 \rangle$ and $\langle 111 \rangle$ directions, 4 projected sites. Depending on the surface site, some projected sites will be redundant. However, all are considered such that the yield at a given ψ is given by,

$$Y(\psi) = \sum_{i=1,N} (w_i y_i) / W \quad , \quad (5-12)$$

where,

$$W = \sum_{i=1,N} w_i. \quad (5-13)$$

Here the w_i are the weights of the individual sites. Figure 5-8 shows projected positions for an adatom in a dimer-like site for the three axial directions generated via a screen dump with the program PROJECT.FOR [Gran92a]. Depicted are the

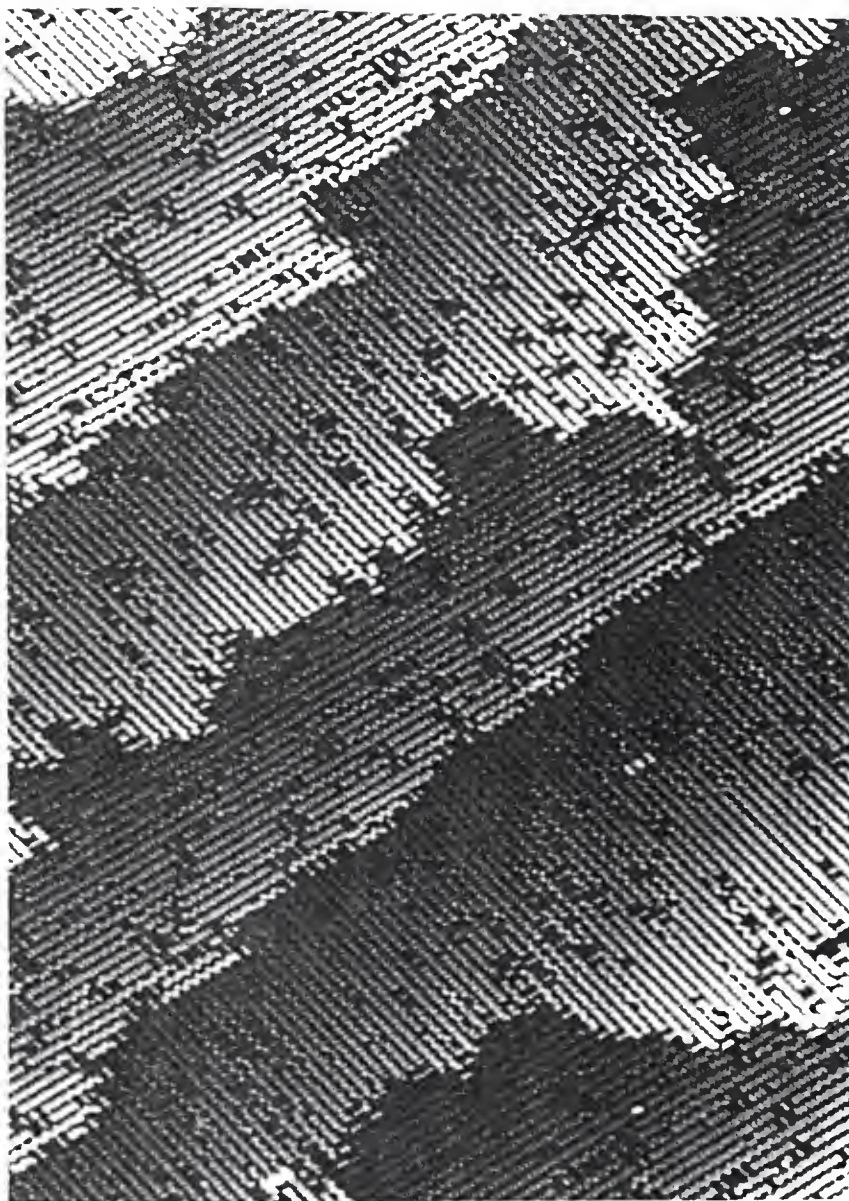


Figure 5-7. STM images of a clean Si(100) surface (from Hamers [Hame86]). Five steps are clearly visible. Dimer strings, appearing as lines on the terraces, are either parallel or perpendicular to the step edges.

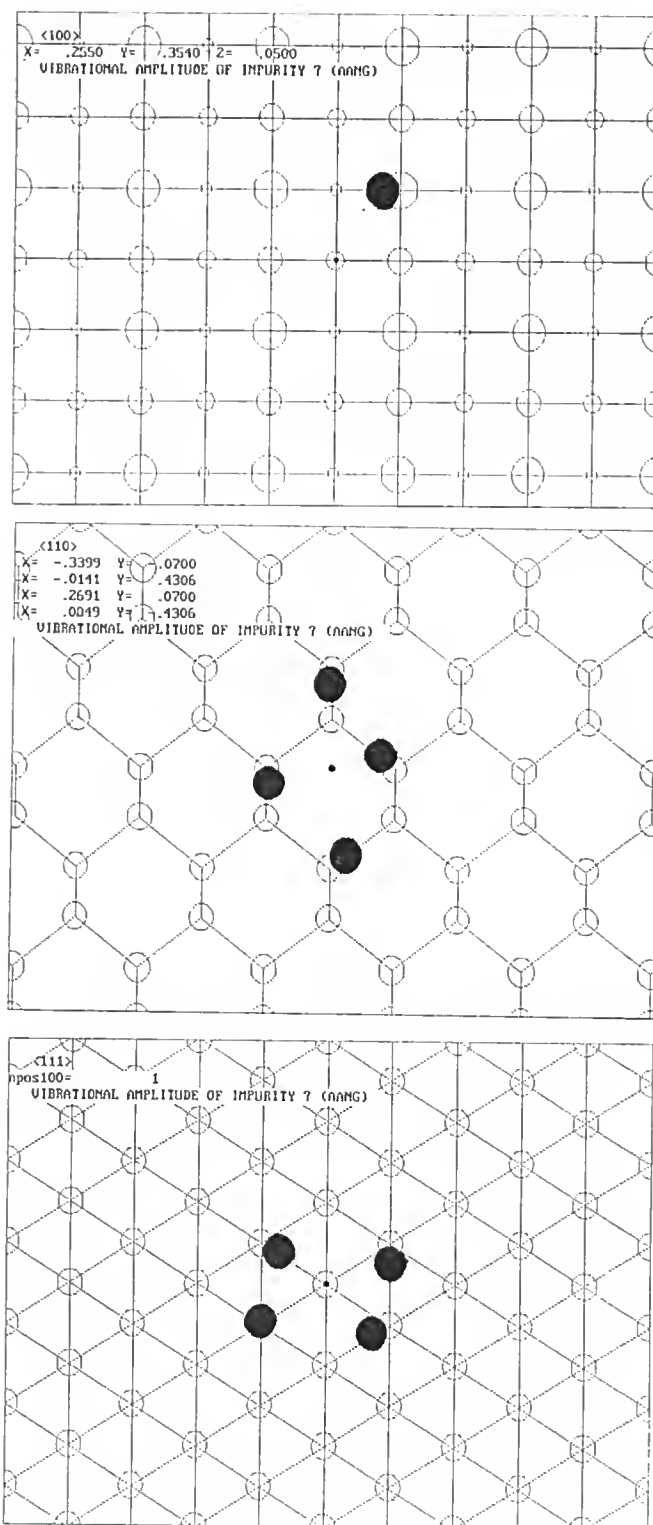


Figure 5-8. Projected adatom positions in three axial channels. These plots were generated via screen dumps from the FORTRAN program PROJECT.FOR. Shown are projections into the $\langle 100 \rangle$, $\langle 110 \rangle$ and $\langle 111 \rangle$ channels for a dimer site (only one dimer atom is projected).

adatom sites (filled circles) on a grid of crystal sites (open circles) defining the channels. The small closed circle on each represents the origin defined for that direction. In PROJECT.FOR, the adatoms sites are projected by defining coordinates on the <100> surface and calculating the positions of the point in the off-normal directions. For the present case, all the sites shown would then be weighted equally.

The equations governing the transformations were found readily using three-dimensional rotational matrices. For these, x_{100} , y_{100} , and z_{100} are the coordinates of the site of interest on the surface. Then, if x_{110} , y_{110} and x_{111} , y_{111} are the coordinates of the projected points, these are given by [Corb50, p 140]:

$$\begin{pmatrix} x_{11?} \\ y_{11?} \\ z_{11?} \end{pmatrix} = \begin{pmatrix} \cos\psi \cos\varphi - \sin\psi \cos\theta \sin\varphi & \cos\psi \sin\varphi + \sin\psi \cos\theta \cos\varphi & \sin\psi \sin\theta \\ -\sin\psi \cos\varphi - \cos\psi \cos\theta \sin\varphi & -\sin\psi \sin\varphi + \cos\psi \cos\theta \cos\varphi & \cos\psi \sin\theta \\ \sin\theta \sin\varphi & -\sin\theta \cos\varphi & \cos\theta \end{pmatrix} \begin{pmatrix} x_{100} \\ y_{100} \\ z_{100} \end{pmatrix}$$

The coordinate systems are defined in figure 5-8, and φ , θ and ψ are the Euler angles. As an example, table 5-1 gives values for the angles for rotation into the <110> direction, and the corresponding x and y coordinates in that plane.

Table 5-1. Coordinate transformation for <110> axial direction*.

#	φ^\dagger	θ^\dagger	ψ^\dagger	x_{110}	y_{110}
1	45	-45	90	$\frac{1}{2}(x+y)-z/(2)^{1/2}$	$(y-x)/(2)^{1/2}$
2	-45	-45	-90	$\frac{1}{2}(y-x)+z/(2)^{1/2}$	$-(x+y)/(2)^{1/2}$
3	135	-45	-90	$\frac{1}{2}(x-y)+z/(2)^{1/2}$	$(x+y)/(2)^{1/2}$
4	-135	-45	90	$-\frac{1}{2}(x+y)-z/(2)^{1/2}$	$(x-y)/(2)^{1/2}$

\dagger Angles in degrees.

* x, y and z are on the surface, i.e., x_{100} , y_{100} and z_{100} .

CHAPTER 6 DATA REDUCTION

Experimental Angular Scan Extraction

In ion scattering, the data come in the form of energy spectra (see figures 3-1 and 3-3). Each spectrum contains a wealth of information about the sample and distribution in energy of the scattered ions. For site determinations, however, it is convenient to have the data in the form of angular scans. In order to display the data in this manner, the scattering yield for a given region in energy at each tilt angle must be extracted from each spectrum. For analysis of an overlayer, this involves determining the integrated sum of counts in the impurity peak of interest. As an example, figure 6-1.a shows spectra in the aligned and random geometry for an Sb/Si(100) sample. For data such as these, the extraction is rather straightforward. One simply has to subtract the approximately linear background from the counts in the region of the spectrum containing the peak. In practice, the process is slightly complicated by the fact that the trajectory dependence of the energy loss of ions traveling in the crystal causes channeled particles to lose less energy than particles traveling in a random direction through the crystal [Appl67; Mae73; Jin86; Dygo88]. As a consequence, the Sb peak moves on the energy axis when the beam is changed from random to channeled incidence. This shift is seen clearly in figure 6-1.b, which shows an expanded view of part of the Sb/Si(100) spectra. However, if one chooses the region to be summed as the foreground such that this entire range is included (the peak region), and chooses the regions by which to determine the background to flank the peak region, an accurate sum can be extracted easily, assuming linear background. A typical choice of windows for this method of data extraction is indicated on figure 6-1.b.

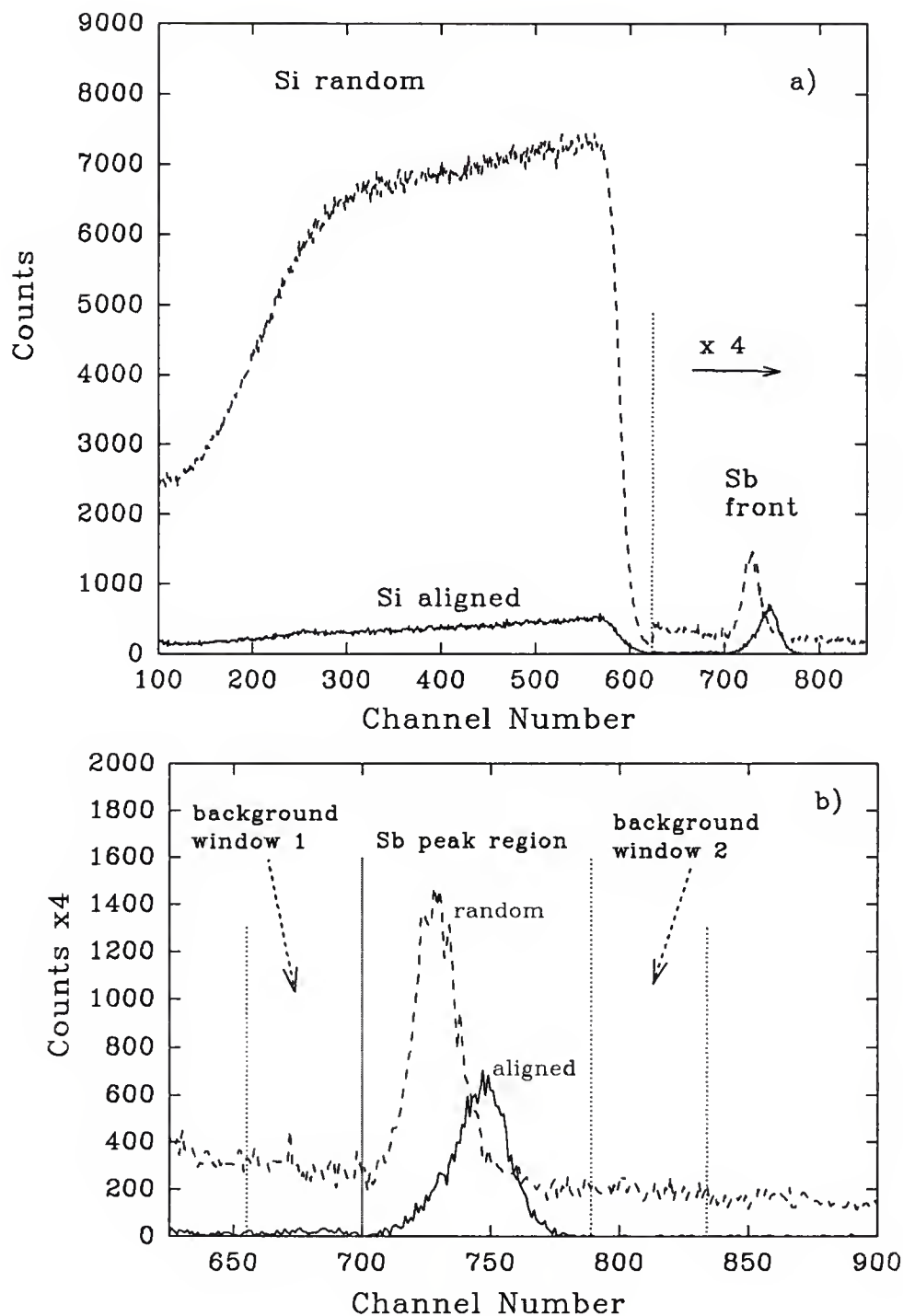


Figure 6-1. Channeling and random spectra ($\langle 100 \rangle$ axis) from an Sb/Si(100) sample. Dashed curves are for random incidence. Solid curves are for aligned incidence. a) Expanded view; b) Region of spectra showing Sb peaks. Indicated are the windows chosen for background subtraction. The total number of channels in the two background windows is equal to the number in the peak window.

Another method of data extraction involves fitting. While fitting is not necessary for spectra such as that in figure 6-1, this method generally lends itself more easily to automation, and it becomes necessary when peaks from two or more elements are closely located in energy. This technique is especially preferred (and necessary) when the peaks overlap. Another concern is that, in general, the lineshapes of peaks from ML films are Gaussian only for random beam incidence. For channeled beams, the shapes are complicated [Dygo94]. These difficulties are illustrated in figure 6-2, where an expanded region of aligned and random incidence spectra from a sample having on it Ge (0.8 ML) and Sb (1 ML) is shown. The data are represented by dots. Also shown, as the solid curves, are fits to the data used to extract peak sums. In order to circumvent the problems involving peak shifts and non-Gaussian peaks, numerous Gaussians are fit to each peak. The curves shown represent the sum of 10 Gaussians (5 each for the Ge and Sb peaks) and a line.

For the fitting procedure, the widths of all Gaussians were fixed at a value determined from a separate fit (of one Gaussian per peak) to a random-incidence spectrum, and the positions of the Gaussians were fixed at values determined as follows. The positions of the Gaussians at the extremes of high and low energy for each element were determined from channeling spectra and shoulder spectra respectively. This determination proved simple for the Sb peak, which was well defined for both cases. However, for the Ge peak, which was not well defined in the channeling direction, the logical assumption was made that the peak shifted, at a maximum, as much as the Sb peak shifted (i.e., the spacing between the extreme Ge peaks was set equal to that of the Sb peaks). Then, the remaining 3 Gaussians for each peak were spaced evenly between these. For determining the low energy bound, the shoulder spectra were used rather than the random ones, since particles traveling preferentially near the rows of atoms (as is the case for shoulder data) have, on

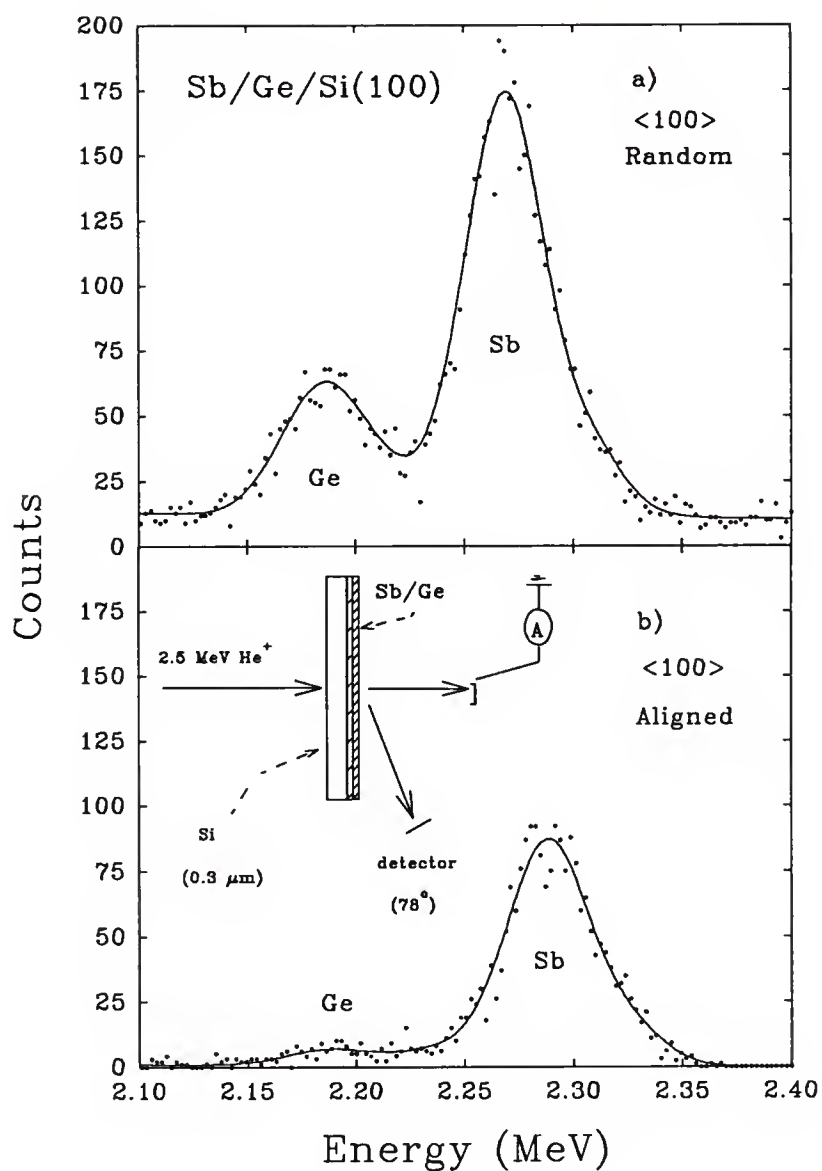


Figure 6-2. Portion of spectra for Sb/Ge/Si sample. Shown are the data (dots) and the fitted curve used to extract the peak sums. a) Random spectrum; b) Aligned spectrum. In the inset is the scattering geometry.

average, a slightly higher energy loss than those with random incidence. The heights of the Gaussians then were varied, along with the slope and intercept of the line for the background.

A FORTRAN program has been written in order to facilitate the fitting process. It displays the fits and data graphically for evaluation and allows for the automatic fitting of multiple spectra. This program, DATAFIT.FOR [Gran93a], uses a Levenberg-Marquardt method, which constitutes a combination of the inverse-Hessian and steepest descent methods, and has become common for nonlinear least-squares fitting [Pres92]. In practice, coefficients for the Gaussians are passed to a subroutine MRQMIN.FOR [Pres92], along with a list of coefficients to be adjusted (parameters) after compilation in DATAFIT.FOR. The parameters are adjusted until the value of chi-squared does not change appreciably for several iterations, after which the fit is assumed converged, and the data and fitted curve are printed to the computer terminal for visual evaluation. Represented in figure 6-3 is the fit, as viewed on the screen, of a spectrum obtained by summing all spectra from a <100> angular scan. The figure shows the data (dots), the sum of the ten Gaussians and a line (upper curve), and the individual Gaussians (lower solid curves). Note that, due to the energy shift with tilt angle, the widths of the Ge and Sb peaks are greater than those obtained at random-incidence (shown in figure 6-3, and equal in width to the individual Gaussians, lower curves). Factors which contribute to the width of random-incidence peaks were discussed in chapter 4 in relation to the Ge thin windows. The widths of aligned-incidence peaks are influenced by trajectory-dependent energy loss considerations.

It has been found that the fitting procedure just described is robust to small changes in the width of the Gaussians, or even the total number of Gaussians. However, in order to minimize errors resulting from the fitting, the data were

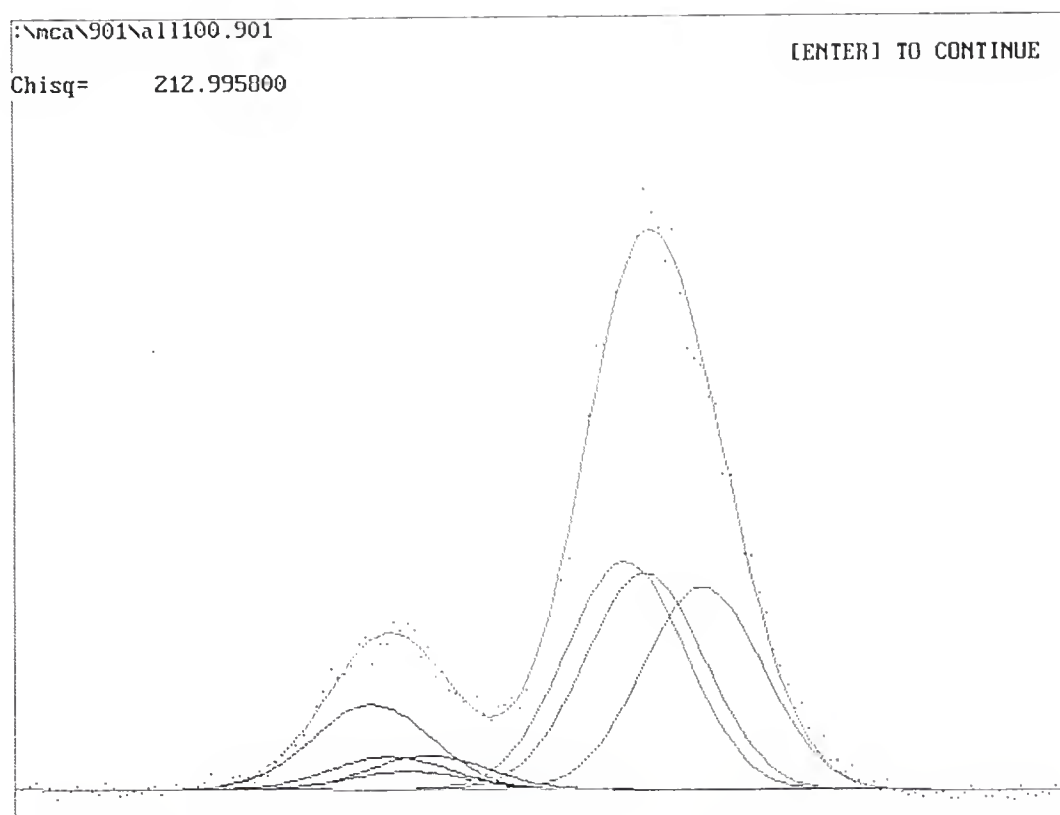


Figure 6-3. Screen dump from DATAFIT.FOR.

extracted with as little reliance on accurate representations of the lineshapes as possible. This was done, for the case of Sb/Ge/Si, by subtracting the *experimental* counts from the fitted background line, in order to arrive at the peak areas, rather than integrating the fitted Gaussians to obtain these areas. This necessarily means that one has to determine which counts belong in which peaks, a task which proves simple except in the region of overlap. In that region, the fit for the largest and most well-defined peak, the Sb peak, was integrated, and the integrated value was added to the total Sb counts outside the region of overlap. The rest of the counts in the interface region then were added to the Ge counts. As a check, the BS detector (150°) provides a signal which has Ge and Sb well separated in energy. While the Ge signal suffers from being in a region of high background (this is one reason the 78° detector is used instead), the Sb gives a strong, clean signal. The Sb data therefore are easily extracted by setting windows on the BS spectra, as described above. With this procedure, the Sb angular scans obtained from the fitting technique described above can be compared to those obtained directly from the BS detector. Figure 6-4 shows a normalized $\langle 110 \rangle$ Sb angular scan obtained by fitting the Sb/Ge/Si(100) data from the 78° detector (solid circles) along with the normalized scan from the BS detector, taken simultaneously. These two show good agreement, suggesting further that the fitting procedure is accurate. This figure also illustrates the difference in the sizes of the experimental uncertainties from the two detectors, and hence shows another advantage of the transmission geometry.

In the studies presented here, both methods of data extraction have been used. For the Sb/Si(100) investigations (chapter 8), the peak sums for the Sb were extracted by setting windows and using a FORTRAN program, CUT.FOR [Lyman90]. For the Sb/Ge/Si and Ge/Si studies, peak sums for the Ge and Sb were extracted by fitting the data with DATAFIT.FOR. For the Ge/Si data (and other test cases), sums were

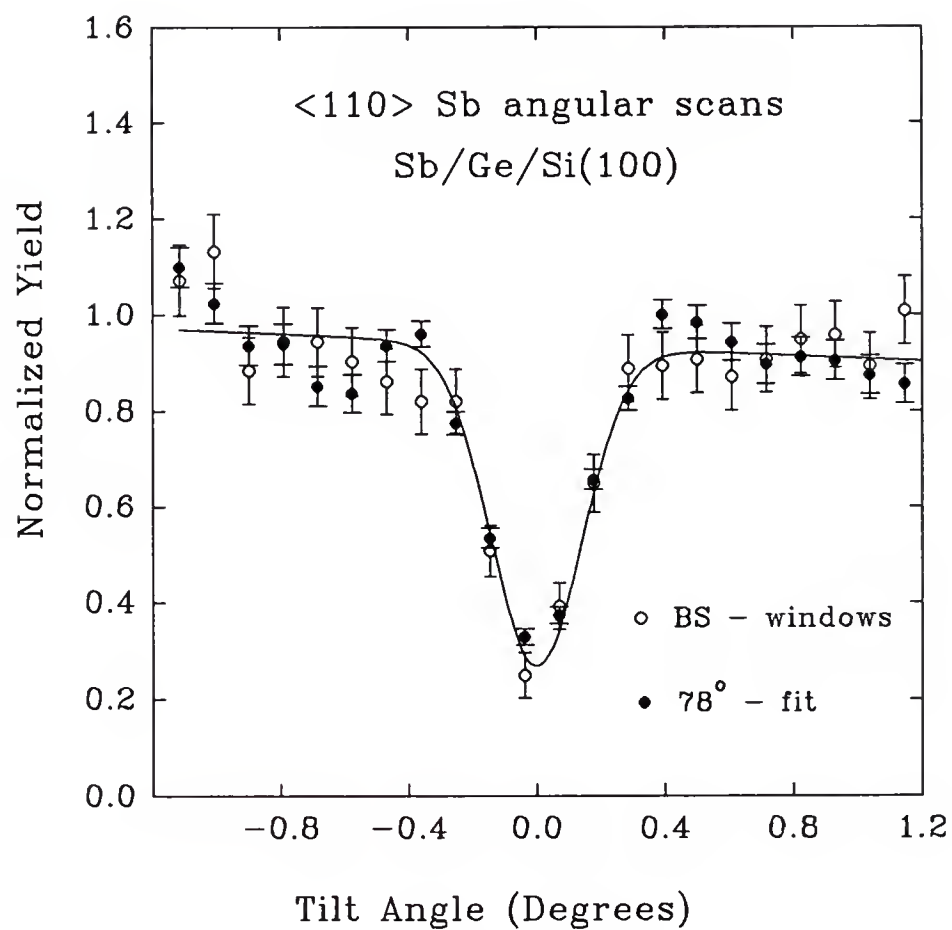


Figure 6-4. Comparison of angular scans generated with peak fits and peak sums. The filled circles were generated using DATAFIT.FOR on data from the 78° detector. The open circles were generated using CUT.FOR on data from the 150° detector. The solid line is to guide the eye. Error bars represent uncertainties due to counting statistics.

checked against those given using CUT.FOR, and in all cases agreement was found. Our data were then corrected for a small change in the scattering cross section across an angular scan due to the difference in energy [Dygo94] loss of channeled and random ions. This task was accomplished by correcting the yield from the channeled fraction of the beam at a given tilt angle. In order to understand this step, imagine the yield from the overlayer (y) to be composed of two components, a channeled and random, such that,

$$y = y_R + y_C \quad (6-1)$$

Here, $y_C = y (1 - \chi_{Si})$, where χ_{Si} is the normalized yield from the Si host for a given datum (this gives the random component of the beam). The channeled component ($y - y_R$) then is corrected by a factor equal to the square of the channeled beam energy divided by the random beam energy. This factor, for 2.5 MeV He^+ incident on a 5000 Å crystal, amounts (at maximum) to a 3.2% correction to y_C in the $\langle 100 \rangle$ channel, a 6.3% correction in the $\langle 110 \rangle$ channel, and 5.2% in the $\langle 111 \rangle$ channel.

Comparison of Experimental and Calculated Angular Scans

As previously mentioned, for a quantitative determination of an adatom site, the computer-calculated scans (chapter 5) are compared to the experimental scans. In this section, the process by which this comparison was accomplished for these studies will be explained. The data used to illustrate the procedure are from Ge on Si(100) (0.6 ML) and Sb data from the Sb/Ge/Si sample. The same basic procedure was applied to both data sets. For the earlier Sb/Si data, a simplified procedure was used, since the dimers were reported as symmetric in the literature [Richt90] before our experiments began. The general process is detailed here because a considerable effort was expended in order to develop a procedure which was accurate, inclusive of all reasonable possibilities, and unbiased.

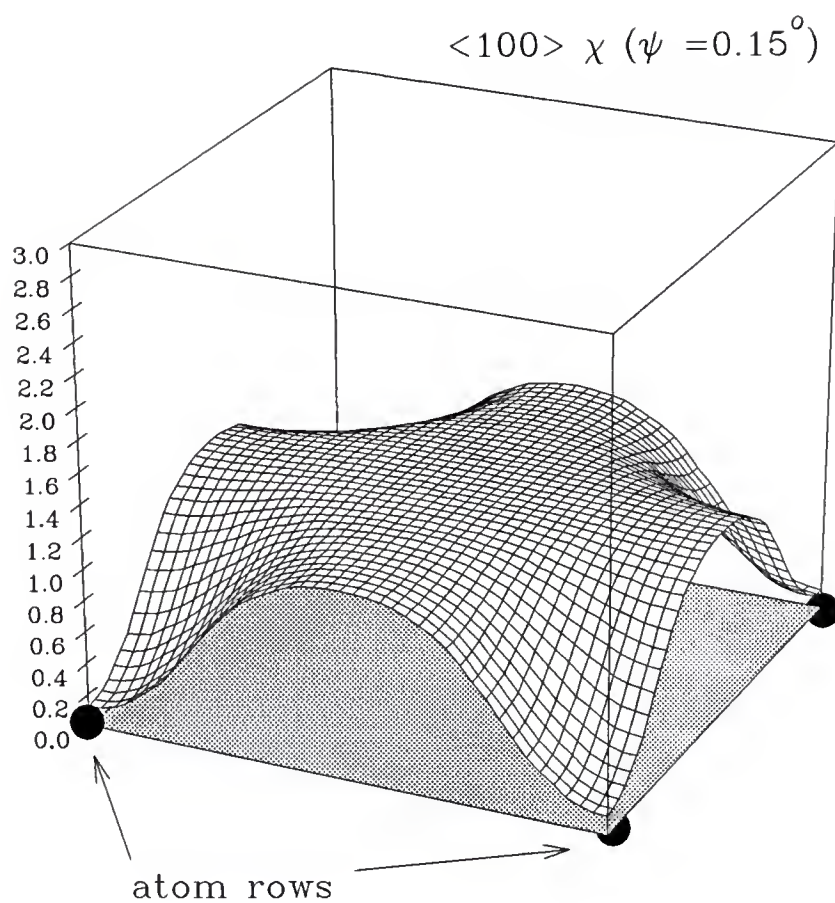


Figure 6-5. Calculated scattering yield across the $\langle 100 \rangle$ channel in Si for a 2.0 MeV He beam with $\psi=0.15^\circ$. The conditions for the calculation were the same as for figure 5-6 (except for the tilt).

From figure 5-6, it is clear that the position of the adatom on the surface (in the channel) will have a great influence on the scattering yield from that adatom. Figure 6-5 illustrates how this yield depends upon the tilt angle, ψ , across the $\langle 100 \rangle$ channel, given the same conditions as those of figure 5-6. The scattering yield is directly related to the flux distribution (see chapter 5) in the channel, which is clearly a strong function of ψ . Herein lies the utility of the angular scans. These concepts are further illustrated in figure 6-6, which shows calculated scans across the $\langle 100 \rangle$ axial channel. These scans are for a single adatom on the $\langle 100 \rangle$ surface, for a crystal thickness of 5000 Å, and for a range of displacements in x from substitutional (in steps of 0.1 Å). Scans across this direction are very sensitive to such displacements, which for purposes of analyzing dimerized surfaces, are related to changes in the surface-projected dimer bond length. Note, however, that this axial direction ($\langle 100 \rangle$) is parallel to z , making scans across this channel completely insensitive to the degree of relaxation of the surface. Sensitivity to z displacements can be accomplished in the off-normal directions ($\langle 110 \rangle$ and $\langle 111 \rangle$), which observe both x and z displacements. This aspect is illustrated in figure 6-7, which shows calculated angular scans across the $\langle 111 \rangle$ axial direction from sites with a fixed x -position ($x=1.49$ Å), but with variable z positions (again in steps of 0.1 Å). Thus, by combining the information from the three directions, the adatom site can be pinpointed.

Basically, pinpointing the adatom configuration becomes the problem of finding the coordinates in a multiple dimensional space (parameter space) that give the calculated scan demonstrating the best agreement with the data. The parameters are the positions and vibrational amplitudes of the impurities. In general, for a site determination, the adatoms are assumed to lie in a perfectly formed overlayer, with each adatom having a well-defined local structure and well-defined local bonding geometry (see discussion in chapter 11). For our studies of dimerized adlayers, two

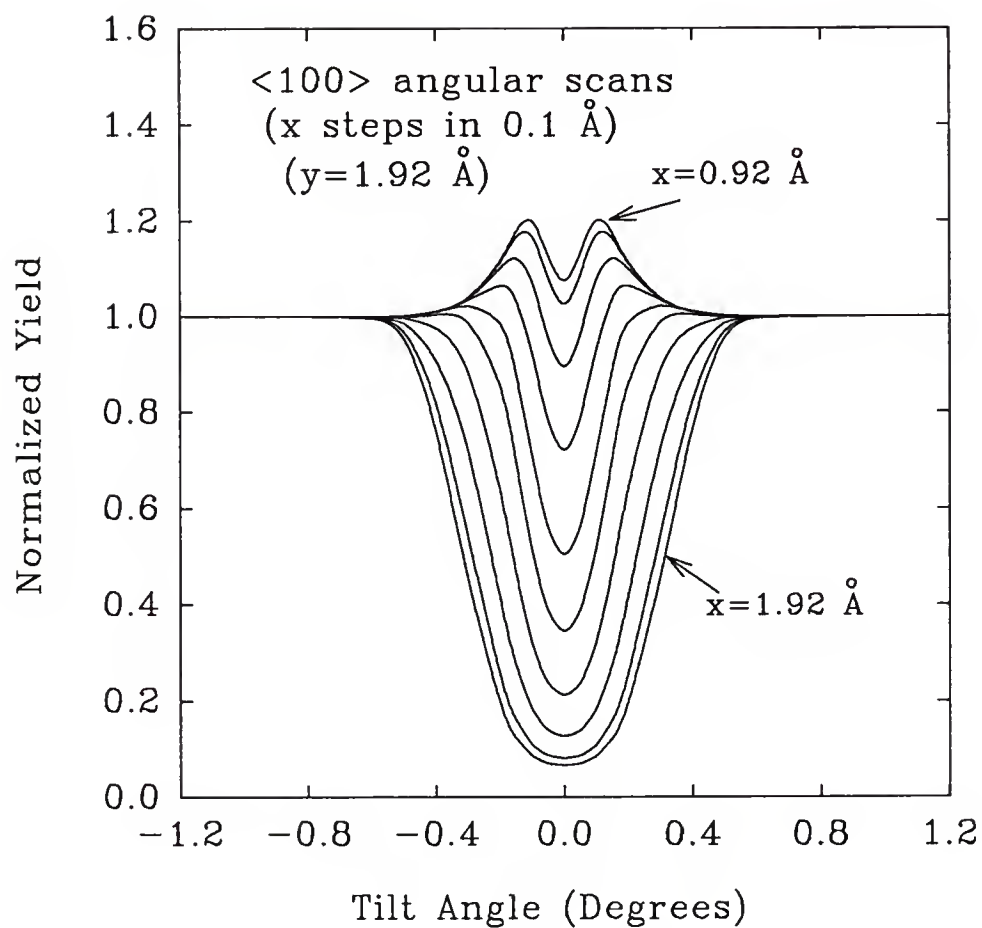


Figure 6-6. Variation in calculated angular scans with x . Shown are calculated scans across the $\langle 100 \rangle$ channel for a symmetric dimer with variable dimer bond length. The calculation was for 2.0 MeV He ions and for a sample thickness of 5000 \AA .

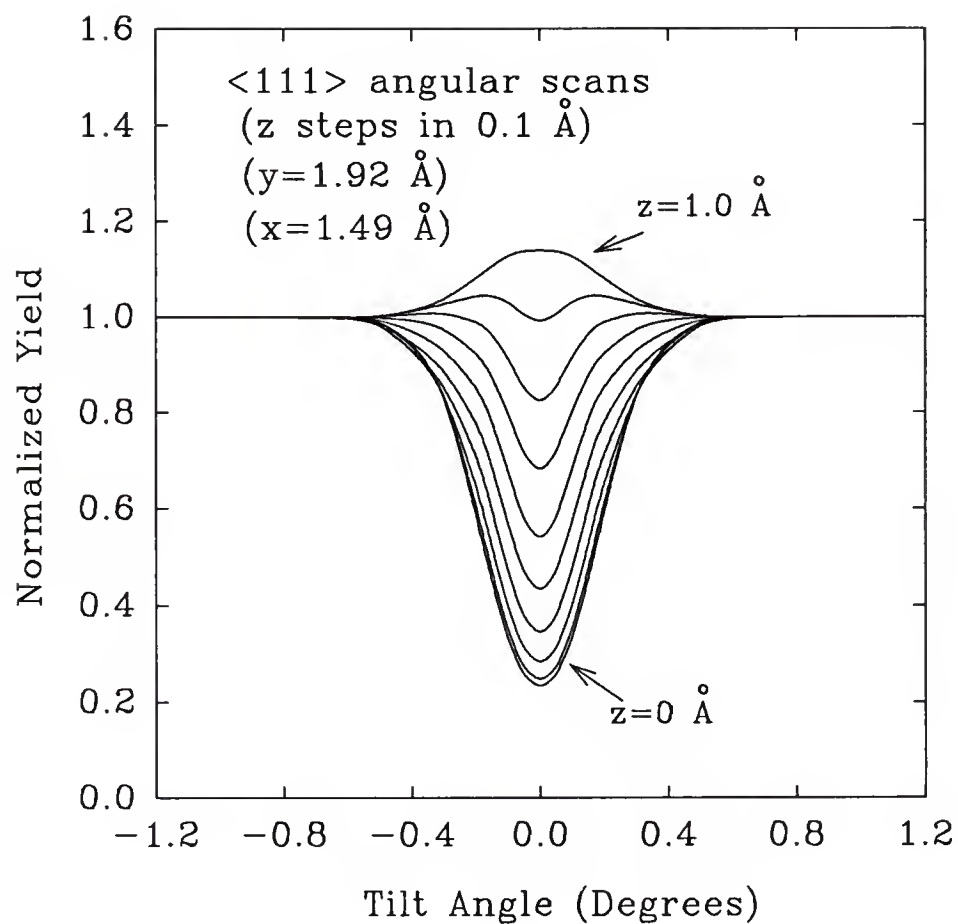


Figure 6-7. Variation in calculated angular scans with z . Shown are calculated scans across the $\langle 111 \rangle$ channel for a symmetric dimer with a fixed dimer bond length and with a variable height above the $\langle 100 \rangle$ surface. The calculation was for 2.0 MeV He ions and for a sample thickness of 5000 Å.

adatom sites were allowed for each atomic species. Two were allowed because of the possibility of buckling in the dimers, which leads to two distinct adatom sites. For the systems we studied, the dimers were not expected to twist out of the plane defined by the surface normal (z) and the gross direction of dimerization (x), so the y positions were fixed. The result is a total of 4 positional degrees of freedom to define the dimer structures. Another potential degree of freedom was ρ . In practice, when a believable value was available in the literature for this quantity, or when the value could not be determined readily from the data, ρ was not used as a fitting parameter. For instance, for the Ge/Si data, a calculated [Aler89] value was used (see chapter 9) for the Ge adatoms. The same is true for the Ge in the Sb/Ge/Si system (see chapter 10), whereas the Sb vibrational amplitude was varied in all studies. Therefore, in general, there were five parameters used in the fitting of the data (the vibrational amplitudes for two dimer atoms were assumed to be equal). The values for the best fit for these were determined by calculating the χ^2 goodness-of-fit indicator for each adatom configuration, considering the data in three crystallographic directions ($\langle 100 \rangle$, $\langle 110 \rangle$ and $\langle 111 \rangle$), and finding the configuration which gave the lowest value. Each direction was weighted equally. The χ^2 minimization was carried out over a grid which spanned all reasonable values of the fitting parameters, and the parameters were varied independently.

In order to facilitate visualization of the fitting procedure, the regions in parameter space giving adequate fits were identified by representing the fitting procedure graphically. Gross estimates of some of the best-fit parameters could be obtained by observing the behavior of χ^2 and considering an experimental angular scan about one of the axial directions. Figure 6-8 shows χ^2 as a function of two parameters for the Ge/Si data from a comparison of calculated scans in the $\langle 100 \rangle$ direction with the $\langle 100 \rangle$ experimental data. The parameters shown are the x -positions for

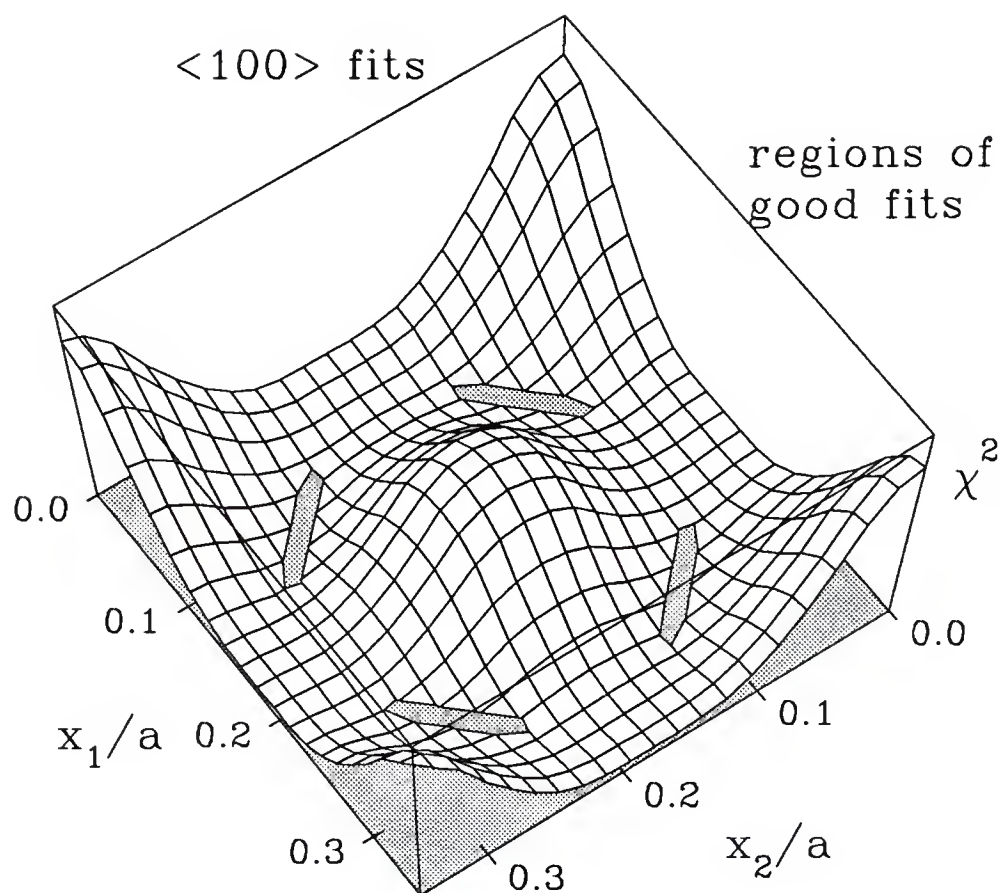


Figure 6-8. Three dimensional representation of fitting procedure. Depicted is the quality of the fits (as measured by χ^2) as a function of the x positions of the two dimer atoms (asymmetric dimers). The shaded regions represent those regions of parameter space giving good fits. Units are fraction of a lattice constant.

calculations compared with the Sb data from the Sb/Ge/Si system. In this figure, the shaded regions represent those values of the two x-coordinates which give fits having a χ^2 below a reasonable cut-off, or, in other words, those configurations giving good fits. By creating similar plots for all three directions, and all parameters, it is assured that no reasonable geometry is overlooked, and the volume in parameter space considered can be reduced substantially.

In general, it is not sufficient to consider the three axial directions independently for a final determination of the bonding geometry. However, when the χ^2 is evaluated considering all channeling directions, the possibility of a simple graphic representation is lost, since the dimensionality of the space is increased. A procedure was developed to circumvent this inconvenience. The parameters were used to calculate quantities of physical significance and these were used to display the data graphically. For instance, from the x and z positions of the two adatoms making up the dimer, the dimer bond length and dimer tilt, two quantities of interest for this study, were calculated for each set of adatom sites giving a good fit. This intermediate comparison then allowed an inspection in two dimensions of the configurations which were consistent with the data, inclusive of all parameters. Also, the uncertainties associated with the determination of these quantities then were determined readily by measuring the volume in parameter space encompassing the good fits. An example of such an analysis is shown in figure 6-9. Plotted is the dimer tilt angle versus dimer bond length represented by the calculated scans that were consistent with the experimental angular scans across all three axial directions for the Ge/Si system. Since the parameters giving good fits tend to cluster, it is reasonable to assume that the correct structure, within error bars, has been discovered. In practice this procedure is facilitated by sorting the configurations by χ^2 value, a task which is accomplished easily with a simple FORTRAN sorting routine (XTRACT.FOR).

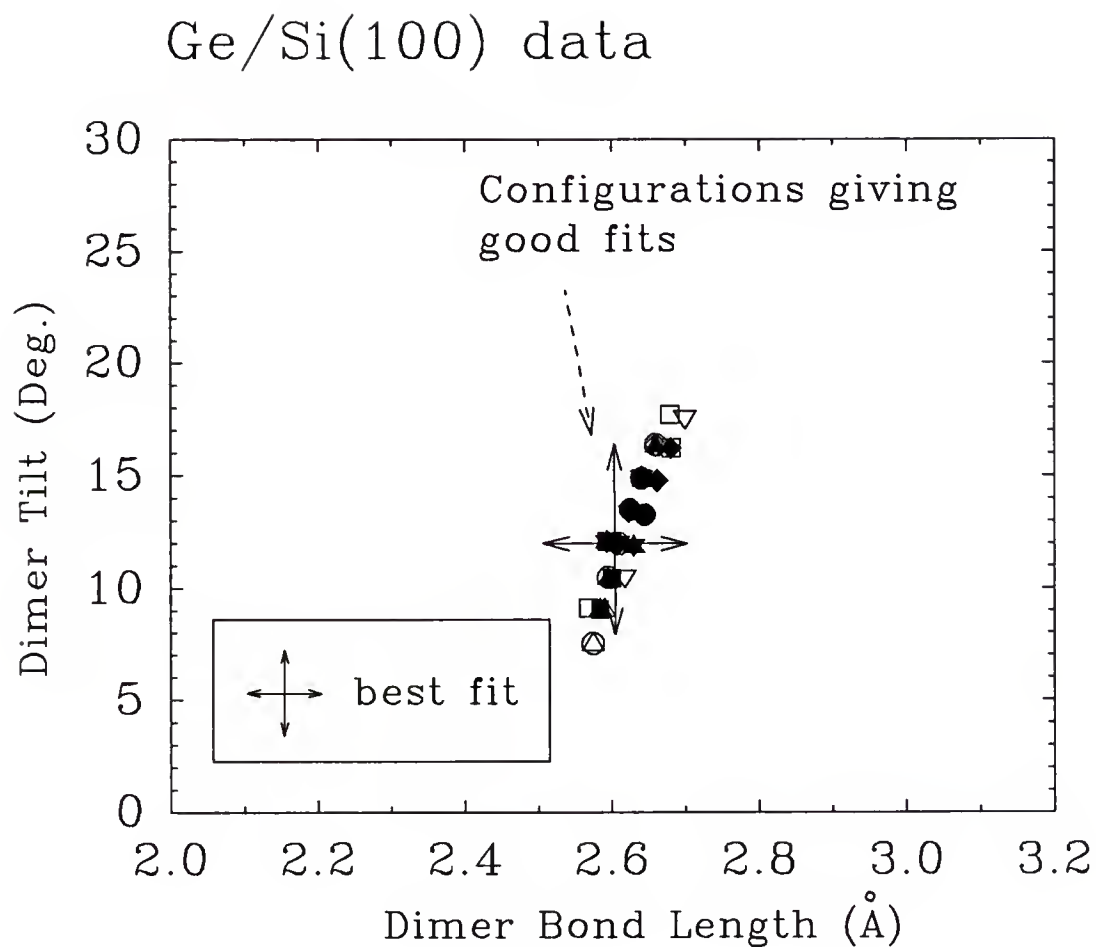


Figure 6-9. Representation of fits using physical quantities. Shown as the filled circles are the dimer configurations giving acceptable fits to the Ge experimental angular scans. The dimer bond length and dimer tilt were calculated from the x and z adatom coordinates.

CHAPTER 7

THE Si(100) SURFACE

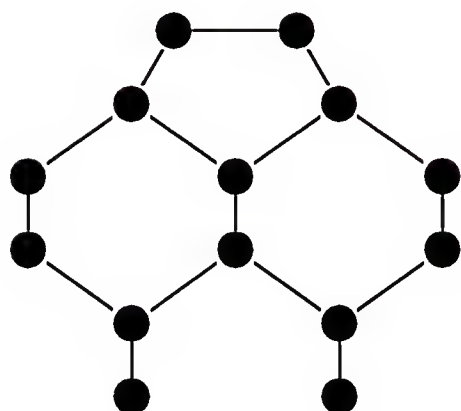
The importance of Si in today's society cannot easily be overstated. The semiconductor-device industry relies almost exclusively on structures grown on the Si(100) surface [Shur90] for the production of the integrated circuits which power computers and electronic devices, which, in turn, drive the progress and productivity of our modern world. For this reason, and because of an interest in surfaces on a fundamental level, there has been a tremendous effort in the surface science community to elucidate the structure and dynamics of the Si(100) surface. This effort began in the 1950's when Schlier and Farnsworth [Schl59] observed with LEED that the Si(100) surface symmetry could not be explained by a simple bulk termination of the crystal. This finding led to the conclusion that the surface atoms moved from their bulk positions [Schl59]. Later studies [East80; Mönc79] supported this early work, and a picture of the surface as composed of dimers began to emerge. This reconstruction was eventually understood as a consequence of the high energy cost of the two dangling bonds per surface atom caused by the cleaving of the crystal at the $\langle 100 \rangle$ plane. By forming bonds in the surface layer the number of dangling bonds is reduced, and, thus, the surface free energy is reduced.

As more was learned, it was suspected, primarily on the basis of works such as a medium energy ion scattering (MEIS) study by Tromp [Trom81a; Trom81b; Trom83] and calculations such as those by Chadi and others [Ch79; Verw80; Yin81], that the surface atoms participated in what were described as "asymmetric dimers". By this it was meant that the dimer bond was tilted with respect to the surface plane. It was thought that this tilting was a consequence of a partially covalent dimer bond [Ch79]. This interpretation was also consistent with core-level photoemission data

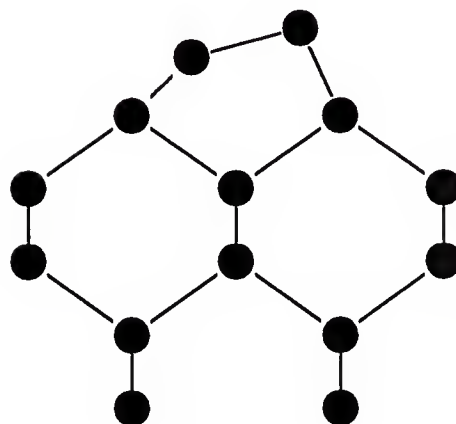
[Himp79; Hil80; Uh81; Hoof80], in which surface shifted components altering the photoemission lineshapes suggested a charge transfer between the two atoms participating in the dimer bond. Symmetric and asymmetric dimers on the $\langle 100 \rangle$ surface are shown schematically in figure 7-1 as viewed along the $\langle 011 \rangle$ direction (a) and from the top (b). See, also, figure 5-7.

The interpretation of the data up to the era of the STM was becoming consistent. Then, in the mid 1980's STM images (see figure 5-7) [Trom85; Hame86] of clean Si(100) surfaces showed symmetric-looking dimers, a finding which inspired a whole bevy of experiments [Jaya93; Uh92; Land92] and calculations [Redo82; Robe90; Tang92; Dabr92, Stil92] aimed at determining the symmetry of the dimers. This enthusiasm was fueled primarily by the calculations, most of which showed only a slight energy difference between asymmetric and symmetric dimers. There have been numerous interpretations of the available data, leading to a controversy which is yet to be resolved. Recent work has helped, however. STM images [Wolk92] obtained at lower temperatures (120K) show asymmetric dimers in greater abundance than for the room temperature surfaces. This excess has led to the acceptance of a picture (first proposed by Hamers *et al.* [Trom85]), which has the dimers flipping at room temperature [Dabr92, Weak90] between two degenerate states (defined by the two possible tilting configurations) such that the STM observes an averaged, symmetric looking dimer, with asymmetric dimers stabilized only at defects or at lower temperatures. The argument is physical, since the time scale for the passing of the STM tip over a dimer is such that a dimer will flip $\sim 10^9$ times during the measurement [Dabr92]. This interpretation seemed be consistent with all the available data. However, until recently, no direct observation of the dimer symmetry had been reported.

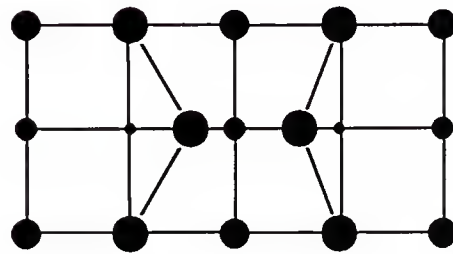
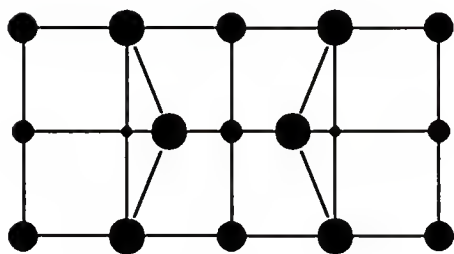
Symmetric



Asymmetric



a) side view



b) top view

Figure 7-1. Geometric representation of symmetric and asymmetric dimers on the Si(100) surface. a) Side view (along $\langle 011 \rangle$); b) Top view (along $\langle -100 \rangle$).

Over about the past three years, there has been a separate but related discussion concerning the origin of shifted components in core level spectra taken from clean Si surfaces and Si(100) surfaces covered with Ge, Sb, or Sb/Ge. Photoemission has proven an extremely useful tool for clarifying issues on the Si(100) surface. On the clean surfaces, two shifted components were observed (labeled S and S') originally [Himp79; Himp80; Wert91]. These were attributed to the up (S) and down (S') dimer atoms, and, as discussed above, were thought to arise from charge transfer between the two (therefore, a partially ionic bond). Interest continued on the problem, and a similar study of Ge on Si(100) provided some intriguing data [Lin91]. These data showed that the S' component from Si lingered until ~ 2 ML of Ge coverage, after the S component vanished at ~ 1 ML. This behavior indicated that the two components were not both from the dimer atoms. Additional evidence supporting this interpretation came from the Ge core-level spectra, which showed the S' component only after greater than 1 ML of Ge growth. Since Ge at this coverage should continue to grow as would Si, rendering the Si below bulklike [Lin91], these data led to the conclusion that the S component was from the top layer (with covalent bonds), and the S' component from the second layer down. These authors turned out to be half right.

A recent study [Land92] with excellent resolution on the Si(100) surface has shown additional components (obscured by the bulk signal), and has identified the S peaks with the up dimer atom and the S' peak with the second layer atoms. This study is also supported by a nice work with Sb, Ge, and Si [Cao92]. The latter work showed that both Si and Ge exhibit the S' peak when directly under a reconstructed layer, be it Sb, Ge, or Si. The S component, however, was observed only from reconstructed Si or Ge surfaces. Further, the S' component vanished from buried layers (for instance Si buried under thick Ge layers). The consensus then seems to be

that the S shifted component comes from the up dimer atom, and is a result of a partially ionic dimer bond. The physical origin of the S' component, coming from the second layer, however, is unclear.

CHAPTER 8

Sb ON THE Si(100) SURFACE

Motivation

Considerable attention has been focused in recent years on the growth of group V elements on Si. These studies have been motivated partly by the desire to improve the quality of III-V epitaxy on Si, and by an interest in achieving abrupt doping profiles. Much progress has been made in clarifying the growth of As and Sb on Si(100) at temperatures sufficiently high that ordered structures are formed on the surface [Richt90; Trom92a; Trom92b; Beck88]. It has been shown by STM [Köhl92; Beck88] that As terminates the Si(100) surface with symmetric-looking (see discussion in chapter 7 of STM images of dimer structures) As-As dimers. On the terraces, As-As dimers form a virtually defect-free overlayer and passivate the Si surface at one ML [Köhl92; Beck88; Uh86]. The low defect density is usually attributed to the small lattice mismatch between Si and As (~1%) and the convenient coordination, which allows each As atom (5 valence electrons) to satisfy its valence requirements by bonding to three atoms (two Si and one As). In this configuration, all dangling bonds on the surface are filled. By comparison of angle resolved photoemission data and *ab initio* pseudopotential calculations, Uhrberg *et al.* [Uh86] determined the structure of the As dimers.

Similar progress has been made on the Sb deposited Si(100) surface. This surface would be expected to behave somewhat like the As/Si case, since As and Sb are both group V elements. In the Sb case, however, the lattice mismatch with the substrate is larger by ~12%. Indeed, for the Sb/Si(100) surfaces grown at elevated temperatures and annealed at 550°C, the surface as viewed by STM [Richt90; Nogami91] consists of short strings of symmetric-looking Sb-Sb dimers, interrupted

by numerous antiphase domain boundaries. For these surfaces, photoemission [Cao92] and ion scattering data [Slij92] suggest that the underlying Si reconstruction has been lifted by the Sb adlayer. Finally, the structure of the annealed surface has been determined using SEXAFS [Richt90].

Considerably less progress has been made in our understanding of the geometry of these interfaces at low processing temperatures, where adatoms impinging on the surface have insufficient mobility to form an ordered overlayer. The absence of long range order, however, does not imply the absence of a preferred bonding site or the lack of well-defined structural features that are possible precursors to the formation of an ordered epitaxial overlayer. One major barrier to progress has been that in the presence of considerable disorder, properties such as bonding geometry are inaccessible to many of the standard surface probes. However, if the long range goals of a theoretical understanding of and control of interface formation are to be achieved, it is of utmost importance to probe the microscopic processes that precede epitaxy.

The $\sim 1\text{ML}$ low temperature surface has been investigated by a number of techniques, such as: core level photoemission [Rich89a; Rich89b], high energy electron diffraction (HEED) [Rich89a; Rich89b], STM [Richt90, Noga91, Rich89a], SEXAFS [Richt90; Richt91], medium energy ion scattering (MEIS) [Slij92] and LEED [Richt90; Richt91; Noga91; Cric93]. Although there is not a true microscopic characterization of the Sb overlayer among these, some of this work hints at the structure of the surface. The MEIS study finds that the Sb deposited at room temperature forms a 2-D film at first, with 3-D Sb islands at higher ($>1\text{ML}$) coverage [Slij92]. They attribute the formation of the 2-D overlayer to the energy gained by chemisorption. This is based on their determination of the Sb binding energy on the Si(100) surface, $E_b = 2.6 \text{ eV/dimer}$. They point out that, since the dissociation energy

of Sb tetramers in the gas phase is 1.2 eV/dimer (the deposited species is Sb_4), there exists an incentive of 1.4 eV/dimer for dissociative chemisorption. They also conclude that upon ~ 1 ML Sb deposition the Si dimers on the surface are broken, and the Si atoms become bulklike. These authors, however were not able to comment on the bonding geometry of the Sb overlayer. Consistent results were found by the group of Rich *et al.* These authors find that for Sb deposition at 320-370°C, the top-layer Si becomes bulklike [Rich89b] (although in similar paper they conclude the Si reconstruction persists [Rich89a]). Again, however the Sb layer is described only as disordered, and no conclusions are drawn concerning the atomic bonding geometry. In still another work, it also has been suggested that the Sb forms a disordered overlayer with three-dimensional Sb clusters upon low temperature deposition [Richt91].

We have used transmission ion channeling to probe the bonding geometry of the Sb terminated Si(100)- 2×1 surface formed at temperatures below 375°C. Some samples were studied for Sb deposition as low as -40°C, with ion scattering conducted at room temperature. In all of these experiments, we have exploited a fundamental advantage of transmission channeling: It probes the registry of adatoms with respect to the underlying substrate directly, and, therefore, does not depend on long range order in the overlayer.

Experimental

After the cleaning and characterization by LEED of the Si surface, Sb was deposited from a boron nitride effusion cell. Sb was deposited at a number of temperatures, however the two most common were 375°C and room temperature. For Sb depositions at 375°C, the surfaces were exposed to several monolayers in order to insure saturation of the surface with Sb. For the room temperature Sb deposition, rates were near 0.05 ML/min. After Sb deposition, the samples either were not

annealed, or annealed at 375°C or 550°C for 15 min. All samples having been exposed to 1 or more ML's had ~1 ML Sb coverage after annealing at 375°C, which is consistent with thermal desorption studies placing a saturation coverage of Sb at elevated temperatures (>150°C) of ~ 1 ML [Barn86]. LEED patterns were noted for all samples and were (1x1) with weak, diffuse 1/2 order spots for samples having ~1 ML of Sb, independent of deposition temperature or annealing. With one sample, the experimental stage was cooled by thermal contact via a copper braid to an *in situ* liquid nitrogen reservoir and Sb deposition occurred at -40°C. Our observed LEED patterns are consistent with the vast majority of LEED results reported by other groups for the Sb/Si(100) surface [Richt90; Richt91; Noga91].

All coverages were determined by RBS. A beam of 2.5 MeV He⁺ ions, collimated to < 0.08° angular divergence, was directed onto each sample after it was transferred to the scattering chamber. Possible effects of ion beam irradiation on the sample were monitored carefully. A small loss of Sb during a typical angular scan was observed due to sputtering of the overlayer by the ion beam. In a separate dosing run, the Sb loss per unit ion-dose was measured for ions incident in a random direction. Shown in figure 8-1 is the Sb yield versus dose used to determine the loss rate. The data are shown as the filled circles, and the dashed line is a linear regression, with the coefficients indicated in the inset. The Si yield is included, which, as expected, shows no dependence on dose. The computer calculations used to fit the data have been corrected to reflect this loss, and the slope in the scans with tilt angle is indicative of this (see figure 8-2 and 8-3). We have no evidence that ion irradiation alters the *site* of the Sb. To the contrary, channeling minimum yields have been measured both before and after angular scans were completed on a particular beam spot, and have shown no significant difference.

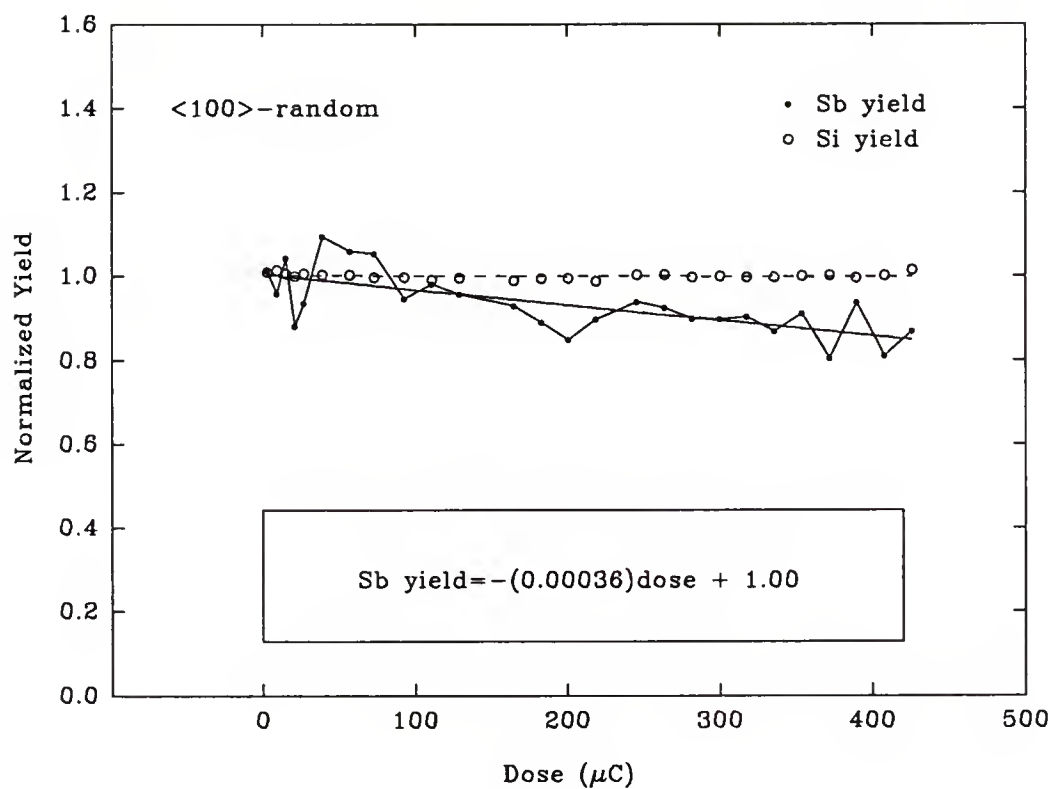


Figure 8-1. Sb loss rate (random incidence). The filled circles represent scattering from the Sb overlayer. The open circles represent scattering for the Si substrate. The solid line is a linear regression used to characterize the Sb loss rate due to sputtering by the ion beam.

Results and Discussion

Annealed Surfaces

Figure 8-2 shows angular scans across three low-index crystallographic directions for Si(100) samples on which Sb was deposited at 375°C, followed by an anneal at 550° C. Coverages for the three samples are $0.9 \pm 0.14\text{ML}$. In this figure the hollow (filled) squares represent the normalized ion scattering yield at a particular tilt angle (ψ) from the Si substrate (Sb overlayer). The solid lines represent calculated angular scans for the Si host (lower curve) and the adsorbed Sb (upper curve). The decrease in the experimental and calculated angular scans for the Sb from left to right is due to the Sb loss with dosing discussed earlier. Three parameters were varied in the calculated scans to determine the best fit to the Sb data; the lateral displacement in the (100) plane (related to the dimer bond length) corresponding to modified bridge site positions, the position of the Sb adatoms perpendicular to the (100) surface (related to the relaxation), and the thermal vibrational amplitude, ρ_{Sb} , of the adatoms. Because it is difficult to distinguish a static displacement along the $\langle 100 \rangle$ direction from a change in ρ_{Sb} , we fixed ρ_{Sb} (taken to be isotropic) and the lateral displacement in the (100) plane first using the (100) angular scan, which is not sensitive to static $\langle 100 \rangle$ displacements. The (110) and (111) scans then were fit by adjusting the position of the Sb perpendicular to the (100) plane.

From fig. 8-2, the calculated scans are seen to be in good agreement with the experimental data in all three channeling directions. These calculated scans represent a modified bridge site, with an Sb-Sb bond length of $2.8 \pm 0.1 \text{ \AA}$, within experimental uncertainty of the bulk Sb bond length (2.90 \AA), and the value found by Richter *et al.* using SEXAFS [Richt90] (2.88 \AA). Assuming an Sb-Si bond length of 2.63 \AA (equal to the sum of the covalent radii of Si and Sb), and the measured Sb-Sb dimer length of 2.8 \AA , the calculated position of the Sb dimers perpendicular to the (100) plane

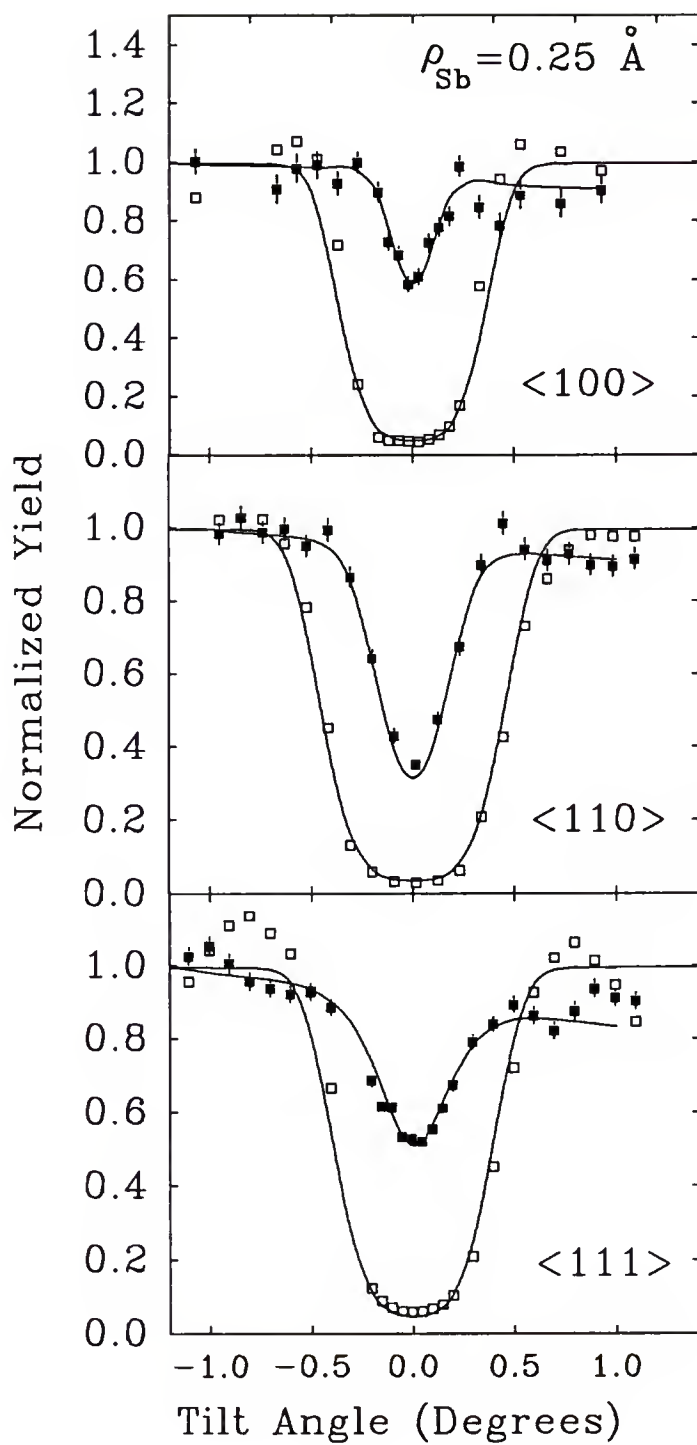


Figure 8-2. Scattering yield as a function of tilt angle for Sb overlayer (closed squares) and Si host crystal (open squares) in three low index crystallographic directions for samples annealed at 550°C. Calculated angular scans are shown as solid lines.

corresponds to a relaxation of the top layer of Si atoms toward the substrate of 0.09 ± 0.07 Å. The magnitude and direction of this relaxation are comparable to those found using *ab initio* pseudopotential calculations for the As-terminated Si(100)-2x1 surface [Uh86]. For the two-dimensional thermal vibrational amplitude, we obtain a value of 0.25 ± 0.1 Å. The Sb bulk value is 0.14 Å, calculated with the Debye model for a temperature of 25°C. Enhanced vibrational amplitudes at surfaces are not unusual, and are often a factor of two larger than bulk values [Wood86].

Unannealed Surfaces

The three angular scans shown in figure 8-3 represent two different annealing conditions. For the data obtained in the <110> direction, the Sb was deposited with the substrate held at 375°C (leaving 1 ML coverage) and not treated further. For the data obtained in the <100> and <111> directions, 0.6 ML of Sb was deposited at room temperature, with no further anneal. Again, hollow squares indicate yields from the Si host, and filled squares indicate yields from the Sb overlayer. As above, the dimer geometry giving the best agreement between calculated and experimental angular scans was determined. The resultant calculated scans are shown as the solid curves. In comparison to the samples annealed at 550°C, we find that the vibrational amplitude for these unannealed samples is increased slightly to $\rho_{\text{Sb}} = 0.3 \pm 0.1$ Å, the dimer bond length is unchanged, 2.77 ± 0.14 Å, and the relaxation towards the substrate is again 0.09 ± 0.07 Å. Overall, the data are very similar for the two annealing conditions, a comparison which provides compelling evidence for Sb-dimer termination of the surface for growth temperatures as low as room temperature. Indeed, the data suggest that on both surfaces, nearly all of the adatoms are in identical, perfectly formed dimers. This interpretation follows from the fact that despite the lack of mobility on the low-temperature surface and its presumed disorder, the angular scans, which are very sensitive to the average position of the overlayer

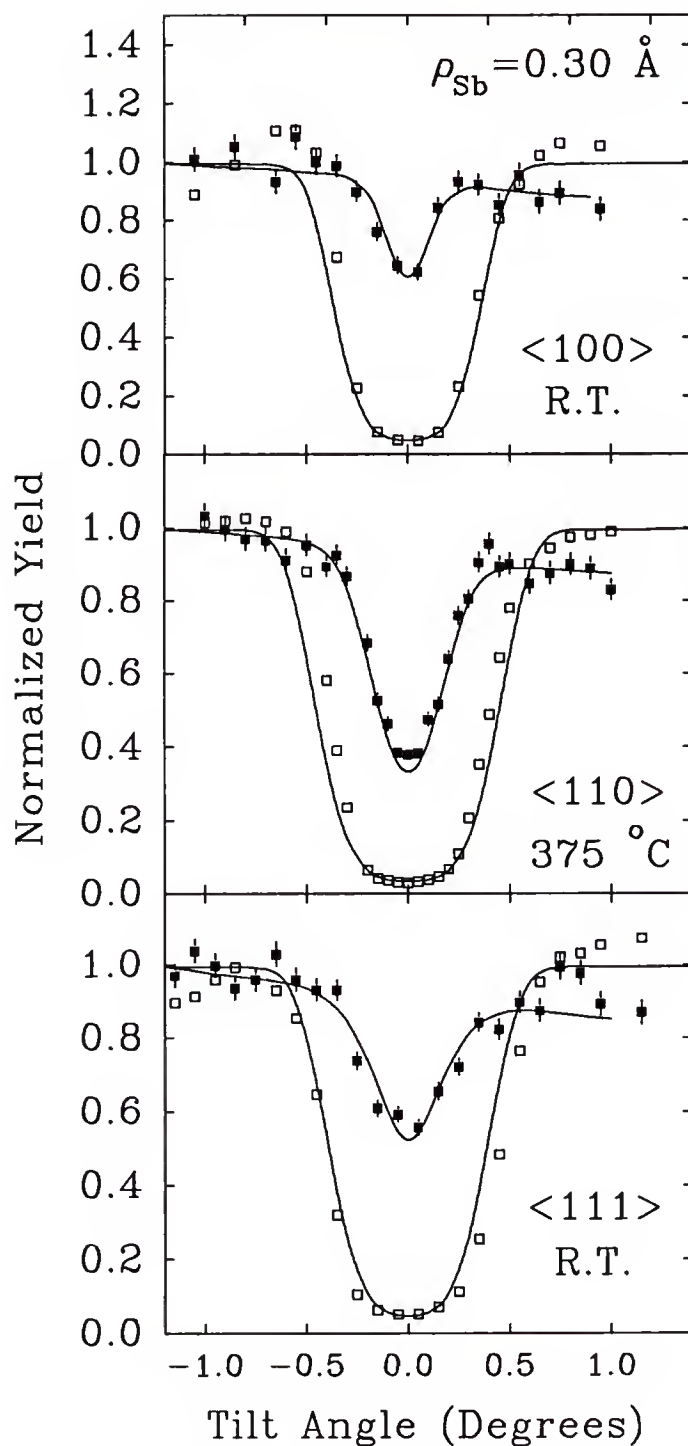


Figure 8-3. Scattering yield as a function of tilt angle for Sb overlayer (closed squares) and Si host crystal (open squares) in three low index crystallographic directions for samples not annealed at 550°C . For the $\langle 110 \rangle$ data, Sb deposition was at 375°C . For the $\langle 100 \rangle$ and $\langle 111 \rangle$ data, deposition was at room temperature. Calculated angular scans are shown as solid lines.

atoms relative to the substrate, show essentially no variation from those of the annealed surfaces. This insensitivity is highlighted in figure 8-4, where the angular scans from the annealed and unannealed surfaces are shown together. In fact, we find the scans highly reproducible, for a wide range of annealing conditions temperatures (-40°C to 375°C) and deposition rates. Figure 8-4, is also representative of the scatter typically observed in our data.

For the unannealed surfaces, the quality of the fit for a dimer site precludes a substantial contribution from other sites (for instance, bulk-like or amorphous). This observation rules out 3-dimensional Sb growth as reported in the SEXAFS study [Richt91], since such growth would alter completely the shapes of the angular scans. Also ruled out is the persistence of the Si dimer reconstruction [Rich89a], if one makes the reasonable assumption that dimer formation requires breaking of dimer bonds in the layer below. In fact, because of the presence of only one dangling bond per surface atom for the *dimerized* Si(100) surface, a saturation coverage of 1/2 ML is expected for Sb on a reconstructed Si surface. On the one hand, STM images of the Sb:Si(100) surface annealed below 550°C appear blurry, bumpy and highly disordered [Rich89a; Richt91]. Based on these images, for coverages near 1 ML, several groups have been unable to determine the structure with STM. On the other hand, an anneal at 550°C produces clear images of short Sb dimer strings with numerous antiphase defects [Richt90; Noga91]. The LEED patterns for all annealing temperatures (including room temperature) are very similar [Richt90; Richt91; Noga91]. Based on these observations, we propose that Sb forms a random array of dimers and lifts the reconstruction of the Si(100) surface for annealing temperatures of room temperature to 375°C and that the dimers become mobile at higher temperatures, and arrange themselves into short dimer strings.

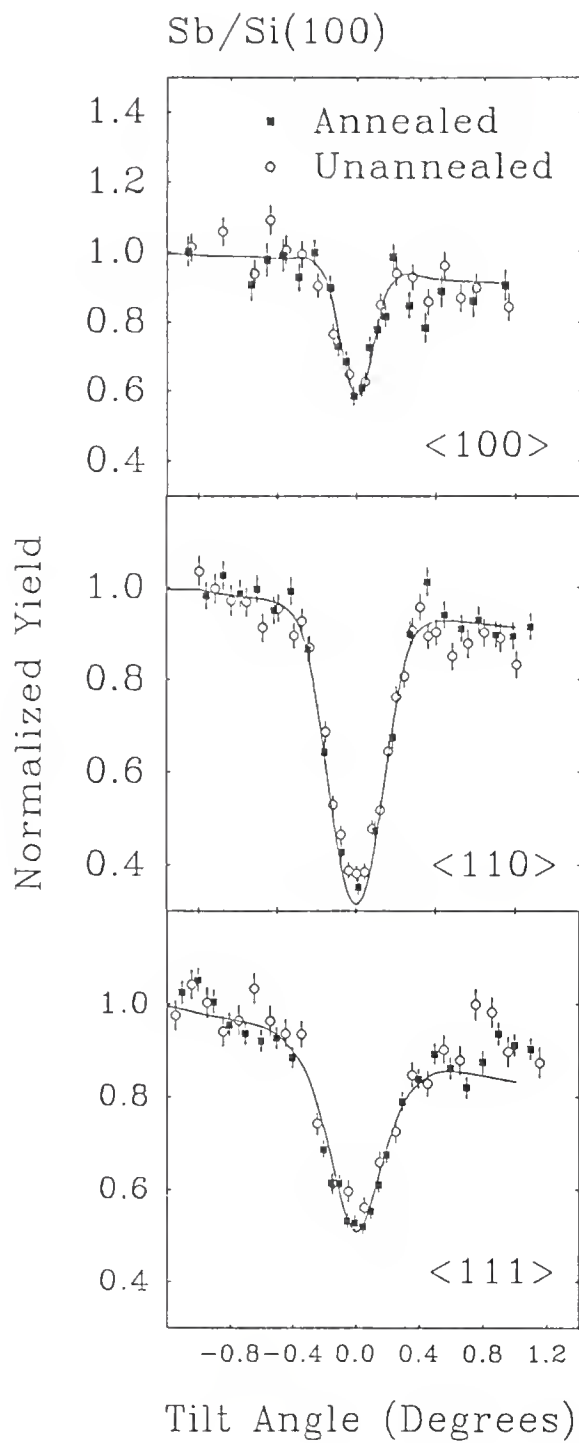


Figure 8-4. Annealed and unannealed data. The Sb data of figures 8-2 and 8-3 are plotted here together for comparison. Note the similarities in all three axial directions.

This idea is schematically illustrated in figure 8-5 (a and b), where the dimer atoms are represented by the filled circles. Both figures were generated with a simple Monte Carlo program (STRINGS.FOR) which distributes dimers randomly on the surface in dimer-like positions. For the bottom figure (unannealed model), the dimers were allowed to occupy any unoccupied dimer sight on which they attempted to land. For the upper figure (annealed case), the dimers were forced to desorb with some probability unless adsorbing onto the edge (end or side) of an island. Separate probabilities were used for the ends (parallel to dimers) and sides (parallel to dimer rows) of the islands and several combinations were tried. The combination represented in this figure lets the dimer stick 1/2 of the time when not on an edge and 1/100 of the time when not on an end. This choice mimics the tendency of the Sb to form dimers strings. The resultant surface has the same qualitative appearance as the STM images of Nogami *et al* [Nogami91]. Because the longest dimer strings observed in the STM images are shorter than the coherence length of the LEED electrons, a random array of dimers and short dimer strings with antiphase defects give rise to the same LEED pattern [Wood86].

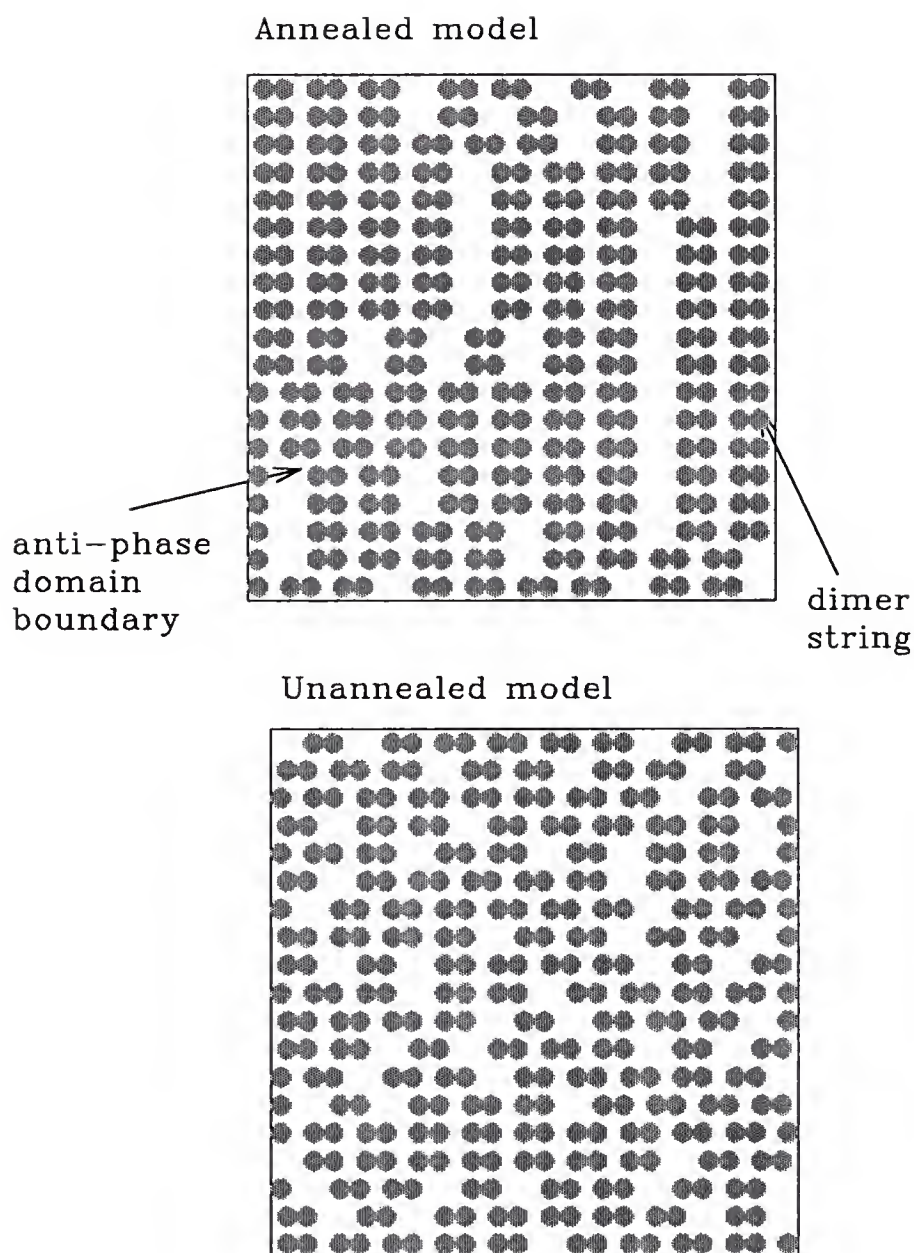


Figure 8-5. Model of Sb-Sb dimer strings. Shown are computer generated (see text) images of the dimerized Sb/Si(100) surface. The top plot shows dimer strings interrupted by antiphase-domain boundaries. The lower plot shows randomly distributed dimers.

CHAPTER 9

Ge ADSORBED ON THE Si(100) SURFACE

Motivation

A system closely related to the clean Si(100)-2x1 surface is that of Ge deposited on Si(100). Ge and Si both are group IV semiconductors and bond tetrahedrally [Shur90, p. 13] in the bulk. It has been shown that for Ge coverage (Θ_{Ge}) approaching 1 ML, the general surface structure is similar (dimers are formed) to that of the heavily studied clean Si(100)-2x1 surface. In many respects the Ge layer might be expected to act as a visible substitution for the otherwise experimentally inaccessible top Si layer. However, the Ge-Si lattice mismatch does lead to significant differences.

Several groups have reported on sub-monolayer Ge growth on Si(100). The interest in this system is due not only to the technological importance of Ge heteroepitaxial layers on Si, but also to the fact that, because of the chemical similarity (they are both group IV) of the two species and a ~4% [Boye61] lattice mismatch, this system has become a model for the study of strained-layer growth. For the surface at low coverages (<1 ML), several groups have shown (with STM) that elongated islands of asymmetric Ge-Ge dimers are the dominant feature [Kna192; Iwaw92a; Iwaw92c; Mo91]. STM images have in some cases also shown the presence of symmetric dimers [Iwaw92c; Kna192] on the surface, with the percentage of symmetric species increasing with decreasing coverage. For this surface, as the Ge coverage nears 1 ML, recent LEED [Köhl92; Trom93] and STM [Köhl92, Trom93, Iwaw92b] studies have revealed a complex 2xN structure. The structure was first observed as stripes on the surface appearing in STM images, and later was characterized [Köhl92] with high

resolution LEED. Here, the satellite spot indicating the higher order symmetry was followed as a function of coverage. In this picture, at low coverage, the surface is riddled with missing dimers, which, with increasing coverage, order to form missing dimer rows (perpendicular to the dimer strings), eventually leading to a $\sim 2 \times 1$ structure at 1 ML. Although the mechanism for this evolution is not completely understood, it is presumably a consequence of the strained growth, and has in fact been reproduced using a simple elastic model of Ge growth on Si(100) [Ters92].

A recent x-ray standing waves (XSW) study [Font93] by Fontes *et al.* addressed the bonding geometry of Ge adatoms on this surface. The XSW technique measures the fluorescent yield from impurity atoms excited in the spatially varying field created by the interference of the incoming x-rays and those scattered from crystallographic planes of the substrate [Vlie91; Hert85; Bedz85]. The technique, therefore, measures the average position, or center of mass, of the impurities with respect to the given set of planes. In the Fontes [Font93] study the authors concluded that the Ge adatoms form asymmetric Ge-Ge dimers. Since only two planes were measured, the data were insufficient to determine the coordinates of both atoms of a dimer, but by comparing the data to a simple, two-parameter model for the surface structure, the authors found a dimer bond length of 2.60 Å and a dimer tilt of 12.1°. Their study was for deposition at 500°C and reported on coverages below 1 ML.

That and other recent work [Jin94] has helped to clarify some of the important issues on this surface. Nevertheless, prior to our studies, the dimer geometry had only been measured with this one technique, and other issues concerning the growth needed to be further addressed. Our experiments on this surface were begun in order to determine the local bonding geometry of the Ge adatoms on the Si(100) surface. In addition, we acquired data on this surface for a range of coverages in order to investigate the possibility of coverage dependence below one ML.

Experiment

After cleaning, Ge was deposited on the Si windows held at 300°C from a Knudsen cell with a graphite crucible at a rate of 0.1-0.15 ML/min. The pressure during evaporation remained in the 10^{-10} Torr range, and the samples were allowed to cool slowly (1°/sec) after the evaporation. The LEED patterns after Ge deposition remained largely unchanged except that the background increased slightly on some samples. The quality of the patterns indicated that the Ge typically formed a well-ordered overlayer [Zang88], consistent with numerous reports for growth of Ge on Si(100) [Lyma91b, Köhl92, Goss85ab]. The samples then were transferred into the scattering chamber and analyzed with either a 2.0 MeV or 2.5 MeV beam of He^+ ions. Typically, different beams spots were used for each angular scan. Ge coverages were determined with the Ge adsorbed side of the sample facing the incoming ion beam by counting in the backscattering detector and integrating current.

Results and Discussion

Adatom Adsorption Sites (0.6 ML)

Figure 9-1 shows angular scans across three low-index axial channeling directions for a Si(100) thin window with a Ge coverage of 0.6 ML [Gran94b]. Each filled circle represents the integrated Ge yield (ordinate) from a spectrum taken at a given tilt angle (abscissa) about the axial channel. Likewise, open circles represent scattering from the Si substrate (i.e., a substitutional position) integrated over the thickness of the thin window ($\sim 5000 \text{ \AA}$). Also shown are calculated angular scans for an asymmetric dimer-like position (solid curves, discussed below) and for a substitutional position (dashed curves). The dotted curve (on the $\langle 100 \rangle$ scan) is a calculated scan for a symmetric Ge dimer with a bulk Ge-Ge bond length, which is clearly not consistent with the data. The upper solid lines in figure 9-1 are the calculated angular scans which give the best fit for the case of an isotropic vibrational

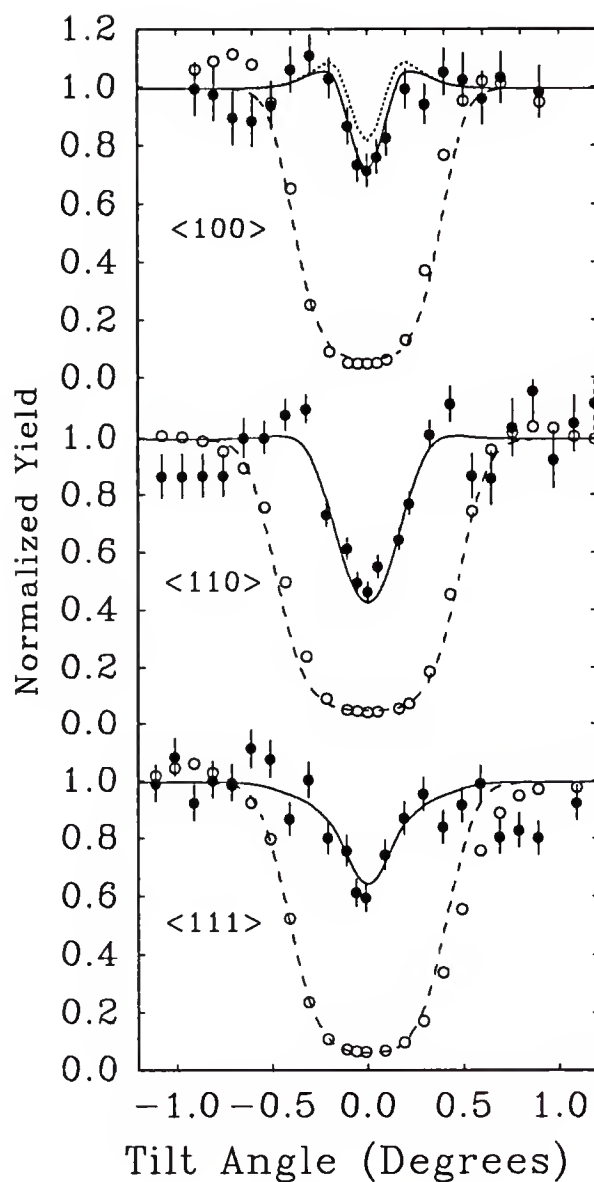


Figure 9-1. Angular scans across three low-index axial directions for samples with 0.6 ML of Ge deposited at 300°C. Filled circles represent the integrated Ge yield and open circles represent the integrated Si yield. The solid and dashed curves are calculated scans for a modified bridge site (discussed in text) and a Si-substitutional site, respectively. Also shown is the calculated scan for a symmetric dimer (dotted curve) with the bulk Ge-Ge bond length. The error bars represent uncertainties due to counting statistics.

amplitude. The asymmetric dimer site represented has a Ge-Ge dimer bond length of 2.6 ± 0.1 Å and a dimer tilt with respect to the surface of $12^\circ \pm 4^\circ$. If z is defined as the direction normal to the surface, we find the average z -position of the Ge to be 0.25 ± 0.20 Å above the normal bulk-terminated (not reconstructed) surface Si-lattice positions. The vertical dimer atom separation (Δz) is 0.5 ± 0.2 Å, and the center of the dimer bond is laterally displaced by 0.07 ± 0.03 Å. The agreement in bond length and tilt angle with the previously mentioned XSW [Font93] work is surprisingly good, and the magnitude of the tilt is consistent with calculated values for reconstructed Si(100) and Ge(100) surfaces (see table 8-1). The dimer bond length is not in agreement with calculated [Need87; Chad79; Robe90] values, which, for Ge (Si) homoepitaxy, consistently predict a Ge (Si) dimer length that is smaller than or approximates the bulk Ge-Ge (Si-Si) bond length of 2.45 Å (2.35 Å) [Boye61]. This comparison is illustrated in table 8-1, which shows our results and the results of other workers (theoretical and experimental) reporting asymmetric structures for clean Si and Ge surfaces and for the Ge/Si system.

Table 8-1. Comparison of results

ref.	technique	bond length (Å)	dimer tilt
1 (Ge/Si)	Transmission ion channeling	2.6	12°
2 (Ge/Si)	X-ray standing waves	2.60	12.1°
3 (Ge/Si)	Energy minimization calcs.	2.48	19°
4 (Si)	Transmission electron diffraction	2.19	6.8°
5 (Si)	Empirical tight-binding calcs.	2.35	11.69°
6 (Si)	Energy minimization calcs.	2.21	6.93°
7 (Si)	Energy minimization calcs.	2.26	7.87°
8 (Ge)	X-ray diffraction	2.44	21°
9 (Ge)	Molecular dynamics calcs.	2.46	13.01°

1-Gran94b; 2-Font93; 3-Jin94; 4-Jaya93; 5-Chad79; 6-Robe90; 7-Yin81; 8- Ross92; 9-Need87.

One difference between our results and the findings of Fontes *et al.* is the slight expansion of the surface (Ge position in z) into the vacuum observed in this study. The calculated Si-host scans in figure 9-1 represent a substitutional site with a vibrational amplitude of 0.14 Å, compared to the bulk vibrational amplitude of 0.11 Å (calculated with the Debye model for 25°C).

Our model is summarized schematically in figure 9-2. Transmission ion channeling determines the adatom positions relative to the bulk lattice, so some information about subsurface lattice distortions can be inferred. Using our experimentally determined Ge positions (represented by filled circles), the positions of the subsurface Si atoms shown in figure 9-2 (open circles) have been estimated with the well known Keating model [Keat66; Appe78b]. This scheme has been used in the past for the prediction of the vibrational properties of atoms near the surface of Si crystals [Tier86; Stei87], for the interpretation of x-ray diffraction experiments [Conw89; Lohm92], and, in general, as a simple model to understand the elastic energetics of tetrahedrally bonded systems [Ters92]. In this model, the elastic energy (E_K) is given by a sum of bond stretching and bond bending contributions,

$$E_K = \sum \alpha_{ij} (|\mathbf{r}_{ij}| - d_{ij})^2 + \beta \sum (\mathbf{r}_{ij} \cdot \mathbf{r}_{ik} + \frac{1}{3} d_{ij} d_{ik})^2, \quad (9-1)$$

where the first sum is over all bonds and the second over all bond pairs. Here, \mathbf{r}_{ij} is the vector from atom i to atom j , and d_{ij} is the nominal bond length (d_{ij} can represent a Si-Si bond or a Si-Ge bond). This model assumes tetrahedral bonding, and is, therefore, not expected to reproduce all atomic positions exactly. This restriction is especially relevant when electronic considerations, such as rehybridization or partial covalent bonding are important. However, since the bond stretching term dominates in equation 9-1 and we are not trying to predict the Ge atomic positions, the model can be expected to give a qualitative idea of the magnitude and direction of the subsurface Si atomic displacements. So, using 5 atomic Si layers (180 atoms), doubly

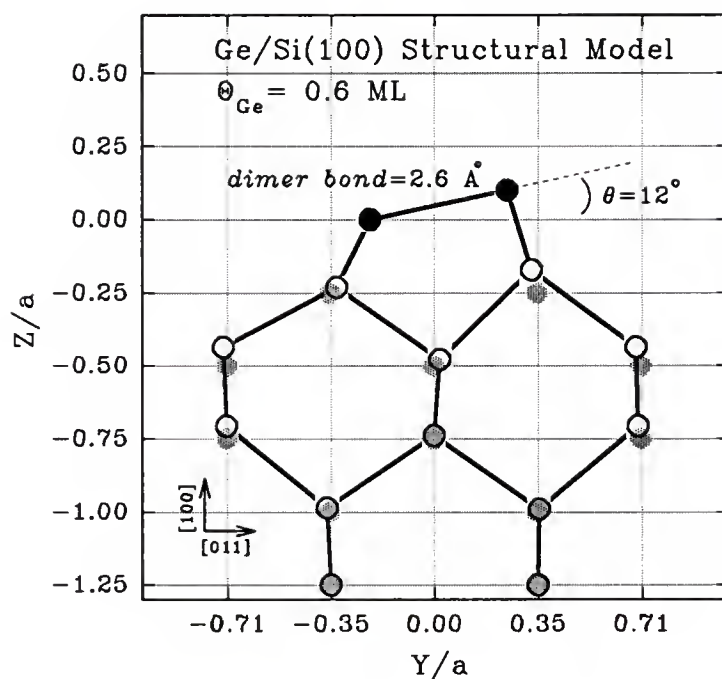


Figure 9-2. Structure of Ge overlayer. Filled circles represent Ge adatoms and shaded circles represent bulk-terminated Si positions. The open circles represent Si atoms displaced from bulk positions due to the surface reconstruction. These positions were estimated with the Keating model (see discussion in text) and should be considered as qualitative. Units are fraction of a lattice constant ($a=5.429 \text{ \AA}$).

periodic boundary conditions, and with the Ge atoms fixed at experimentally determined positions, subsurface Si atomic positions were found by minimizing equation 9-1. The minimization was accomplished with a variable metric method [Pres92] using the FORTRAN code STRAIN.FOR [Gran93b]. We have used parameters $\beta/\alpha_{ij}=0.0910$ (0.102 for the Si-Ge interface). These were obtained from the papers by Steif *et al.* [Steif87] and Appelbaum and Hamann [Appel78b] and chosen to describe the elastic constants for bulk crystals. We also demanded that the lowest Si layer be bulk-like, and assumed a 2x1 overlayer symmetry. As a test case, an ideal (bulk-terminated) crystal was produced having several displaced atoms. It was observed that these defects were repaired quickly by the minimization procedure, yielding a perfect crystal.

The use of transmission channeling (and many other techniques) for adatom site determination is ultimately limited by a lack of understanding of the vibrational properties of the surface impurity of interest. Some calculations on the vibrations of surface atoms have been performed for the reconstructed Si(100) surface [Tier86; Aler89], however, little work has been devoted to the study of the vibrational properties of Ge adsorbed on Si(100). For this study, we assumed that both Ge atoms participating in the dimer bond exhibit identical and isotropic vibrations, and took the magnitude of the two-dimensional root-mean-square thermal vibrational amplitude for the Ge to be $\rho=0.14$ Å. This value is obtained by taking the average of the three Cartesian components of the (weakly anisotropic) amplitude calculated for Si dimers on Si(100) by Alerhand *et al.* [Aler89]. While it is true that transmission channeling can be used to determine the vibrational amplitudes of surface atoms, in cases where the atomic configuration for the calculated best fit to the data varies with the assumed vibrational amplitude, this task can prove difficult or impossible.

The Ge dimer geometry also was investigated with allowance for asymmetric vibrational amplitudes. If the vibrational amplitude is allowed to vary independently for each axial direction, we find large, anisotropic vibrations give the best fit. In this case, $\rho_{100}=0.19\text{\AA}$, $\rho_{110}=0.45\text{\AA}$, $\rho_{111}=0.29\text{\AA}$, are the two-dimensional vibrational amplitudes for the respective directions. For the dimer bond length, we get 2.35\AA , near the bond length for bulk Ge. The quality of the fits is better than that obtained with a fixed ρ (above) since three more parameters are introduced. However, the dimer tilt becomes very large (31°), leading to unphysical subsurface distortions. Because of this and the large vibrational amplitudes (especially in the $\langle 110 \rangle$ direction), we do not consider this geometry as plausible. This treatment did not simulate anisotropic vibrations in the strict sense, since the adatom's distribution in each channel (*i.e.*, projected in a plane perpendicular to a given axial direction) was still represented by a two-dimensional Gaussian which was isotropic in that plane. Further, no consistency among the three projected amplitudes was forced. In a separate analysis, however, the true projections of anisotropic vibrations on the Si(100) surface were accomplished with the code ANISO.FOR [Gran93c], and the distributions were represented by two-dimensional matrices in each plane. This analysis proved difficult because of an overparametrization of the data. However, if reliable values for the anisotropy of vibrating surface atoms for a system were available, this method of analysis would be preferred.

Coverage Dependence

Shown as the inset in figure 9-3 (points) are angular scans about the $\langle 111 \rangle$ axial channeling direction. The solid curves are fits to the data of a line plus an inverse Gaussian, used for consistent characterization of the data. The scans display clearly a systematic broadening and deepening with coverage. From these data the minimum yields (ratio of the integrated yield in the channeling direction to the yield in a random

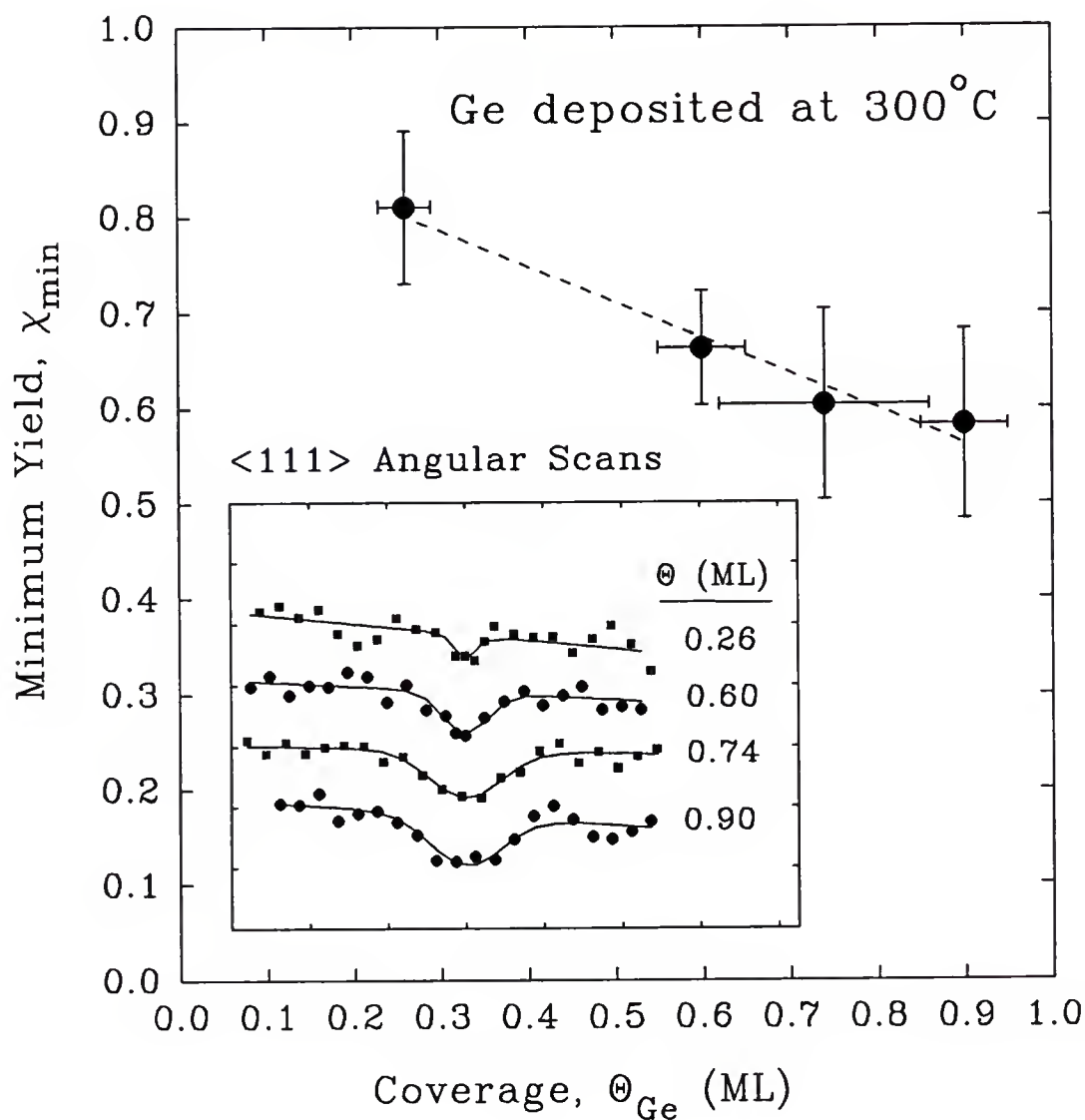


Figure 9-3. Dependence of overlayer structure on coverage. Shown is the minimum yield (solid circles) as a function of Ge coverage in the <111> direction. The dashed line is a linear regression. The inset gives the raw <111> angular scans with solid lines (fits to a line minus a Gaussian) to characterize the data. The vertical error bars represent uncertainties due to counting statistics and were calculated considering the counts in one channeling and one random spectrum per point. Since the minimum yields were found from fits to the spectra, the error bars may be overestimated.

direction) as a function of Θ_{Ge} were extracted. These results are illustrated as the filled circles in figure 9-3. Also shown as figure 9-4 is a similar plot for the $\langle 100 \rangle$ direction. It is clear from the trend shown (especially in the $\langle 111 \rangle$ direction) that our data are not consistent with identical and perfectly formed dimer rows throughout this range of coverage, since a surface composed of such rows would show absolutely no dependence on Θ_{Ge} . Instead, our results indicate that submonolayer Ge growth is complicated by a dimer geometry that changes with coverage, or a coverage-dependent mixture of adatom sites.

While we have not been able to develop a simple model to explain these results fully, there are several effects expected for this surface which would influence the channeling measurements. One likely influence is significant second layer growth at coverages approaching 1 ML. This second layer occurs as incoming Ge forms dimers on the incomplete Ge layer rather than on uncovered Si regions. As dimers are formed, the reconstruction of the Ge atoms underneath is broken and they are forced into substitutional positions. STM images from Knall and Pethica [Kna192] suggest that at a coverage of 0.8 ML, roughly 5 % of the Ge resides in the second layer. Further, core-level photoemission spectra show a shifted component attributed to a small amount of second layer growth at coverages as low as 0.3 ML [Lin91]. In addition, at deposition temperatures of 400°C, it has been shown that some Si-Ge intermixing occurs for thicker Ge layers (~ 4 ML) [Saka92]. Since the minimum yield from a substitutional Ge adatom is very low (~ 0.05), even a small percentage of such sites would cause a noticeable reduction in the overall minimum yield from the overlayer.

Another mechanism which could influence the angular scans is the occupation of so-called "random" sites by some fraction of the overlayer. With regard to this possibility, it is reasonable to suspect the presence of some random component on the

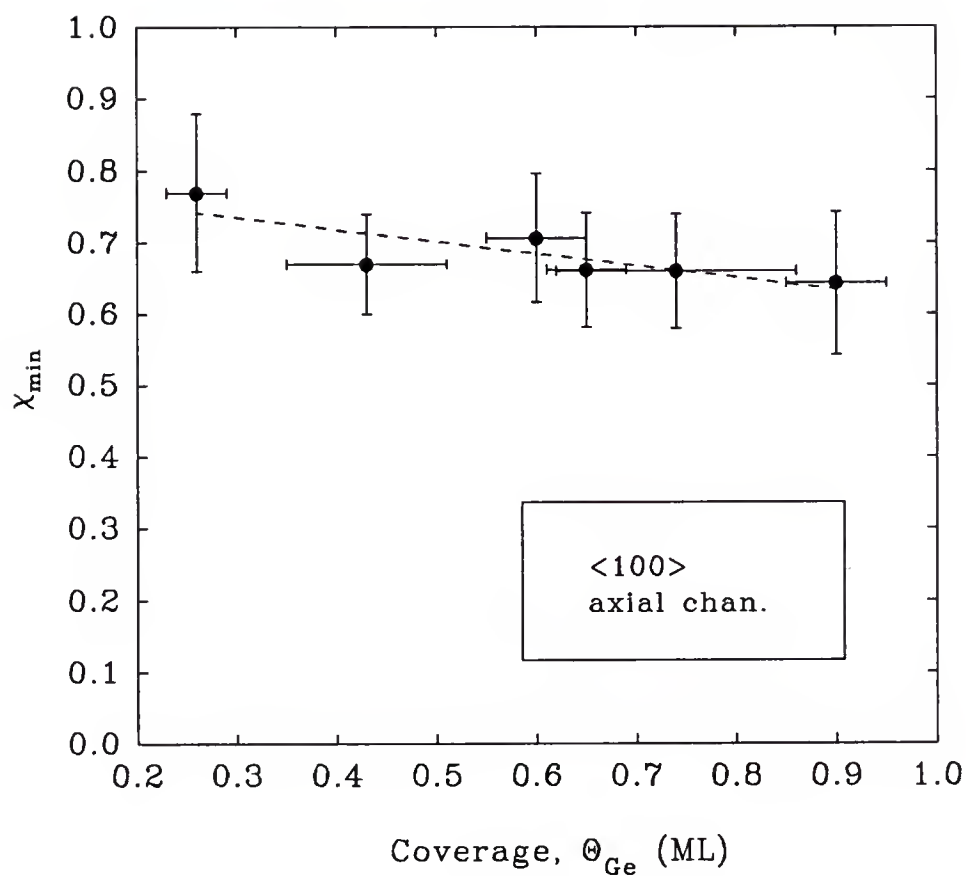


Figure 9-4. Depth of channeling dip as a function of Ge coverage for the <100> channel. Shown are the depths (filled circles) of angular scans across the <100> axis for the Ge/Si(100) samples. The dashed line is a linear regression. Error bars were estimated as in figure 9-3. This data does not display any obvious trend, however, lends support to the obvious trend in the <111> direction (figure 9-3).

surface arising from bonding to step edges and other defects. One further might expect that at low coverage the Ge adatoms are preferentially bonded to such sites. A preference of this kind would lead to an approximately constant number of random Ge sites. The minimum yield for such a component is one, and since the fraction of this component would decrease with increasing coverage, such a mechanism would lead to a decreasing minimum yield with Θ_{Ge} . At lower coverages, the angular scans do indeed approach that for a random overlayer (flat line). Also, it has been observed that the fraction of symmetric dimers observed with STM increases at low coverage [Iwaw92a; Kna192]. While it has been shown that the absolute determination of dimer symmetry with an STM should be approached with some trepidation [Wolk92], the STM might be expected to reliably detect local differences in surface properties.

In general, the submonolayer growth of Ge on the Si(100) surface appears to be more complicated than the original suggestions. In those, the process below 1 ML was viewed essentially as a replication of Si homoepitaxy. The strain induced by the $\sim 4\%$ lattice mismatch does seem to influence the growth. As discussed earlier, this interpretation also is supported by the observation that the surface is characterized by a complex $2 \times N$ structure [Kna192; Köhl92; Trom93; Iwaw92b; Ters92], where N varies with Ge coverage. The presence of this structure should affect our results, although it is unclear exactly to what extent, since STM cannot measure the registry of the overlayer with the substrate accurately. For these reasons, we focused on a coverage of 0.6 ML for our determination of the Ge dimer geometry. Here we expect that the vast majority of the dimers will be surrounded by other Ge-Ge dimers and reside on Si. We hope to minimize any random contribution or contribution from non-ideal dimers at lower coverage while avoiding the possibility of significant second layer growth at higher coverage. In a more practical light, our scattering signal is strong only at coverages greater than ~ 0.4 ML.

CHAPTER 10

Sb DEPOSITED ON PSEUDOMORPHIC Ge ON Si(100)

Motivation

Epitaxy on the Si(100) surface of Ge layers in the presence of Sb has been studied widely in recent years. This intense effort has been due mainly to the interest in so-called "surfactant-mediated growth" (a recent review has been written [Tour93]). This term refers to the observation that the characteristics of the growth of Ge on Si(100) can be altered dramatically when the growth occurs in the presence of Sb, or some other surfactant. An example of this type of behavior was first observed for the Sb/Ge/Si system by Copel *et al.* [Cope89] using MEIS (1989). They studied layered structures (period ~ 100 Å) of Ge and Si in the $\langle 100 \rangle$ orientation. Si normally grows on Ge in the Volmer-Weber growth mode (immediate islanding) [Volm26]. These authors found, however, that the growth of the Si could be made to proceed layer-by-layer (Frank-Van der Merwe growth mode) [Fran49] by introducing a monolayer of Sb at the growth front. They also concluded that the growth mode of Ge on Si(100), normally Stranski-Krastanow (layer-by-layer growth followed by islanding) [Stra38], could be changed to layer-by-layer to a thickness well beyond the critical thickness [Mat74] (transition point from layer-by-layer to islanding). Similar effects have been observed since by numerous other groups. Initially it was thought that the mechanism causing the surfactant behavior was the lowering of the surface free energy of the growing layer. In this picture, the reduction lead to layer-by-layer growth above the critical thickness for island formation. It was shown later however, by Tromp and Reuter [Trom92a], using low energy electron microscopy (LEEM), that surfactant effects likely were caused by the kinetic limitation of the growing species in the

presence of the surfactant. This finding has since been confirmed in part with beautiful TEM micrographs [Eag193] showing Ge islands, formed in the presence of Sb, after long periods of annealing. These images suggest that the equilibrium structure of the surface is not characteristically flat, but that, given time, the kinetically limited Ge atoms will island. However, the island shape in the presence of Sb did show a preference for the $\langle 100 \rangle$ facet. The growth of Ge on Si(100) in the presence of Sb thus seems to be controlled by both kinetic and energetic considerations. Although heavily studied because of this interest in Sb-assisted growth of Ge on Si, little structural information is available on a microscopic level. Also, the question of exactly how the Sb atoms affect the growth of Ge, on the microscopic level, remains unanswered.

The techniques used to study this system include some of the most contemporary and powerful: extended x-ray adsorption fine structure (EXAFS) [Saka92], MEIS [Col89; Horn91; Cope90], reflection high energy electron diffraction [Saka92; Oste92c; Oste93], STM [Köhl92], transmission electron microscopy [Eag193; Oste93; Oste92b; Horn91; Oste92a; Oste92c], ultra-violet photoelectron spectroscopy [Cope90] and x-ray photoelectron spectroscopy [Cope89; Cao92; Ost92c; Cope90]. Most of the structural information for the surface, however, has been inferred from studies of Sb on the clean Si(100) surface, and from indirect probes such as core-level photoemission. There have been only a few "microscopic" studies of the Sb/Ge/Si system. An EXAFS study by Sakamoto *et al.* counted the Si-Ge bonds at the interface after growth with and without Sb [Saka92]. Their study showed that the intermixing of Ge and Si is suppressed by the presence of the Sb, but no conclusions were drawn concerning the bonding geometry of the Ge or Sb atoms. Another microscopic study of Sb/Ge/Si was conducted Cao *et al* [Cao92]. These authors observed changes in the surface shifted components from core-level

photoemission spectra for growth in the presence of Sb of Ge on Si and Si on Ge. By noting that the emission-components normally attributed to the surface reconstruction disappear upon the migration of Sb atoms to the growth front [Himp80], the authors concluded that the resultant Ge layers were well ordered and that the buried Si substrate was bulklike. In addition, these authors showed that the Sb floats to the surface of the Ge during growth on Si(100), an observation consistent with previous work [Cope90]. Again, however, no structural determination of the microscopic bonding geometry was attempted for the Ge or Sb layers.

There are two main structural points of interest to be addressed for this system. The first concerns the bonding geometry of the Sb overlayer. Since the Sb dimers on Si(100) were reported as symmetric [Richt90], and since 1 ML of Ge terminating the Si(100) should not alter drastically the binding environment of the Si surface (due to the chemical similarity of Ge and Si), naively, one would expect a similar structure for the Sb/Si and Sb/Ge/Si systems. However, the lattice mismatch between Si and Ge introduces a strain energy at the interface. In part this study was undertaken to determine the influence of this strained Ge layer on the local structural environment of the Sb adatoms.

The second important point concerns the state of the Ge adlayer upon Sb deposition. Subsurface layers have been shown to participate in the reconstruction of surfaces. For instance, it was only after distortions in the subsurface layers were considered that LEED [Appe78a; Jona77; Tong78] and ion scattering [Feld80; Sten81; Trom83] data from the clean Si(100)-2x1 surface could be fully understood. Also, the exact reconstructed atomic positions provide crucial information about the energetics of the surface when reproduced or predicted by total energy calculations [Chad79]. However, in studies of heteroepitaxy, very little published work has characterized the subsurface layers adequately. One reason is that with epitaxy

directly on the Si(100) surface, for many techniques (including ion scattering), the experimental signal from the near surface layers is obscured by or commingled with the bulk signal, making a determination of the atomic positions difficult or impossible. For the Sb/Ge/Si(100) system, in contrast to the case of Sb on clean Si(100), the second atomic layer (Ge) is visible clearly above the background with MeV ion scattering. This separation allows, using transmission ion channeling, the determination of the atomic positions with respect to the bulk of both the top, reconstructed Sb layer and the underlying Ge layer.

It should be noted that the study of this system is ideally suited to transmission ion channeling. This suitability occurs because the Ge and Sb adatoms both are referenced to a position deep in the bulk [Feld82], allowing the bonding sites of each to be determined independently. Also, few techniques can access buried layers. Again, since transmission channeling utilizes the flux distribution of ions in the channel, as determined by the substrate, the presence of the Sb overlayer has no impact on the processes leading to scattering from the Ge layer.

Experimental

After the *in situ* Si oxide desorption (chapter 4), Ge was deposited on the 2x1 Si(100) surface, held at 300°C, from a Knudsen cell at a rate of 0.1 ML/min. The pressure during evaporation remained in the 10⁻¹⁰ Torr range. The LEED pattern after Ge deposition remained unchanged except that the background increased slightly, indicating that the Ge formed a well-ordered overlayer. Again, the sample was held at 300°C and Sb was deposited from another Knudsen cell at >0.1 ML/min. Sb deposition at temperatures above 150°C has been shown to lead to saturation coverage on the clean Si(100) surface (chapter 8) [Barn86; Cope90]. After cooling, the LEED pattern was 1x1 with a high background and with very faint, blurry 1/2 order spots at certain energies. The LEED pattern was very similar to that for Sb on

clean Si(100) [Richt90; Noga91], indicating that the degree of long range order on the Sb/Si and Sb/Ge/Si surfaces is similar. The sample then was transferred under vacuum to the scattering chamber and analyzed at room temperature with a 2.5 MeV beam of He^+ ions having an angular divergence of $<0.08^\circ$. For the surface coverage, we measured 0.95 ML of Sb and 0.81 ML of Ge with RBS.

Although the slight disparity in Sb and Ge coverage should cause a portion ($\sim 14\%$) of the Sb adatoms to reside on Si (rather than on Ge/Si), the dimer structures on the two should be similar, and the effect on the results minimal. In fact, a Ge coverage of less than 1 ML is desirable for a precise characterization of that layer since, for thicker films (>1 ML), any portion of the film above 1 ML will be substitutional. This substitutional fraction would influence the results in much the same way as would intermixing between the Si and Ge layers. In the present case, the lower Ge coverage insures that all Ge resides on Si. Also, it is desirable that the Sb coverage exceed the Ge coverage in order that all of the Ge should reside under Sb.

To determine the adatom site(s) for this surface, angular scans were calculated using variable adatom positions and compared to the data using the chi-square minimization procedure described in chapter 6. Allowing for surface asymmetry, two independent adatom positions for each element (Ge and Sb) each were varied in two directions, parallel (in the direction of dimerization) and perpendicular to the surface. To determine the final structure (figure 10-3), all combinations of the best-fit configurations for both elements were considered, and those yielding unreasonable Sb-Ge bond lengths ($> 5\%$ deviation from the sum of the covalent radii, 2.62 Å) were disallowed. This restriction served mainly to reduce the size of the error bars, and had no influence on the final structure determined. No restrictions were placed on the Sb dimer bond length, or on Si-Ge bonds.

Another parameter in the fitting procedure was the two dimensional vibrational amplitude (ρ) of the adatoms. In general, enhanced vibrational amplitudes at surfaces are expected, and can be as much as a factor of two larger than bulk values [Woo88, p. 69]. Some reports even exist of extreme surface vibrational amplitudes, many times that of bulk [Mart92]. There is little consistency in the predictions or observations of such surface enhancements, however, especially for subsurface layers. In this study, although the Sb-covered Ge is near the surface, it is fully coordinated and would be expected to vibrate much like a bulk atom. Therefore, we took the magnitude of the vibrational amplitude for the Ge to be $\rho_{\text{Ge}}=0.14 \text{ \AA}$, a value equal to that used to calculate the Si scans. Then, for an exactly substitutional site, the Ge angular scans should have followed closely the bulk angular scans, which were reproduced by the calculation (see figure 10-1). For the Sb calculated scans, ρ_{Sb} was used as a fitting parameter. Again, all vibrations were assumed isotropic.

Results and Discussion

Figure 10-1 shows Ge angular scans across three low-index axial channeling directions for the Sb/Ge/Si(100) sample. Each filled circle represents the integrated Ge scattering yield at a given tilt angle across the axial channel. Likewise, open squares represent scattering from the Si substrate (i.e., a substitutional position) at the beam exit side of the sample. The calculated Si-host scans (lower solid lines) are for a substitutional site with a vibrational amplitude of 0.14 \AA . For comparison, experimental angular scans for a reconstructed Ge adlayer composed of dimers (grown at 300°C) [Gran94b] are shown as the open circles. These scans represent the state of the surface before Sb deposition (i.e., when the Ge was reconstructed, chapter 9). A comparison of the two Ge data sets shows that the Ge layer is altered significantly by the presence of the Sb. Also, the shapes and depths of the Sb-adsorbed Ge angular scans are very characteristic of a near-substitutional atomic site [Chu78, p. 269].

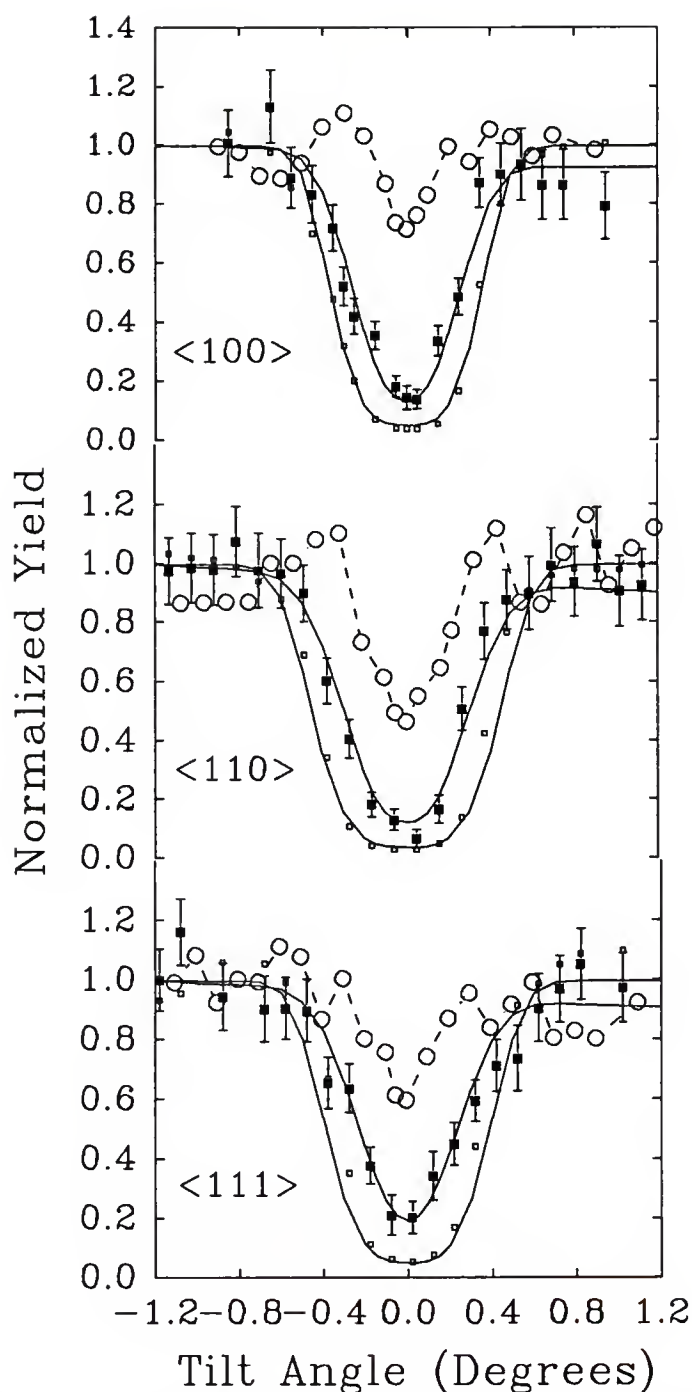


Figure 10-1. Ge angular scans across three axial channeling directions on the Si(100) surface with (filled circles) and without (open circles) an Sb overlayer. Also shown is the Si host scan (open squares). Solid curves are calculated scans for proposed Ge sites (upper solid curve) and a substitutional site (lower curve). Error bars indicate uncertainties due to counting statistics.

This similarity clearly indicates that the Ge reconstruction is lifted upon Sb deposition at 300°C.

This observation is consistent with core-level photoemission spectra for the Sb/Si [Yang92; Rich89b] (Sb/Ge [Yang92]) surface, which show that the Si 2*p* (Ge 3*d*) surface component vanishes upon Sb deposition. This component typically is associated with charge transfer between dimer atoms, and the disappearance of the component is interpreted as indicating a lifting of the reconstruction. Recently, further evidence of this was given by MEIS data from Sb/Si(100), which led the authors to conclude that the Si under adsorbed Sb becomes bulklike [Slij92]. In the MEIS study, however, no indication was given for a limit on the displacement of these subsurface atoms (and, since the analysis relies on comparisons with Monte Carlo simulations, this is not easy to estimate). In the present case, transmission ion channeling is a more sensitive technique to the Ge atomic positions [Lyma91a]. In figure 10-1 the reduced Ge-scan halfwidths, as compared to the Si-host, indicate that the sites are displaced from those for an ideal bulk-termination by Ge [Chu78 p. 269; Feld82, p. 78]. Indeed, the calculated Ge scans shown (upper solid curve) represent two equally weighted and *asymmetric* Ge sites, with one adatom very near a Si host site (substitutional in *x*, with a $0.07(\pm 0.08)$ Å *z* displacement), and the other displaced from a substitutional site by $0.39(\pm 0.04)$ Å in *x* and $-0.34(\pm 0.08)$ Å in *z*. The use of the term *asymmetric* here refers to the observation that the displacements for the two Ge sites are not equal.

The Ge data are reproduced assuming *symmetric* Ge displacements only with an unphysically large Ge vibrational amplitude ($\rho_{\text{Ge}}=0.28$ Å). It should be noted that, this large ρ_{Ge} could be interpreted a consequence of the disorder caused in the Ge layer by a high density of defects in the Sb overlayer. In principle, this disorder could lead to a distribution of Ge atomic sites, which would mimic an increased vibrational amplitude. In the absence of other observations, disorder could suitably explain our

experimental data. However, the presence of disorder in the Sb overlayer, as is indicated by the 1×1 LEED pattern and as is observed for the similar Sb/Si(100) surface, does not imply the lack of a well defined bonding geometry or the absence of well-defined local structure. In fact, our study on the Sb/Si(100) [Gran92b] surface showed that Sb overlayers grown at room temperature essentially have the same local structure as those for annealed Sb/Si(100) surfaces, even though the overlayer for the annealed case has been shown (by STM [Richt90; Rich89a]) to possess a much higher degree of order (see chapter 8). This can be reconciled with the LEED pattern by recognizing that a randomly distributed array of dimers gives rise to the same pattern as a partially ordered surface whose dimer domain length is shorter than the coherence length of the electrons [Woo88, p. 63]. In addition, due to the difference in widths of the Si and Ge scans, the data are not consistent with bulk-like Ge in the presence of a partially disordered overlayer. A contribution from a random component, which gives a flat angular scan, would preserve the width of the Si scans and only change the depth. Nor are the data reproduced well assuming a partial lifting (to bulk sites) of the reconstruction, with the remaining atoms in (experimentally determined [Gran94b], chapter 9) dimer sites. This assumption also leads to angular scans that are too wide. Therefore we have assumed that all Ge and Sb atoms reside in positions that are representative of the preferred local bonding geometry for this surface.

In figure 10-2 shows angular scans across the $\langle 100 \rangle$ and $\langle 111 \rangle$ axial channeling directions for the Sb data (filled squares). The calculated scans that best reproduce the Sb data are shown as the solid curves. The positions represented are for an asymmetric Sb-Sb dimer with a bond length of $2.76(\pm 0.07)$ Å and a dimer tilt of $7(\pm 3)^\circ$. The center of mass of the Sb dimer is displaced in z by $0.30(\pm 0.08)$ Å and by

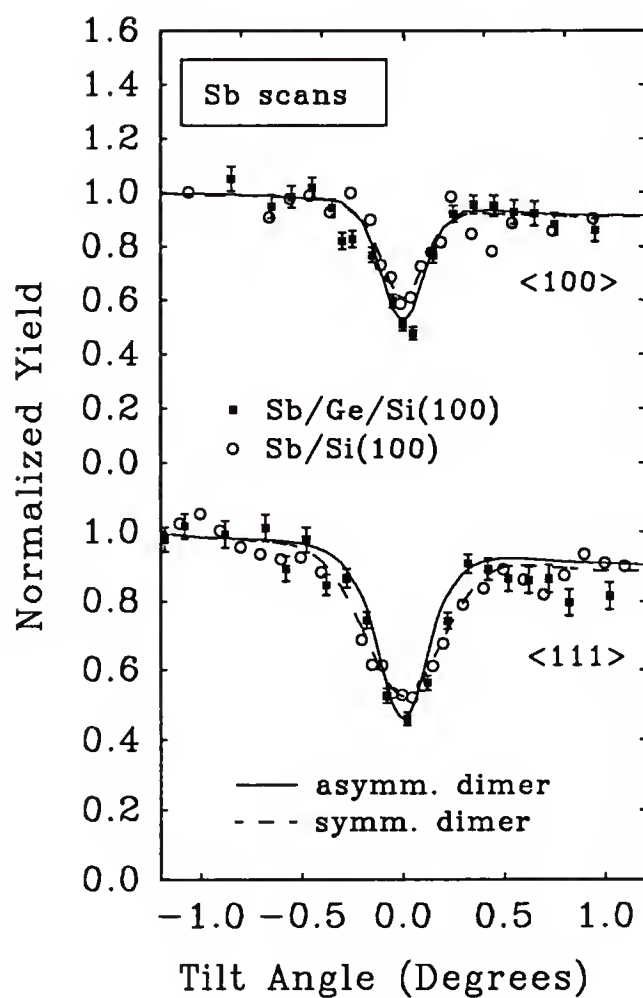


Figure 10-2. Sb angular scans across the $\langle 100 \rangle$ and $\langle 111 \rangle$ axial channeling directions. Filled squares are for an Sb/Ge/Si(100) surface, with calculated scans (solid curves) for an asymmetric dimer (discussed in text). Open circles are for an Sb/Si(100) surface, with calculated scans (dashed curves) for a symmetric dimer. The Sb/Si(100) data and calculation are from Grant *et al.* [Gran94a].

0.17(\pm 0.03) Å in x . The best-fit vibrational amplitude is $\rho_{\text{sb}}=0.2(\pm 0.1)$ Å, consistent with that found for Sb/Si(100) (chapter 8) [Gran92b]. Also shown are angular scans for Sb dimers on the clean Si(100) surface (open circles, discussed in chapter 9), which have been reported in the literature as symmetric [Richt90; Gran92b]. The dashed curves are calculated scans for an Sb dimer (bond length = 2.8 Å) having a tilt of 0°. The differences in the Sb/Si(100) and the Sb/Ge/Si(100) angular scans are subtle, approaching the resolution of the technique. This limited resolution is due partly to the sensitivity of the dimer tilt to small differences in the relative z positions of the adatoms, and to the low sensitivity of transmission ion channeling to atomic displacements in z . However, with the logical assumption that asymmetry in the Ge layer translates to asymmetry in the Sb layer (since the Ge and Sb are bonded), the argument for Sb dimer asymmetry is strong.

Shown in figure 10-3 is the structural model for the Sb/Ge/Si(100) system viewed along the $\langle 011 \rangle$ direction. In this model, the surface asymmetry is clearly visible. The positions of the adatoms (Ge, shaded circles; Sb, solid circles) are those determined above. The Si positions (open circles) represent the bulk lattice sites, without subsurface relaxation. In reality, these atoms would be displaced significantly from bulk positions for ~ 4 to 5 layers into the crystal [Appel78a; Jay93]. The Sb-Sb bond (2.76 Å) shown is slightly shorter than the bulk Sb-Sb bond (2.90 Å) and slightly shorter than that found in previous experiments for Sb/Si(100) [Richt90]. This geometry has Sb-Ge bond lengths that deviate by an average of 3.1% from the sum of the Sb and Ge covalent radii.

For the clean Si(100) surface, energy minimization calculations [Chad79] and other theoretical treatments, find that buckling of Si dimers is accompanied by a charge transfer from the down dimer atom to the up dimer atom (partially ionic bond). This charge transfer has been used to explain very high resolution Si $2p$ core-level

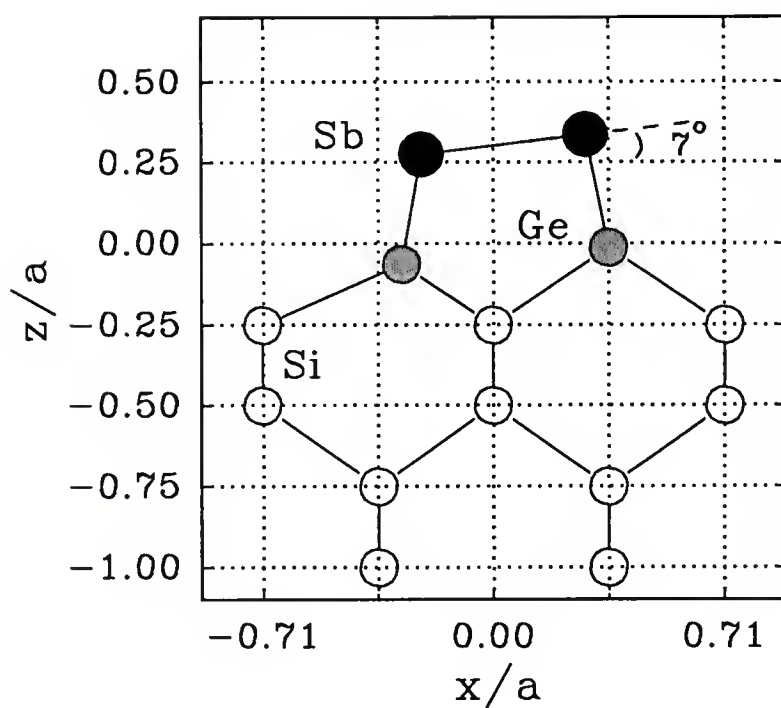


Figure 10-3. Bonding geometry of the Sb/Ge/Si(100) surface, showing asymmetric Sb dimer (filled circles) and displaced Ge layer (shaded circles). Units are fraction of a Si lattice constant ($a = 5.430 \text{ \AA}$).

photoemission spectra [Land92], which display two surface shifted components. Typically these components are assigned to the up and down dimer atoms. Another mechanism which could be driving the asymmetry concerns the hybridization [Mead89] of the surface atoms. Lohmeier *et al.* observed shifted Sb dimers on the Ge(100) surface in an x-ray diffraction study [Lohm92]. These authors suggested that the asymmetry might be driven by rehybridization in the Sb layer. In this picture, one of the dimer atoms undergoes an sp^3 -rehybridization and the other retains a p^3 nature, defining new equilibrium bond angles. It is not clear whether Sb-Sb or Sb-Ge charge transfer, or some surface rehybridization in the Sb or Ge layer could account for the observed asymmetry, or whether the asymmetry should be attributed to the additional, Ge-induced stress. This work, in the context of published work on Sb/Si(100), however, does suggest that surface dimer interactions with the second layer atoms (in this case Ge) are essential to the surface reconstruction. Clearly, state-of-the-art theoretical work such as total energy calculations or molecular dynamics simulations is needed to further clarify this structure.

CHAPTER 11

CONCLUSIONS

In this study, MeV transmission ion channeling was used to investigate the local bonding geometry of thin heteroepitaxial films (≤ 1 ML) grown on the Si(100) surface. Channeling has been widely used for impurity site location in bulk crystals and has been used in the transmission geometry to locate adatom sites on metal surfaces and chemically cleaned Si surfaces. However, the studies presented here are the first to use transmission ion channeling for adatom site determinations on clean, reconstructed semiconductor surfaces under ultrahigh vacuum conditions. In order not only to determine the adatom sites, but also to elucidate the adsorbate-adsorbate interactions involved in the initial stages of epitaxial growth, we have studied three related systems. These results illustrate the utility of the technique as applied to surface structural investigations, revealing the ability to determine the registry of the surface layer with the bulk, as well as the somewhat rare ability to characterize buried layers.

Sb on Si(100)

First, submonolayer films of Sb were investigated on the Si(100) surface [Gran92b]. Two types of Sb/Si(100) surfaces were studied, those deposited at 375°C and annealed at 500°C, and those deposited at temperatures ranging from room temperature to 375°C and not further annealed. As discussed in chapter 9, for the annealed surfaces, we find excellent agreement with a published SEXAFS study [Richt90] for the bonding geometry of the Sb. We conclude that the Sb-Sb adatoms form symmetric dimers on the surface, with an Sb-Sb bond length of 2.8 Å. For the unannealed surfaces, we find that the surface is also terminated by symmetric Sb-Sb dimers of the same geometry (within error bars).

Since our publication of these results [Gran92b], new experimental data have been reported on this system. The most important probably is an STM study by Mo [Mo92]. His images for very low coverages show, upon deposition of Sb_4 , the presence of several precursor states which involve Sb_4 and Sb_2 molecular species in various configurations on the surface. At first glance, these results appear to disagree with our channeling results. However, upon closer inspection, consistency can be found. First, Mo observed a significant fraction (0.27) of the adatoms in dimer sites at room temperature deposition, with a large fraction of the Sb converted to dimer sites with only a mild anneal. Additionally, he found that the precursor states could be converted simply by scanning the STM tip over Sb atoms in precursor states at a slightly increased voltage ($\sim 3\text{V}$ versus $\sim 1\text{V}$ volts for imaging). He calculated an effective activation energy of only 0.5 eV from the Sb_4 to the final dimer state. These data support our claim of dimer formation at room temperature on the surface.

With ion channeling we do not observe the precursor states reported by Mo [Mo92], but believe this can be attributed to the difference in Sb coverage. His study was for extremely low coverages ($\Theta_{\text{Ge}} = 0.02 \text{ ML}$). This is significant because a calculation based on the first-principles local-density method [Tang92] has shown that the final dimer state (with bulklike Si) is energetically favorable only at high Sb coverage. At lower coverages, the Sb atoms are seen [Tang92] to adsorb on the dimerized Si without breaking the Si-Si dimer bonds and lifting the Si reconstruction. This is also consistent with photoemission studies showing that the topmost Si layer becomes bulklike (the reconstruction is lifted) at a coverage of 0.6 ML [Richt90; Rich89b]. Therefore we believe that the precursor states observed by Mo are present on the surface only at very low coverages, and that at the coverage of our study (0.6 ML) the energetics of the surface are sufficiently altered (due to Sb-Sb and Sb-Si

interactions) that the precursor states are all converted to the final observed dimer state.

Ge on Si(100)

Next, Ge adsorbed on the Si(100) surface at 300°C has been investigated for coverages from 0.3 to 0.9 ML [Gran94b]. It is shown that for 0.6 ML, the surface is terminated by asymmetric Ge-Ge dimers having a bond length of 2.6 (± 0.1) Å and a dimer tilt of 12°($\pm 4^\circ$). This bond length and tilt angle is in excellent agreement with a recent x-ray standing wave study [Font93]. However, the bond length is longer than theoretical predictions (see table 9-1). As in the XSW study, we assume an isotropic vibrational amplitude. Again, the utility and reliability of transmission ion channeling was demonstrated, this time for asymmetric dimers.

Our results also show a marked coverage dependence, suggesting that the submonolayer growth of Ge on Si is considerably more complicated than for the homoepitaxy of Si on Si(100). This is presumably due to the strain induced by the ~4 % lattice mismatch, and is consistent with recent LEED, STM, and core-level photoemission results. Structural studies on heteroepitaxial systems often proceed under the assumption that all adatoms occupy locally identical positions, with no dependence on coverage. We have shown that this situation is not realized for this system. This raises the possibility that our site determination has been influenced slightly by mechanisms such as second layer growth, a mixture of dimer geometries, or our treatment of the vibrational amplitude. We have, however, taken care to minimize such effects.

Further work on this system should include a thorough characterization of the Ge-Ge bond length and Ge coordination with the Si as a function of coverage by a very sensitive technique, such as SEXAFS. This would insure that the dimer bond length does not change as a function of coverage. Also, since SEXAFS is sensitive to

the coordination of the surface atoms, this technique should be able to detect significant second layer Ge growth or Ge-Si intermixing [Saka92]. Additionally, studies such as this would be facilitated by a precise measurement of the adatom vibrational amplitude. Knowledge of the magnitude and asymmetry of the vibrations would increase the resolution of transmission channeling.

Sb on Ge on Si(100)

Along with the submonolayer Ge and Sb-terminated Si(100) surfaces, we have also characterized the Ge/Si(100) system upon 1 ML Sb chemisorption [Gran94a]. Two main structural points are addressed for this surface. The first concerns the state of the Ge adlayer upon Sb adsorption. We determine that the Ge reconstruction is lifted upon Sb deposition, showing that the local Ge structure is characterized by asymmetry. The second point concerns the geometry and symmetry of the Sb overlayer. Based on our data and logical assumptions, we conclude that the Sb overlayer on this surface is composed of asymmetric Sb-Sb dimers, in contrast to the symmetric dimers reported for the Si(100) surface [Richt93, Gran92b] and markedly different from the shifted Sb dimers recently reported on Ge(100) [Lohm92]. For the Sb/Ge/Si system, the characterization of the underlying Ge provides additional and convincing evidence for tilted Sb dimers. This study represents the first complete determination of the surface structure for epitaxial growth on a pseudomorphic semiconductor layer, and demonstrates the somewhat unique ability of transmission ion channeling to characterize buried layers.

This study should be of interest to a variety of experimentalists and theorists working in a range of surface related fields. One area in which these results might be particularly interesting concerns a recent development in core-level photoemission. Our results for the Sb/Ge/Si(100) system provide a characterization of the Ge atomic positions for the second layer. It would be very interesting to characterize the S'

behavior for this surface (1 ML Sb on 1 ML pseudomorphic Ge on Si) with core-level photoemission. Coupled with our experimental determination of the positions, such studies might clarify the mechanism leading to the S' surface shifted component.

APPENDIX A
Si *EX SITU* TREATMENT

Chemical Treatment

- I. Acetone soak{ 10 mins}
- II. Hot Methanol soak{ 10 mins}
DI rinse {30 sec}
- III. Hot Concentrated Nitric soak{ 10 mins}
DI rinse {30 sec}
HF dip (10%) {30 sec}
DI rinse {30 sec}
- IV. Hot NaOH:H₂O₂:H₂O soak { 10 min}
DI rinse {30 sec}
HF dip (10%) {30 sec}
DI rinse {30 sec}
- V. Hot HCl:H₂O₂:H₂O soak { 10 min}
DI rinse {30 sec}
HF dip (10%, fresh solution) {30 sec}
DI rinse {30 sec}
- VI. Hot HCl:H₂O₂:H₂O soak { 10 min}
DI rinse {30 sec}

Step III is repeated twice, steps IV and V are each repeated once, and step VI forms the protective oxide. Above, the word "hot" is defined as ~ 85°C. This temperature is accomplished by partially submerging the Teflon/Nalgene beaker

containing the samples and chemicals in heated water (in a glass bowl on a hot plate). The deionized water (DI) rinses are with 18.0 M Ω -cm water, filtered to remove organic contaminants also.

Sample Loading

After cleaning, one sample is mounted onto each of five Ta sample modules, held in place with Ta clips. The mounting is carried out in the chemical laboratory (on a different floor than the accelerator lab) under a laminar flow hood. We suspect that loading the samples in the dusty environment of the accelerator lab leads to contamination of the surface with particulates. The modules, with samples mounted, are then carried in a closed plastic container to the sample introduction chamber, loaded, and the chamber pumped down.

APPENDIX B

Ge THIN WINDOWS: DEFECT ANALYSIS

Thin Ge windows were used to align a 2.0 MeV ion beam with the $\langle 100 \rangle$ axial channeling direction for our Ge films on Si(100) (made from samples obtained from Spire Corporation, see chapter 4). The interface between the Si and Ge (defective region) was then analyzed using RBS with channeling by moving off of the window onto the thick part of the sample (as-grown). Shown in figure B-1 are spectra taken from a $\sim 1\mu\text{m}$ thick Ge/Si sample. The open circles are for aligned case, and the dashed line is from the aligned case on a bulk Ge wafer (separate experiment, see chapter 4). The solid squares are for random beam incidence. For the present case, we assume that the contribution from direct scattering is negligible compared to that from dechanneling [Feld82, chap. 4]. Subtracting the bulk channeling curve from the channeling spectrum of the as-grown film isolates the dechanneling contribution of the defects (solid circles). This dechanneling peak has been fitted to a Gaussian function (dotted line). As a first approximation, we treat the defect-induced dechanneling rate near the interface as a constant. This gives rise to a linear increase in the channeling yield that is abruptly terminated by the end of the Ge epilayer. This abrupt fall is softened by the finite system resolution (including straggling) at the interface, yielding a peak. The onset of dechanneling was taken to be 1.11 MeV, coincident with the rise in the dechanneling peak, and the falling edge was set to 0.89 MeV, the half-height of the back edge of the dechanneling peak. This range of energies corresponds to a thickness of $\sim 4000 \text{ \AA}$ in the Ge (or roughly 1/3 of the Ge film), which implies that either the defects themselves, or the lattice distortions associated with them, are

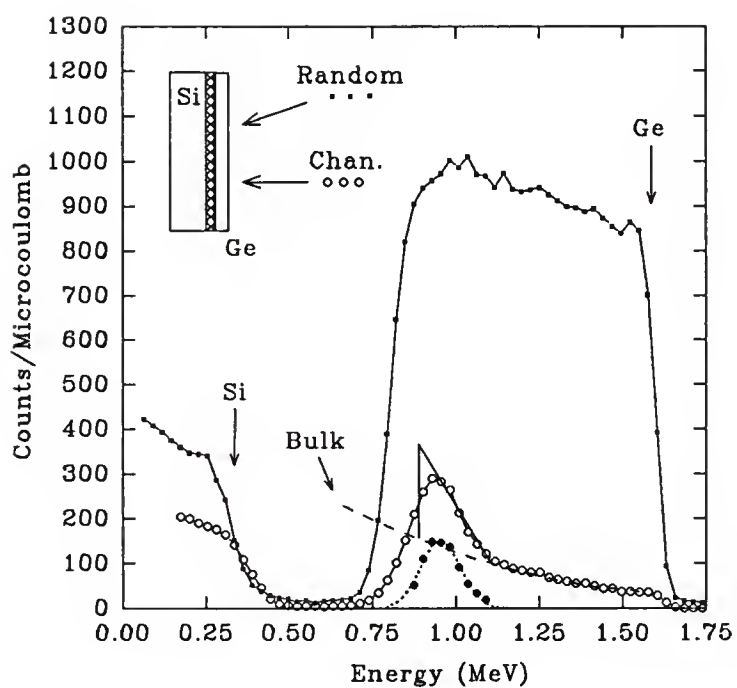


Figure B-1. Channeling and random spectra of as-grown Ge/Si(100). Also shown is the difference (solid circles) of the epitaxial-Ge channeling spectrum (open circles) and the measured bulk-Ge channeling spectrum (dashed line). A simple model for defect-induced dechanneling, assuming a constant dechanneling rate, is represented by the solid line.

distributed over this range. A region containing lattice distortions over roughly 1/3 of the Ge film is consistent with results from XTEM (see figure 4-3).

The area of the triangular-shaped region (solid curve) was set equal to the area of the dechanneling peak, which determined the height of the triangle and, thus, the total fraction of the beam dechanneled by defects in the Ge film. Adding the contribution to the dechanneled fraction at the exit of the Ge film from the bulk crystal, 0.18, to the contribution from the defects, 0.20, yields a dechanneled fraction of 0.38 as the beam reaches the Si substrate. The minimum yield at a depth of $\sim 4000 \text{ \AA}$ into the Si substrate is 0.58. This implies (neglecting the dechanneling contribution from defect-free Si) that dechanneling from defects in the Si contributes 0.20 to the minimum yield, the same contribution as from dechanneling in Ge.

For a fully relaxed Ge film, the number of misfit dislocations at the interface can be calculated to be $N_d = 0.02 / \text{\AA}$, assuming the Burger's vector lies in the interface plane. Setting the dechanneling probability, $P = \sigma_d N_d$ equal to the dechanneling in the Ge film (0.20) gives an experimental value for the dechanneling cross-section, $d = 10 \text{ \AA}$. A simple model for axial dechanneling by dislocations due to Quéré [Quer68] gives a value for d of 47 \AA . However, a more rigorous computer calculation by Kudo [Kudo75] gives values for dechanneling cross-sections a factor of 0.2 - 0.7 smaller than Quéré's for comparable systems. Thus, our data are consistent with dechanneling by misfit dislocations in a fully-relaxed Ge film.

REFERENCES

- [Abel75] F. Abel, G. Amsel, M. Bruneaux, C. Cohen and A. L'Hoir, Phys. Rev. B **12**, 4617 (1975).
- [Aler89] O.L. Alerhand, J.D. Joannopoulos and E.J. Mele, Phys. Rev. B **39**, 12622 (1989).
- [Appe78a] J.A. Appelbaum, G.A. Baraff, D.R. Hamann, H.D. Hagstrum and T. Sakurai, Surf. Sci. **70**, 654 (1978).
- [Appe78b] J.A. Appelbaum and D.R. Hamann, Surf. Sci. **74**, 21 (1978).
- [Appl67] B.R. Appleton, C. Erginsoy and W.M. Gibson, Phys. Rev. **161**, 330 (1967).
- [Arms71] J.C. Armstrong, W.M. Gibson and H.E. Wegner, Radiat. Eff. **11**, 241 (1971).
- [Barn86] S.A. Barnett, H.F. Winters and J.E. Greene, Surf. Sci. **165**, 303 (1986).
- [Barr71] J.H. Barrett, Phys. Rev. **3**, 1527 (1971).
- [Barr76] J.H. Barrett, F. Fujimoto, K. Komaki and Y. Hashimoto, Radiat. Eff. **28**, 119 (1976).
- [Bedz85] M.J. Bedzyk and G. Materlik, Phys. Rev. B **32**, 6456 (1985).
- [Bech88a] B. Bech Nielsen, Phys. Rev. B **37**, 6353 (1988).
- [Bech88b] B. Bech Nielsen, Ph.D. thesis, University of Aarhus, 1988.
- [Beck88] R.S. Becker, T. Klitsner and J.S. Vickers, J. Microsc. (Oxford) **152**, 157 (1988).
- [Behr87] A.M. Behrooz, R.L. Headrick, L.E. Seiberling and R.W. Zurmühle, Nucl. Instrum. Methods B **28**, 108 (1987).
- [Bens89] S. Bensalah, J.P. Lacharme and C.A. Sébenne, Surf. Sci. **211/212**, 586 (1989).
- [Bohg71] A. Bohg, J. Electrochem. Soc. **118**, 401 (1971).
- [Bohr15] N. Bohr, Phil. Mag. **30**, 581 (1915).
- [Bøgh67] E. Bøgh, in *Interaction of Radiation with Solids* (Plenum, New York, NY, 1967).

- [Bond72] E. Bonderup, H. Ebensen, J.U. Anderson and H.E. Schiøtt, *Radiat. Eff.* **12**, 261 (1972).
- [Bord76] J.A. Borders and J.M. Poate, *Phys. Rev. B* **13**, 969 (1976).
- [Boye61] H.E. Boyer, *Metals Handbook*, 8th ed. (American Soc. for Metals, Metals Park, OH, 1961) pp. 50-51.
- [Cao92] R. Cao, X. Yang, J. Terry and P. Pianetta, *Appl. Phys. Lett.* **61**, 2347 (1992).
- [Chad79] D.J. Chadi, *Phys. Rev. Lett.* **43**, 43 (1979).
- [Cheu80] N.W. Cheung, *Rev. Sci. Instr.* **51**, 1212 (1980).
- [Cheu81] N.W. Cheung and J.W. Mayer, *Phys. Rev. Lett* **46**, 671 (1981).
- [Chu78] W.-K. Chu, J.W. Mayer and M.-A. Nicolet, *Backscattering Spectrometry*, (Academic Press, San Diego, CA, 1978).
- [Cohe83] C. Cohen, J.A. Davies, A.V. Drigo and T.E. Jackman, *Nucl. Instrum. Methods B* **218**, 147 (1983).
- [Conw89] K.M. Conway, J.E. Macdonald, C. Norris, E. Vlieg and J.F. van der Veen, *Surf. Sci.* **15**, 555 (1989).
- [Cope89] M. Copel, M.C. Reuter, E. Kaxiras and R.M. Tromp, *Phys. Rev. Lett.* **63**, 632 (1989).
- [Cope90] M. Copel, M.C. Reuter, M. Horn von Hoegen and R.M. Tromp, *Phys. Rev. B* **42**, 11682 (1990).
- [Corb50] H.C. Corben, *Classical Mechanics*, 2nd ed. (Wiley, New York, NY, 1950).
- [Cric93] A. Cricenti, S. Selci, A.C. Felici, L. Ferrari, G. Contini and G. Chiarotti, *Phys. Rev. B* **47**, 15745 (1993).
- [Culb86] R.J. Culbertson, Y. Kuk and L.C. Feldman, *Surf. Sci.* **167**, 127 (1986).
- [Dabr92] J. Dabrowski and M. Scheffler, *App. Surf. Sci.* **56-58**, 15 (1992).
- [Davie60] J.A. Davies, J. Friesen and J.D. McIntyre, *Can. J. Chem.* **38**, 1526 (1960).
- [Davis78] L.E. Davis, N.C. MacDonald, P.W. Palmberg, G.E. Riach and R.E. Weber, P.A. *Handbook of Auger Electron Spectroscopy*, 2nd ed. (Physical Electronics, Eden Prairie, MN, 1978).
- [Dell73] G. Della Mea, A.V. Drigo, S. Lo Russo, P. Mazzoldi, G.G. Bentini, A. Desalvo and R. Rosa, *Phys. Rev. B* **7**, 4029 (1973).
- [Doyle68] P.A. Doyle and P.S. Turner, *Acta. Cryst. A* **24**, 390 (1968).
- [Dygo88] A. Dygo and A. Turos, *Phys. Lett. A* **127**, 281 (1988).

- [Dygo93] A. Dygo, W.N. Lennard and I.V. Mitchell, Nucl. Instrum. Methods B **74**, 581 (1993).
- [Dygo94] A. Dygo, M.A. Boshart, M.W. Grant and L.E. Seiberling, Nucl. Instrum. Methods B (in press, 1994).
- [Eagl93] D.J. Eaglesham, F.C. Unterwald and D.C. Jacobson, Phys. Rev. Lett. **70**, 966 (1993).
- [East80] D.E. Eastman, J. Vac. Sci. Technol. **17**, 492 (1980).
- [Fran49] F.C. Frank and J.H. van der Merwe, Proc. R. Soc. A **198**, 205 (1949).
- [Feld77] L.C. Feldman and S.T. Picraux, in *Ion Beam Handbook for Materials Analysis*, edited by J.W. Mayer and E. Rimini (Academic Press, New York, NY, 1977).
- [Feld78] L.C. Feldman, P.J. Silverman, J.S. Williams, T.E. Jackman and I. Stensgaard, Phys. Rev. Lett. **41**, 1386 (1978).
- [Feld80] L.C. Feldman, P.J. Silverman, and I. Stensgaard, Nucl. Instr. Methods **168**, 589 (1980).
- [Feld82] L.C. Feldman, J.W. Mayer and S.T. Picraux, *Materials Analysis by Ion Channeling* (Academic Press, New York, NY, 1982).
- [Feld86] L.C. Feldman and J.W. Mayer, *Fundamentals of Surface and Thin Film Analysis*, (Elsevier, New York, NY, 1986).
- [Font93] E. Fontes, J.R. Patel and F. Comin, Phys. Rev. Lett. **70**, 2790 (1993).
- [Gemm74] D.S. Gemmell, Revs. Mod. Phys. **46**, 129 (1974).
- [Gibs72] W.M. Gibson, Y. Hashimoto, R.J. Keddy, M. Maruyama, and G.M. Temmer, Phys. Rev. Lett. **29**, 74 (1972).
- [Gold80] H. Goldstein, *Classical Mechanics*, 2nd ed. (Addison-Wesley, Reading, MA, 1980) p. 115.
- [Goss85a] H.J. Gossman, L.C. Feldman and W.M. Gibson, Surf. Sci. **155**, 413 (1985).
- [Goss85b] H.J. Gossman and L.C. Feldman, Phys. Rev. B **32**, 6 (1985).
- [Gran92a] M.W. Grant and M.A. Boshart, FORTRAN code PROJECT.FOR (University of Florida, 1992).
- [Gran92b] M.W. Grant, P.F. Lyman, J.H. Hoogenraad and L.E. Seiberling, Surf. Sci. Lett. **279**, L180 (1992).
- [Gran93a] M.W. Grant, FORTRAN code DATAFIT.FOR (University of Florida, 1993).
- [Gran93b] M.W. Grant and M.A. Boshart, FORTRAN code STRAIN.FOR (University of Florida, 1993).

- [Gran93c] M.W. Grant and M.A. Boshart, FORTRAN code ANISO.FOR (University of Florida, 1993).
- [Gran93d] M.W. Grant, P.F. Lyman, J.H. Hoogenraad, B.S. Carlsward, D.A. Arms, L.E. Seiberling and F. Namavar, *J. Appl. Phys.* **73**, 2486 (1993).
- [Gran94a] M.W. Grant, M.A. Boshart, D.J. Dieleman, and L. E. Seiberling, *Surf. Sci. Lett.*, (in press, 1994).
- [Gran94b] M.W. Grant, D.J. Dieleman, M.A. Boshart and L.E. Seiberling, *Phys. Rev. B* (in press, 1994).
- [Hame86] R.J. Hamers, R.M. Tromp and J.E. Demuth, *Phys. Rev. B* **34**, 5343 (1986).
- [Hert85] N. Hertel, G. Materlik and J. Zegenhagen, *Z. Phys. B* **58**, 199 (1985).
- [Himp79] F.J. Himpsel and D.E. Eastman, *J. Vac. Sci. Technol.* **16**, 1297 (1979).
- [Himp80] F.J. Himpsel, P. Heimann, T.C. Chiang and D.E. Eastman, *Phys. Rev. Lett.* **45**, 1112 (1980).
- [Hoof80] H.A. van Hoof and M.J. van der Wiel, *Appl. Surf. Sci.* **6**, 444 (1980).
- [Hoog92] J.H. Hoogenraad, Masters thesis (Rijksuniversiteit Utrecht, 1992).
- [Horn91] M. Horn-von Hoegen, F.K. LeGoues, M. Copel, M.L. Reuter and R.M. Tromp, *Phys. Rev. Lett.* **67**, 1130 (1991).
- [Ishi86] A. Ishizaka and Y. Shiraki, *J. Electrochem. Soc.* **133**, 666 (1986).
- [Iwaw92a] F. Iwawaki, H. Kato, M. Tomitori and O. Nishikawa, *Ultramicroscopy* **42-44**, 895 (1992).
- [Iwaw92b] F. Iwawaki, M. Tomitori and O. Nishikawa, *Ultramicroscopy* **42-44**, 902 (1992).
- [Iwaw92c] F. Iwawaki, M. Tomitori and O. Nishikawa, *Surf. Sci.* **266**, 285 (1992).
- [Jaya93] G. Jayaram, P. Xu and L.D. Marks, *Phys. Rev. Lett.* **71**, 3489 (1993).
- [Jens90] F. Jensen, I. Stensgaard, F. Besenbacher and K. Mortensen, *Nucl. Instrum. and Meths. B* **48**, 334 (1990).
- [Jin85] H.S. Jin, T. Ito and W.M. Gibson, *J. Vac. Sci. Technol. A* **3**, 942 (1985).
- [Jin86] H.S. Jin and W.M. Gibson, *Nucl. Instrum. Methods B* **13**, 76 (1986).
- [Jin94] J.-M. Jin and L.J. Lewis, *Phys. Rev. B* **49**, 2201 (1994).
- [Jona77] F. Jona, H.D. Shih, A. Ignatiev, D.W. Jepsen and P.M. Marcus, *J. Phys. C* **10**, L67 (1977).
- [Keat66] P.N Keating, *Phys. Rev.* **145**, 637 (1966).

- [Keva85] S.D. Kevan, Phys. Rev. B **32**, 2344 (1985).
- [Knal92] J. Knall and J.B. Pethica, Surf. Sci. **265**, 156 (1992).
- [Köhl92] U. Köhler, O. Jusko, B. Müller, M. Horn-von Hoegen and M. Pook, Ultramicroscopy **42-44**, 832 (1992).
- [Kudo75] H. Kudo, J. Phys. Soc. Japan **40**, 1645 (1975).
- [Kvam91] E.P. Kvam and F. Namavar, Appl. Phys. Lett. **58**, 2357 (1991).
- [Land92] E. Landemark, C.J. Karlsson, Y.-C. Chao and R.I.G. Uhrberg, Phys. Rev. Lett. **69**, 1588 (1992).
- [Lin91] D.-S. Lin, T. Miller, and T.-C. Chiang, Phys. Rev. Lett. **67**, 2187 (1991).
- [Lind65] J. Lindhard, Kgl. Danske Videnskab. Selskab Mat.-Fys. Medd. **34**, No. 14 (1965).
- [Lohm92] M. Lohmeier, H.A. van der Vegt, R.G. van Silfhout, E. Vlieg, J.M.C. Thornton, J.E. Macdonald and P.M.L.O. Scholte, Surf. Sci. **275**, 190 (1992).
- [Lyma90] P.F. Lyman, FORTRAN code CUT.FOR (University of Florida, 1990).
- [Lyma91a] P.F. Lyman, Ph.D. thesis, University of Pennsylvania, 1991.
- [Lyma91b] P.F. Lyman, S. Thevuthasan, L.E. Seiberling, J. Cryst. Growth **113**, 45 (1991).
- [Mart92] R. Martinez, E. Fontes, J.A. Golovchenko and J.R. Patel, Phys. Rev. Lett. **69**, 1061 (1992).
- [Math74] J.W. Mathews and A.E. Blakeslee, J. Cryst. Growth **27**, 118 (1974).
- [Matz67] H. Matzke and J.A. Davies, J. Appl. Phys. **38**, 805 (1967).
- [Mead89] R.D. Meade and D. Vanderbilt, Phys. Rev. Lett. **63**, 1404 (1989).
- [Mo89] Y.-W. Mo, B.S. Swartzentruber, R. Kariotis, M.B. Webb and M.G. Lagally, Phys. Rev. Lett. **63**, 2393 (1989).
- [Mo90] Y.-W. Mo, R. Kariotis, B.S. Swartzentruber, M.B. Webb and M.G. Lagally, J. Vac. Sci. Technol. A **8**, 201 (1990).
- [Mo91] Y.M. Mo and M.G. Lagally, J. Cryst. Growth **111**, 876 (1991).
- [Mo92] Y.W. Mo, Phys. Rev. Lett. **69**, 3643 (1992).
- [Mönc79] W. Mönch, Surf. Sci. **86**, 672 (1979).
- [Morg73] D.V. Morgan, *Channeling: Theory, Observations and Applications*, edited by (Wiley, London, UK, 1973).

- [Mort88] K. Mortensen, F. Besenbacher, I. Stensgaard and W.R. Wampler, *Surf. Sci.* **205**, 433 (1988).
- [Nama90] F. Namavar, E. Cortesi, J.M. Manke, N.M. Kalkhoran, E.A. Johnson, O.A. DeSilvestre, M.C. Blythe, M.H. Johnson, and D.L. Perry, *Proc. of the 2nd ICEM*, pub. by MRS, Pitt. PA, **403** (1990).
- [Nama91] F. Namavar, J.M. Manke, E.P. Kvam, M.M. Sanfacon, C.H. Perry, and N.H. Kalkhoran, *MRS Symp. Proc.* **220**, 285 (1991).
- [Need87] M. Needels, M.C. Payne and J.D. Joannopoulos, *Phys. Rev. Lett.* **58**, 1765 (1987).
- [Noga91] J. Nogami, A.A. Baski and C.F. Quate, *Appl. Phys. Lett.* **68**, 475 (1991).
- [Oste92a] H.J. Osten, E. Bugiel and J.K. Klatt, *Appl. Phys. Lett.* **61**, 1918 (1992).
- [Oste92b] H.J. Osten, J.K. Klatt, G. Lippert, E. Bugiel, and S. Hinrich, *Appl. Phys. Lett.* **60**, 2522 (1992).
- [Oste92c] H.J. Osten, J.K. Klatt, G. Lippert, B. Dietrich and E. Bugiel, *Phys. Rev. Lett.* **69**, 450 (1992).
- [Oste93] H.J. Osten, J.K. Klatt, G. Lippert and E. Bugiel, *J. Appl. Phys.* **74**, 2507 (1993).
- [Outl84] R.A. Outlaw and P. Hopson, Jr., *J. Appl. Phys.* **55**, 1461 (1984).
- [Pres92] W.H. Press, S.A. Teukolsky, W.T. Vetterling and B.P. Flannery, *Numerical Recipes in FORTRAN*, 2nd ed. (Cambridge, New York, NY, 1992).
- [Quer68] Y. Quere, *Phys. Stat. Sol.* **30**, 713 (1968).
- [Redo82] A. Redondo and W.A. Goddard III, *J. Vac. Sci. Technol.* **21**, 344 (1982).
- [Rich89] D.H. Rich, F.M. Leibsle, A. Samsavar, E.S. Hirschorn, T. Miller and T.-C. Chiang, *Phys. Rev. B* **39**, 12758 (1989).
- [Richt90] M. Richter, J.C. Woicik, J. Nogami, P. Pianetta, K.E. Miyano, A.A. Baski, T. Kendelewicz, C.E. Bouldin, W.E. Spicer, C.F. Quate and I. Lindau, *Phys. Rev. Lett.* **65**, 3417 (1990).
- [Richt91] M. Richter, J.C. Woicik, P. Pianetta, K.E. Miyano, T. Kendelewicz, C.E. Bouldin, W.E. Spicer and I. Lindau, *J. Vac. Sci. Technol. A* **9**, 1951 (1991).
- [Robe90] N. Roberts and R.J. Needs, *Surf. Sci.* **236**, 112 (1990).
- [Rol60] P.K. Rol, J.M. Fluit, F.P. Viehböck and M. De Jong, *Proc. Fourth Inter. Conf. on Ionization Phenomena in Gases*, ed. by N.R. Nilsson (North-Holland, Amsterdam, 1960).

- [Rosn78] J.S. Rosner, W.M. Gibson, J.A. Golovchenko, A.N. Goland and H.E. Wegner, *Phys. Rev. B* **18**, 1066 (1978).
- [Ross92] R. Rossman, H.L. Meyerheim, V. Jahns, J. Wever, W. Moritz, D. Wolf, D. Dornisch and H. Schulz, *Surf. Sci.* **265**, 199 (1992).
- [Rowe74] J.E. Rowe and H. Ibach, *Phys. Rev. Lett.* **32**, 421 (1974).
- [Saka92] K. Sakamoto, K. Miki, T. Sakamoto, H. Yamaguchi, H. Oyanagi, H. Matsuhata and K. Kyoya, *Thin Solid Films* **222**, 112 (1992).
- [Schl59] R.E. Schlier and H.E. Farnsworth, *J. Chem. Phys.* **30**, 917 (1959).
- [Seib93] L.E. Seiberling, P.F. Lyman and M.W. Grant, *J. Vac. Sci. Technol. A* **11**, 715 (1993).
- [Shur90] M. Shur, *Physics of Semiconductor Devices*, (Prentice Hall, Englewood Cliffs, NJ, 1990).
- [Slij92] W.F.J. Slijkerman, P.M. Zagwijn, J.F. van der Veen, D.J. Gravesteijn and G.F.A. van der Walle, *Surf. Sci.* **262**, 25 (1992).
- [Steif87] A. Steif, S.C. Tiersten, and S.C. Ying, *Phys. Rev. B* **35**, 857 (1987).
- [Sten81] I. Stensgaard, L.C. Feldman and P.J. Silverman, *Surf. Sci.* **102**, 1 (1981).
- [Sten85] I. Stensgaard and F. Jakobsen, *Phys. Rev. Lett.* **54**, 711 (1985).
- [Sten92] I. Stensgaard, *Rep. Prog. Phys.* **55**, 989 (1992).
- [Stil92] F.H. Stillinger, *Phys. Rev. B* **46**, 9590 (1992).
- [Stra38] J.N. Stranski and L. Krastanov, *Ber. Akad. Wiss. Wien* **146**, 797 (1938).
- [Tang92] S. Tang, A.J. Freeman and B. Delly, *Phys. Rev. B* **45**, 1776 (1992).
- [Ters91] J. Tersoff, *Phys. Rev. B* **43**, 9377 (1991).
- [Ters92] J. Tersoff, *Phys. Rev. B* **45**, 8833 (1992).
- [Ters94] J. Tersoff, A.W. Denier van der Gon and R.M. Tromp, *Phys. Rev. Lett.* **72**, 266 (1994).
- [Tier86] S. Tiersten, S.C. Ying and T.L. Reinecke, *Phys. Rev. B* **33**, 4062 (1986).
- [Tong78] S.Y. Tong and A.L. Maldonado, *Surf. Sci.* **78**, 459 (1978).
- [Tour93] E. Tournié, K.H. Ploog, *Thin Solid Films* **231**, 43 (1993).
- [Trom81a] R.M. Tromp, R.G. Smeenk and F.W. Saris, *Phys. Rev. Lett.* **46**, 939 (1981).

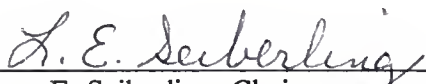
- [Trom81b] R.M. Tromp, R.G. Smeenk and F.W. Saris, *Solid. State Commun.* **39**, 755 (1981).
- [Trom83] R.M. Tromp, R.G. Smeenk, F.W. Saris and D.J. Chadi, *Surf. Sci.* **133**, 137 (1983).
- [Trom85] R.M. Tromp, R.J. Hamers and J.E. Demuth, *Phys. Rev. Lett.* **55**, 1303 (1985).
- [Trom92a] R.M. Tromp, A.W. Denier van der Gon and M.C. Reuter, *Phys. Rev. Lett.* **68**, 2313 (1992).
- [Trom92b] R.M. Tromp and M.C. Reuter, *Phys. Rev. Lett.* **68**, 954 (1992).
- [Trom93] R.M. Tromp, *Phys. Rev. B* **47**, 7125 (1993).
- [Uhrb81] R.I.G. Uhrberg, G.V. Hansson, J.M. Nicholls and S.A. Flodström, *Phys. Rev. B* **24**, 4684 (1981).
- [Uhrb86] R.I.G. Uhrberg, R.D. Bringans, R.Z. Bachrach, and J.E. Northrup, *Phys. Rev. Lett.* **56**, 520 (1986).
- [Uhrb92] R.I.G. Uhrberg, J.E. Northrup, D.K. Biebersen, R.D. Bringans and L.-E. Swartz, *Phys. Rev. B* **46**, 10251 (1992).
- [Van85] J.F. Van der Veen, *Surf. Sci. Rep.* **5**, 199 (1985).
- [Verw80] W.S. Verwoerd, *Surf. Sci.* **99**, 581 (1980).
- [Vlieg91] E. Vlieg, E. Fontes and J.R. Patel, *Phys. Rev. B* **43**, 7185 (1991).
- [Volm26] M. Volmer and A. Weber, *Z. Phys. Chem.* **119**, 277 (1926).
- [Wätj90] U. Wätjen, D. Schroyen, E. Bombelka and P. Rietveld, *Nucl. Instrum. Meth. B* **50**, 172 (1990).
- [Weak90] P.C. Weakliem, G.W. Smith and E.A. Carter, *Surf. Sci. Lett.* **232**, L219 (1990).
- [Wert91] G.K. Wertheim, D.M. Riffe, J.E. Rowe and D.E. Eastman, *Phys. Rev. Lett.* **67**, 120 (1991).
- [Wiel86] L.S. Wielunski, S. Hashimoto, and W.M. Gibson, *Nucl. Instr. Meth. B* **13**, 61 (1986).
- [Wolk92] R.A. Wolkow, *Phys. Rev. Lett.* **68**, 2636 (1992).
- [Wood86] D.P. Woodruff and T.A. Delchar, *Modern Techniques of Surface Science* (Cambridge University Press, Cambridge, 1986).
- [Yang92] X. Yang, R. Cao, J. Terry and P. Pianetta, *J. Vac. Sci. Technol B* **10**, 2013 (1992).
- [Yin81] M.T. Yin and M.L. Cohen, *Phys. Rev. B* **24**, 2303 (1981).

- [Zang88] A. Zangwill, *Physics at Surfaces*, (Cambridge University Press, Cambridge, UK, 1988).
- [Zieg77] J.F. Ziegler, *The Stopping and Ranges of Ions in Matter*, (Permagon, New York, NY, 1977).

BIOGRAPHICAL SKETCH

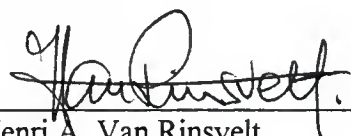
Mark Wayne Grant was born in a small town in Southern Indiana on November 4, in the year 1965. His parents are Larry Patrick Grant and Peggy Lee (Green) Grant, and he has two sisters, Michelle and Marsha. In 1984, the family moved to Green Cove Springs, Florida. Mark graduated from Clay High School in 1984 and received a 4-year academic (Presidential) scholarship to attend Jacksonville University in Jacksonville, Florida. He graduated *magna cum laude* from JU in 1988 with a B.S. in physics. Mark began graduate school (Department of Physics) at the University of Florida in September, 1988. After teaching for two years, he conducted his dissertation work under Professor L.E. Seiberling, studying heteroepitaxy on the Si(100) surface. On November 3, 1993, Mark and his family were blessed with the birth of a son, Hunter.

I certify that I have read this study and that in my opinion it conforms to acceptable standards of scholarly presentation and is fully adequate, in scope and quality, as a dissertation for the degree of Doctor of Philosophy.



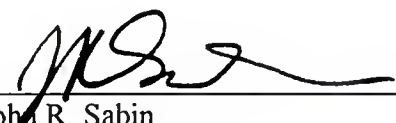
Lucy E. Seiberling, Chairperson
Associate Professor of Physics

I certify that I have read this study and that in my opinion it conforms to acceptable standards of scholarly presentation and is fully adequate, in scope and quality, as a dissertation for the degree of Doctor of Philosophy.



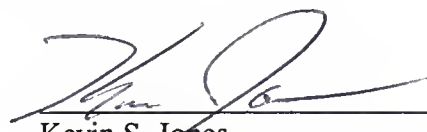
Henri A. Van Rinsvelt
Professor of Physics

I certify that I have read this study and that in my opinion it conforms to acceptable standards of scholarly presentation and is fully adequate, in scope and quality, as a dissertation for the degree of Doctor of Philosophy.



John R. Sabin
Professor of Physics

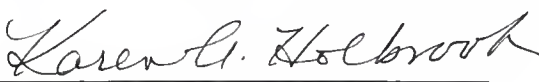
I certify that I have read this study and that in my opinion it conforms to acceptable standards of scholarly presentation and is fully adequate, in scope and quality, as a dissertation for the degree of Doctor of Philosophy.



Kevin S. Jones
Associate Professor of Materials Science
and Engineering

This dissertation was submitted to the Graduate Faculty of the Department of Physics in the College of Liberal Arts and Sciences and to the Graduate School and was accepted as partial fulfillment of the requirements for the degree of Doctor of Philosophy.

August 1994



Dean, Graduate School

UNIVERSITY OF FLORIDA



3 1262 08396 371 9